Periodic-Random Modulated Surface Textures

For Efficient Light Trapping in Thin-Film Silicon Solar Cells

T. C. Loef

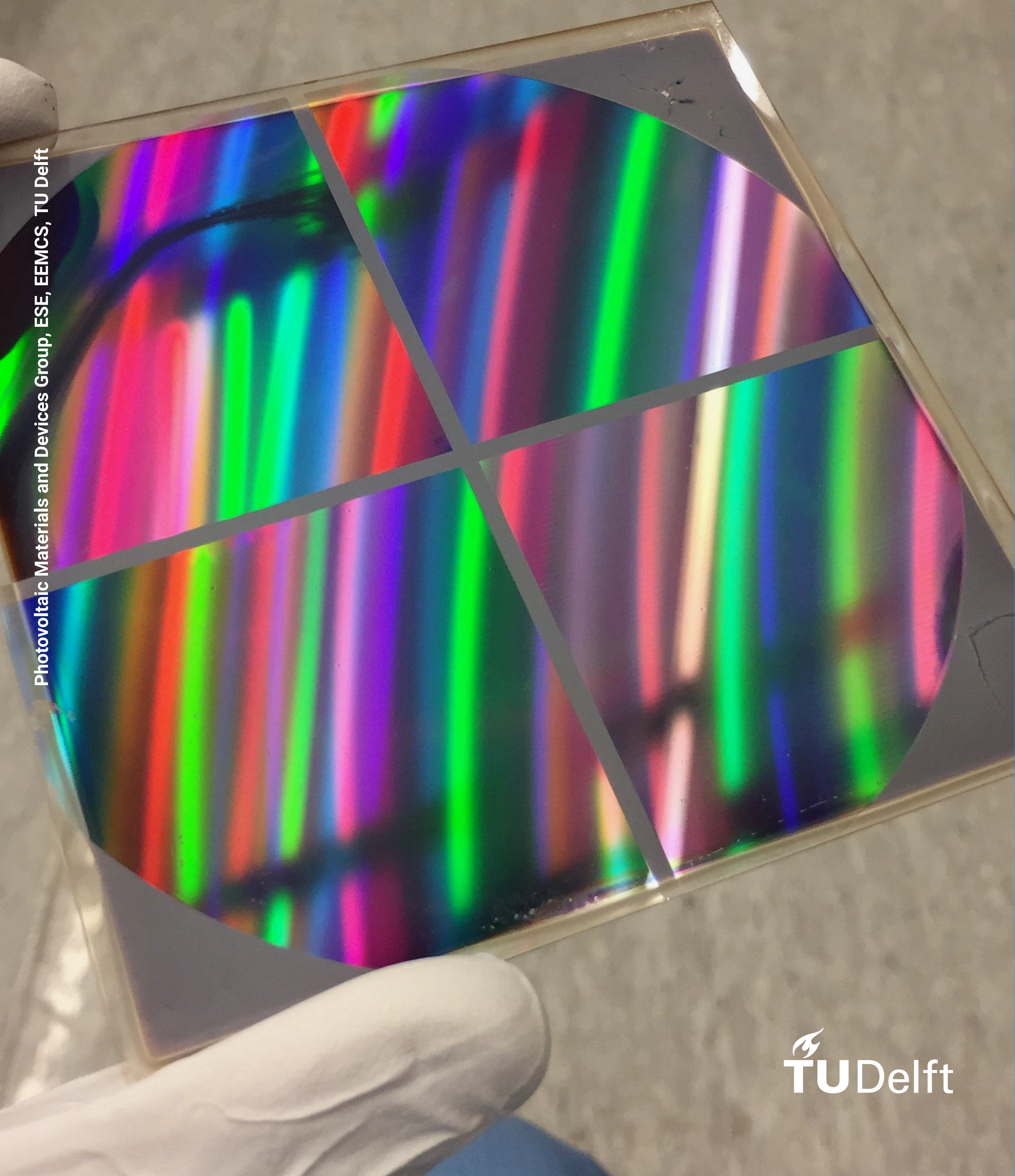

Photovoltaic Materials and Devices Group, ESE, EEMCS, TU Delft

TU Delft

Periodic-Random Modulated Surface Textures

For Efficient Light Trapping in Thin-Film Silicon Solar Cells

by

T. C. Loef

in partial fulfillment of the requirements for the Master of Science

Sustainable Energy Technology

at the Delft University of Technology,
to be defended publicly on Monday June 25, 2018 at 1:00 PM.

Student number:	4245490		
Project duration:	September, 2017 – June, 2018		
Thesis committee:	Dr. ir. O. Isabella	TU Delft, ESE - PVMD	Supervisor
	Ir. R. Vismara	TU Delft, ESE - PVMD	Daily supervisor
	Prof. dr. ir. M. Zeman	TU Delft, ESE - PVMD	Head of the ESE Department
	Dr. ir. M. Mastrangeli	TU Delft, ME - ECTM	External committee member

This thesis is confidential and cannot be made public until June 25, 2018.

Abstract

Thin-film silicon solar cells make use of relatively thin layers of active material compared to wafer-based solar cells. The main advantage of thin absorber layers is the possibility to fabricate flexible solar cells. However, due to limited absorber layer thickness and weak absorption coefficients at long wavelengths, light management techniques need to be implemented in order to increase the device performance. Advanced substrate texturisation is one of the promising light management techniques that have drawn much attention recently. In state-of-the-art devices, randomly textured interfaces are often used to increase the optical performance. However, the introduction of periodic diffraction gratings resulted in world record conversion efficiencies for hydrogenated amorphous/nanocrystalline silicon (a-Si:H/nc-Si:H) tandem solar cells.

A different method of advanced texturisation is introducing modulated surface textures (MST). These MST structures combine various surface morphologies (random and/or periodic) to reach higher levels of light scattering over a broader wavelength range. Modulated surface textures based on large periodic gratings and small random textures have been successfully employed in single-junction nc-Si:H solar cells, resulting in a world record efficiency of 11.8 %. An MST structure based on large random features and small periodic gratings, however, has not been reported yet.

The aim of this work is to investigate the possibility of fabricating MST structures based on micro-textured glass with superimposed periodic gratings, and to obtain a functioning *n-i-p* nc-Si:H solar cell, based on an MST substrate. An optical and morphological analysis of randomly textured substrates, periodic gratings, and modulated surface textures was carried out. It was found that MST substrates can be fabricated using ITO induced, wet-etched glass substrates, and a photolithography process. MST structures resulted in light scattering into greater, less distinct angles, when compared to either one of the individual surface morphologies. Therefore, these structures show promising light scattering behaviour for application in nc-Si:H solar cells.

Hydrogenated nanocrystalline silicon solar cells were fabricated on randomly textured glass substrates and MST structures. Two-dimensional (2D) periodic gratings, with square and hexagonal lattice structures, were superimposed on randomly textured glass to obtain MST substrates. nc-Si:H solar cells based on hexagonal MST structures seemed to outperform their square lattice counterparts. A functioning device with an active area efficiency of 6.46 % and short-circuit current density (J_{SC}) of 19.74 mA/cm^2 was fabricated. This work reports the first functioning nc-Si:H solar cell, based on a periodic-random modulated surface texture substrate. The best performing solar cell on randomly textured glass, however, exceeded this performance with an active area efficiency of 7.67 % and J_{SC} of 23.2 mA/cm^2. It can be concluded that functioning nc-Si:H solar cells can be fabricated on 2D MST substrates. Further research focused on the morphological optimisation of MST substrates could help to prevent defective material growth, to improve the electrical properties of future devices.

Contents

List of Figures

List of Tables

Preface

This master thesis marks the end of my studies in Sustainable Energy Technology (SET) at Delft University of Technology. Six very inspiring years have passed since I first started my BSc. degree in Mechanical Engineering. Looking back on my choice for SET now, I am sure I took the right decision. The last two years have brought me a lot of knowledge about different sustainable energy technologies, but more important: more awareness about the challenges we are facing to keep living on Earth like we do now. Considering everything I have learned, I am convinced that we can overcome the climate and energy challenges by deploying technological solutions in a smart way.

I could not have completed this thesis without the help of many people. I would like to thank my daily supervisor, Robin, for his excellent supervision. He helped me with experiments, guided me when it was necessary and was always available for a quick question. Thanks for the interesting discussions we had, sometimes in the office or lab, sometimes with a beer in the /Pub or during a barbecue. Furthermore I would like to thank Dr. ir. Olindo Isabella for his passion and enthusiasm that he expressed during my project. Working under his supervision, both during my thesis project and as a teaching assistant in the PV Lab, has enriched my career as an MSc. student. I am thankful to Prof. Dr. ir. Miro Zeman for letting me carry out my research in the PVMD group. Thanks to Dr. ir. Max Mastrangeli for his willingness to be part of my graduation committee as an external member. A big thanks to Gianluca for his help with the SEM images, to Guangtao for his helpful feedback and to my friend Martijn for his willingness to read my thesis and his very useful linguistic advice.

My gratitude goes to the process engineers and technicians that helped me to use the equipment. Stefaan Heirman and Martijn Tijssen assisted me in the measurement rooms and cleanrooms and never hesitated to help. *Hartelijk dank daarvoor!* Furthermore a big thanks goes to all EKL staff members that helped me out in the cleanroom, especially to Wim Wien.

Looking back on my time as a student in Delft, I realise that this experience would not have been possible without the support of many people close to me. I made new, international friends during the last two years. Without them it would not have been the same. Andrés, thanks for everything: your PV passion, the great fun, parties, chimichurri, and many pizza's (and of course the catering during the major part of my project). Sandeep and Sander for being great colleagues. Yifeng, Peiqing, Yiran and Gerwin for being thrust worthy buddies in the cleanrooms. Esteban, Chris, Manoj and Simona for being the best office mates. Marco, Luca and Michele for the great times we had. Julen, for being the proud Basque you are (I will definitely visit you in Bilbao sooner or later!). And finally Paolo, for being the great Italian/Belgian friend, colleague, and *topo*, to whom I could talk about anything that bothered me. To all, I hope we will meet very often in the future!

I want to thank my parents. Without their continuous love and support, I would not have reached this point. To them I say: *Bedankt voor alles wat jullie de afgelopen zes jaar en daarvoor voor mij betekend hebben. Zonder jullie had ik nooit op dit punt kunnen komen. Jullie constante aanmoedigingen en betrokkenheid bij mijn studie en scriptie gaven mij extra motivatie om door te gaan. Het gevoel dat ik ouders heb die trots zijn op wat ik heb bereikt, zal mij altijd bij blijven.* Finally, I would like to thank Babet for her love, support and patience. She helped me to stay calm and relax when the work was tough. Therefore: *Bedankt dat je er voor me was, ook wanneer ik maar moeizaam vooruit kwam. Jij was keer op keer mijn rustpunt in deze drukke periode. Ik kijk ontzettend uit naar onze rondreis in Australië en onze toekomst samen.*

Thomas Loef
Delft, June 2018

1

Introduction

1.1. The Global Energy Demand

During the last century, there has been a massive increase in global energy consumption. In the last 40 years, global primary energy consumption has doubled and reached a value of 155,000 TWh in 2016. Figure 1.1 shows that the majority of the primary energy is currently generated from fossil fuels such as coal, crude oil and natural gas. It is clear that during the past 50 years the pace of burning fossil fuels has increased drastically. This has resulted in more pollution and raised CO_2 concentration to a level that has not been reached for over 400,000 years [1]. This high CO_2 concentration has caused the global mean temperature to increase, resulting in various problems such as sea level rise and more frequent and intense cyclones and hurricanes.

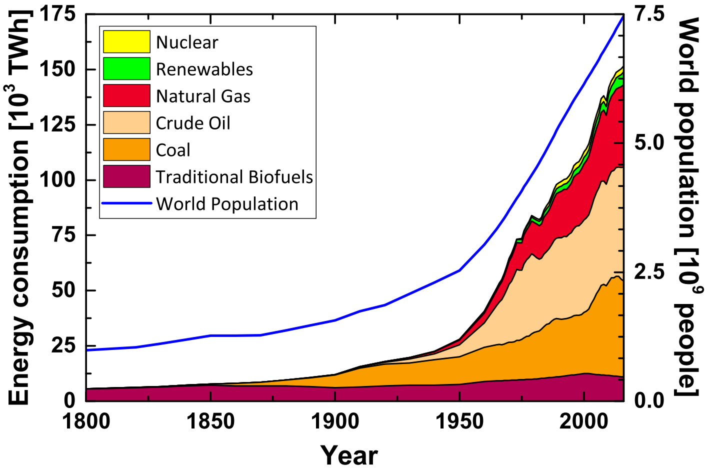

Figure 1.1: Annual global primary energy consumption from 1800 to 2016 and world population. Data adapted from [2–4] (population data were interpolated where necessary).

In the *International Energy Outlook 2017*, the U.S. Energy Information Administration recently revealed that world energy consumption is expected to increase by 28 % between 2015 and 2040 [5]. More than half of this increase is attributed to the strong economic growth in non-OECD countries in Asia (including China and India) [5].

Figure 1.1 might be misleading: it seems that the world population and energy consumption follow very similar curves. One could conclude that the increase in world population is the only reason for the rising energy demand. However, when the global primary energy consumption is expressed per capita (figure 1.2), it is clear that the use of energy per inhabitant has increased as well. The primary energy demand per capita almost doubled between 1950 and 2016. The population growth is expected to continue with a similar, approximate linear trend. The anticipated world population in 2050 is estimated at 9.7 billion people [3]. Moreover, most of the population growth will occur in regions of the world that are still in development (mainly Asia and Africa). If the primary energy demand per capita in these regions follows the expectations and rises, the total global energy demand will increase even more.

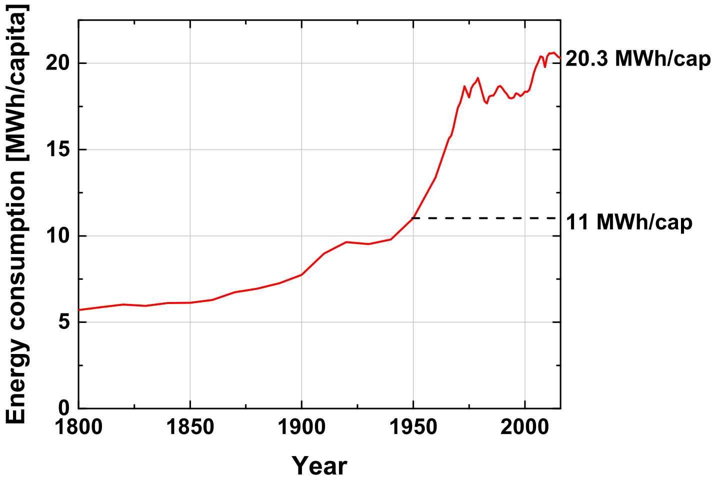

Figure 1.2: Annual global primary energy consumption per capita from 1800 to 2016. Data adapted from [2–4].

To be able to meet the future energy demand and reduce atmospheric pollution to an acceptable level, the need for clean and infinite energy sources is more evident than ever before. The largest sources of renewable energy such as hydro, wind, solar and biomass are already present in the current global energy mix. As shown in figure 1.1, however, the share of renewable energy sources is relatively small. Especially solar energy has a significant development potential, as the Sun is the largest source of energy for our planet [6]. Solar energy can be converted into electricity using a thermodynamic or electronic conversion method [7]. The first method is usually based on mirrors that focus sunlight on a heat exchanger. This heat exchanger transfers heat from the concentrated light to a working fluid. Steam turbines are used to generate electricity from this heat.

The second conversion method is based on a direct conversion from sunlight to electricity, using photovoltaic (PV) devices known as solar cells. Over the last decades, much research has been done on increasing the conversion efficiency and reducing the production costs of PV systems. As a result, the Levelised Cost of Electricity (LCOE) of solar energy has decreased rapidly, such that PV energy has obtained grid parity[1] in various locations. It is expected that the total system costs continue to decline, such that PV becomes an economically viable source of electricity over expanding geographical regions [8].

1.2. Basic Working Principle of Solar Cells

Solar cells convert sunlight into electricity, based on the photovoltaic effect: the generation of a potential difference between two different materials upon exposure to light (or more general: electromagnetic radiation). In 1901, the German physicist Max Planck published an article in which he suggested that light consists of discrete energy packages which he called *energieelemente* [9]. These packages are nowadays referred to as *photons*. Albert Einstein later demonstrated that Planck was

---

[1] Grid parity occurs when the LCOE of a renewable energy source is less than or equal to the sales price of electricity from the grid.

right and received the Nobel Prize in Physics for this achievement in 1921 [10]. The energy of a photon was defined by Planck as:

$$E = h \cdot v \tag{1.1}$$

where h is Planck's constant and v is the frequency of the electromagnetic radiation. The photovoltaic effect can be divided into three main processes that will be described briefly.

Generation of Charge Carriers

The semiconductor material that is used to absorb the incident light is characterised by its band gap energy (E_G). If the semiconductor material is ideal (contains no defects), electrons are only allowed to occupy a position below the *valence band* and above the *conduction band*. The band gap describes the difference between these energy states: $E_G = E_C - E_V$. When a photon is absorbed in a semiconductor material, its energy (E_{ph}) is used to excite an electron from the valence band to the conduction band. Hence, a photon is only able to excite an electron into the conduction band as long as its energy is equal to, or greater than the band gap energy ($E_{ph} \geq E_G$). In figure 1.3 the absorption of a photon and the electron travelling to the conduction band is visualised in steps 1 and 2 respectively. If the energy of a photon is greater than the band gap energy, a part of the energy is thermalised, i.e. converted into heat. This last process is represented in step 3 of figure 1.3.

The excitation of an electron to the conduction band can physically be described as liberating the electron from its atom in the lattice structure. The electron is able to move freely through the lattice, while leaving an empty spot behind. This empty spot is called a *hole* that behaves as a particle with a positive elementary charge.

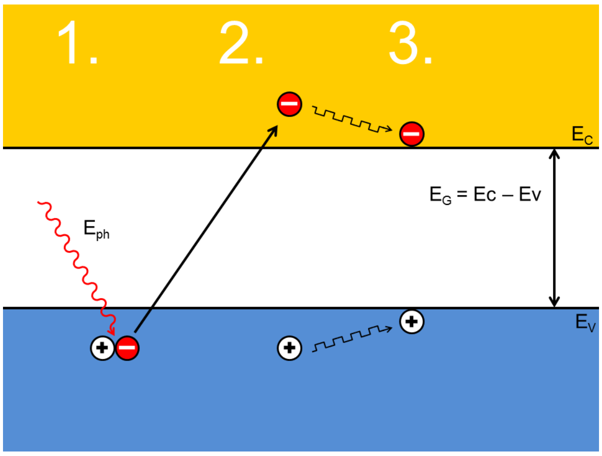

Figure 1.3: The absorption of a photon (1) generates an electron-hole pair when an electron is excited into the conduction band (2) if $E_{ph} \geq E_G$. A part of the photon energy is lost due to thermalisation (3) when $E_{ph} > E_G$.

Separation of Generated Charge Carriers

When the electron and the hole are not separated, they will recombine and release energy as a photon (*radiative recombination*) or transfer it to other electrons, holes or a lattice vibration (*non-radiative recombination*) [10]. To separate charge carriers, most solar cells are made of a combination of *p*-type and *n*-type doped materials. When *p*-type silicon is in contact with *n*-type silicon, electrons will diffuse from the *n*-type side (high electron concentration) to the *p*-type side (low electron concentration). If there is no external circuit connected, electrons will recombine with holes and on both sides of the *p*-*n* junction a charge will build up, creating an electric field. If a photon generates an electron-hole pair, charge carriers will move in the absorber layer. If the diffusion length of charge carriers is large enough they can reach the *p*-*n* junction. This *p*-*n* junction will force electrons from the *p* side to the *n* side, and holes in the other direction. Once the charge carriers reach their side of the *p*-*n* junction, they can be collected at the terminals of the solar cell.

Collection of Generated Charge Carriers

To make use of the energy contained by the charge carriers, an external circuit should be connected to the electrical contacts of the solar cell. The electrons will flow through the circuit and perform work in components of the external circuit. When the electrons passed through the circuit they will reach the *p*-type semiconductor-metal contact. The electrons will recombine with holes at this interface.

1.3. Solar Cell History and Modern Technologies

In 1839, the photovoltaic effect was discovered by the French physicist Alexandre-Endmond Becquerel. Becquerel submerged two platinum electrodes in an *electrolyte*: an electrically conducting solution [10]. He discovered that this experiment setup produced electricity when exposed to sunlight. The first functioning PV device, based on selenium with a thin layer of gold, was created in 1883 by Charles Fritts. The conversion efficiency of this solar cell was approximately 1 % [10]. The first solar cell based on silicon (Si) was made in 1941 by R. Ohl [11]. Since that moment, research has focused on silicon-based solar cells, and companies have started developing them. In 1985, Martin Green demonstrated a crystalline silicon (c-Si) solar cell with a conversion efficiency over 20 % [10].

Since 2000, environmental issues have become more prominent in public discussions, generating increased interest in solar energy. The PV market has evolved into a global market, in which Germany has taken the lead with a progressive feed-in tariff policy [10]. In 2016, the global installed PV capacity reached a new milestone of 300 GW [12], resulting in a 1.8 % share of the global electricity generation. With an annual installed capacity of 34.54 GW and a cumulative installed capacity of 78.07 GW, China has the largest PV market. The Netherlands reached an annual installed capacity of 700 MW in 2017, leading to a cumulative installed capacity of 2.7 GW [13].

Many different solar cell technologies for various applications have been developed during the last century. In the following sections these different types of solar cells will be discussed.

1.3.1. Wafer-Based Solar Cells

The PV market is currently dominated by c-Si wafer-based solar cells. In 2016, about 94 % of the solar cell production was based on c-Si technology [14]. Wafer-based c-Si solar cells can be based either on monocrystalline or polycrystalline silicon. Monocrystalline silicon solar cells are fabricated on wafers that consist of a large single crystal. Polycrystalline solar cells are based on wafers that consist of multiple crystals, which are usually cheaper than their monocrystalline counterparts. Wafer-based c-Si solar cells have greatly benefited from the know-how and manufacturing tools that were already developed in the integrated circuit industry [15]. A drawback of these first generation solar cells was that the 200-250 µm thick wafers were responsible for a large part of the production costs. Therefore, a new generation of solar cells evolved in order to try to reduce these costs by using thin-film devices [15, 16].

1.3.2. Thin-Film Technology

Second generation PV technology, or *thin-film technology*, consists of single-junction solar cells that aim to reduce the use of material while maintaining the conversion efficiencies of the first generation. These solar cells are made through the deposition of a thin layer of active material on a sub- or superstrate. This technology can reduce the thickness of the active layer to only 1-10 µm, which could potentially lead to a great cost reduction [15]. The relatively thin layers and their corresponding production processes allow for the production of flexible solar cells, which is an advantage compared to rigid wafer-based solar cells. However, these thin layers of active material introduce an important drawback. In order to absorb a sufficient amount of light, light management techniques need to be implemented (further explained in chapter 2). In general, thin-film solar cells are less efficient than c-Si solar cells, with the exception of gallium arsenide (GaAs) solar cells [10]. Materials that are commonly used for thin-film solar cells are amorphous silicon (a-Si), micro-crystalline silicon (μc-Si), copper-indium-(gallium)-diselenide (CI(G)S) and cadmium-telluride (CdTe) [15]. Current world record efficiencies are 14.0 % for thin-film silicon (stabilised), 22.6 % for CIGS, and 22.1 % for CdTe [17]. Thin-film solar cells were expected to become significantly cheaper than wafer-based solar cells. However, due to the ongoing drop in production costs of silicon wafers, the price of wafer-based solar cells stays close to that of thin-film solar cells.

1.3.3. Third Generation Solar Cells

The term *third generation solar cells* is used to refer to all new PV technologies that have the goal of exceeding the Shockley-Queisser (SQ) limit for single-junction solar cells [10]. The SQ-limit is a thermodynamic approach to estimate the maximum conversion efficiency of single-junction solar cells based on the bandgap of the semiconductor material. Exceeding the SQ-limit might be possible by overcoming one of the following limits for classic single-junction solar cells [10].

- Only one semiconductor material with one bandgap can be used. Therefore, a part of the energy of high energetic photons is lost (further described in chapter 2).
- Most solar cells are based on a single sun irradiance. A higher irradiance can increase the conversion efficiency.
- Photons with lower energy levels than the bandgap of the semiconductor cannot generate charge carriers and are therefore considered to be lost.

Various concepts have been developed to overcome these limitations. An important method for overcoming the first limitation is the use of multiple layers of active material, in which each layer absorbs a different part of the incident spectrum. This concept is known as the multi-junction approach. A multi-junction solar cell is built by stacking two or more subcells on top of each other. In such a device, light first enters the cell with the highest bandgap, where the blue, high energetic part of the spectrum is absorbed. The last cell that the incident light reaches has the lowest bandgap, to absorb the red, low energetic part of the spectrum. A typical Si multi-junction solar cell consists of a-Si and μc-Si subcells (also known as nano-crystalline silicon (nc-Si)). The current world record efficiency for a triple-junction a-Si/μc-Si/μc-Si cell is 14.0 % [18].

To overcome the second limitation, incident sunlight can be concentrated using optical lenses. The voltage of a solar cell increases logarithmically with an increasing irradiance. Concentrating the incident irradiance can therefore increase the efficiency of a solar cell [10]. The current world record efficiency for a multi-junction cell (GaInP/GaAs; GaInAsP/GaInAs) under an intensity of 508 Suns is 46.0 % [17, 18]. This is currently the highest conversion efficiency for all solar cell technologies available.

Many more interesting solar cell concepts such as quantum dot/quantum well, organic, dye-sensitised and hot carrier solar cells are being introduced and investigated. Some of these technologies are already being demonstrated in lab-scale solar cells, others are still in an early research phase. Figure 1.4 shows all world record efficiencies that have been achieved for different PV technologies from 1976 to the present [17].

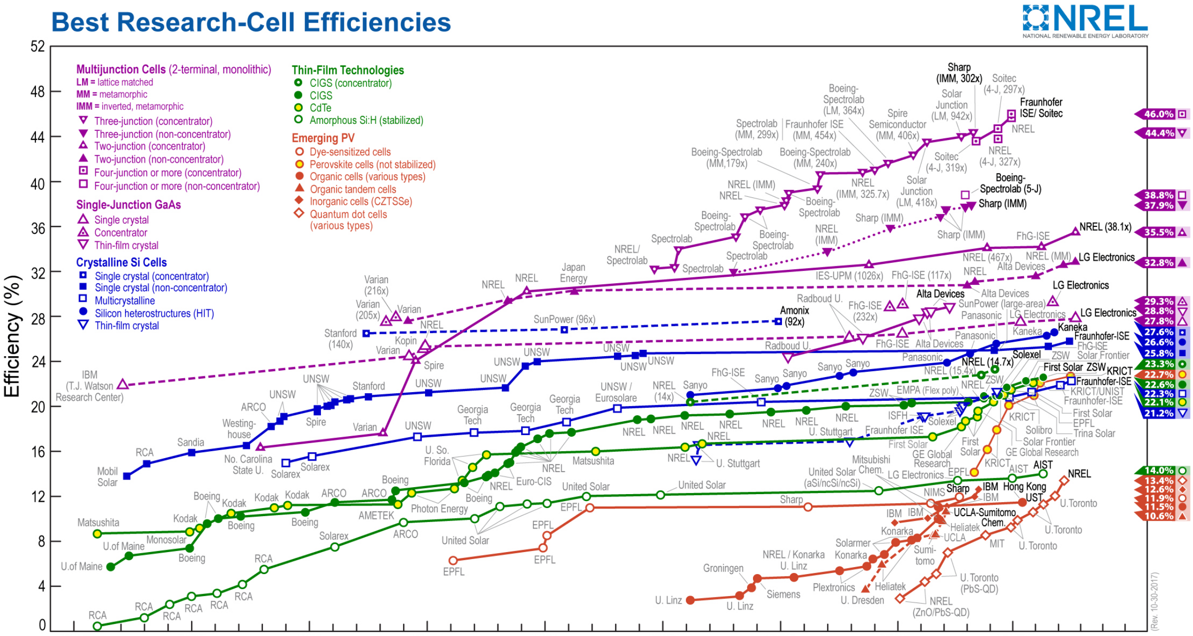

Figure 1.4: NREL research efficiency chart for different PV technologies from 1976 to present [17].

1.4. Thin-Film Silicon Solar Cells

As explained in section 1.3.2, thin-film solar cells are being developed in order to reduce the use of material and to bring down manufacturing costs. The first thin-film solar cell based on amorphous silicon was made in 1976 by D. E. Carlson and C. R. Wronski [19]. This solar cell had an initial efficiency of 2.4 % under an AM1.0 spectrum. Since then, the development of thin-film solar cells has commenced and was firstly commercialised into a large-area module in 1986 by Arco Solar [20].

In doped a-Si:H layers, electronic properties such as diffusion length and mobility of charge carriers are relatively poor compared to c-Si. Thin-film silicon solar cells make use of *p*-*i*-*n* junctions instead of *p*-*n* junctions. The intrinsic (undoped) layer is less defective than the doped layers and charge carriers in this type of material have a lower recombination rate. The intrinsic layer is sandwiched between a *p*- and an *n*-layer. This sandwich structure results in an electric field across the *p*-*i*-*n* junction. In typical c-Si solar cells with *p*-*n* junctions charge carrier separation is based on *diffusion*. In thin-film solar cells, however, the photo-generated charge carriers are separated and forced to the terminals of the cell by an internal electric field. Thin-film solar cells are therefore called *drift* devices [7].

There are two main configurations that are used to build up a thin-film silicon solar cell (figure 1.5). The first option is a so-called *superstrate* configuration. In this case, a transparent carrier gives mechanical strength to the device. The solar cell deposition takes place in the following order: (i) a front transparent conductive oxide (TCO) layer that collects the holes, (ii) *p*-type, intrinsic and *n*-type silicon layers that form the active layers in the solar cell, (iii) back TCO and (iv) metal back contact to collect the electrons [7]. For thin-film silicon solar cells, these superstrate devices are also called *p*-*i*-*n* solar cells. Due to the relatively poor mobility of holes in a-Si or nc-Si compared to wafer-based c-Si solar cells, the *p*-layer is used as a window layer. This ensures that the average distance that holes have to travel in order to be collected at the terminals is less than the distance travelled by electrons. A sketch of a typical thin-film *p*-*i*-*n* device is shown in figure 1.5a.

Besides *p*-*i*-*n* devices, thin-film silicon solar cells can also be deposited in the so-called *n*-*i*-*p* or *substrate* configuration. Substrate-based devices allow for the use of any type of material that can

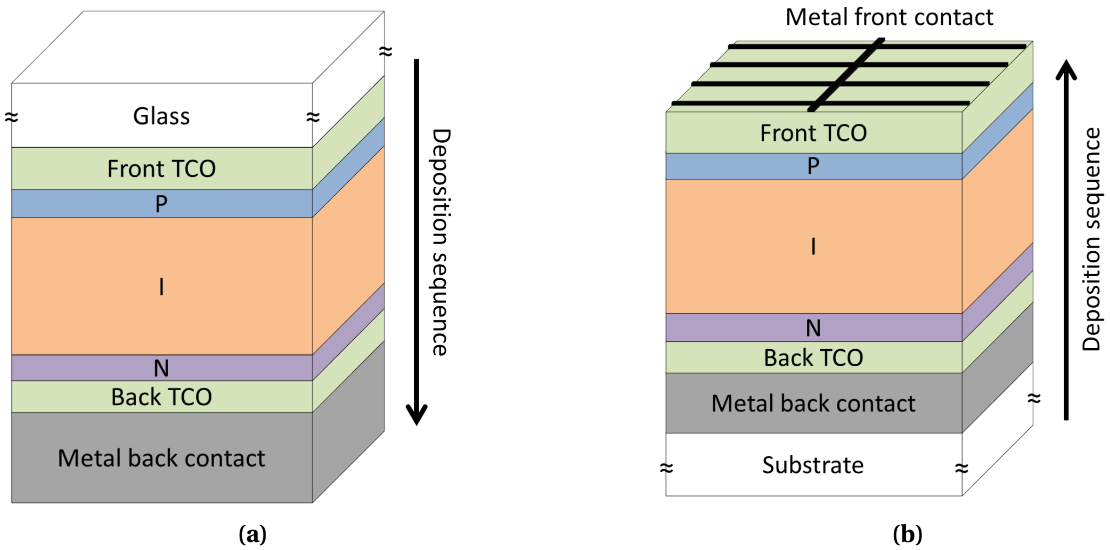

Figure 1.5: Sketches of thin-film solar cells with a *p*-*i*-*n* or superstrate configuration (a) and a *n*-*i*-*p* or substrate configuration (b).

give mechanical strength as a substrate, independent of the optical characteristics of the material. By using opaque foils or stainless steel, flexible solar cells can be manufactured [21]. The deposition sequence of *n*-*i*-*p* cells is exactly opposite to *p*-*i*-*n* configured solar cells. A metal layer will be evaporated first, acting as a back contact and back reflector. On top of the metal back contact the back TCO, *n*-type, intrinsic and *p*-type silicon layers are deposited. Finally, a front TCO and a metal front contact are deposited and evaporated to collect the charge carriers at the front of the cell. Figure 1.5b shows a sketch of a typical *n*-*i*-*p* device.

Although figures 1.5a and 1.5b show flat interfaces between the different layers, a texture is usually introduced to scatter light in the solar cell. For *p*-*i*-*n* devices, a texture could be introduced at the glass/TCO or TCO/*p*-layer interfaces. In *n*-*i*-*p* devices the substrate or back TCO could be textured in order to obtain rough interfaces between the different layers [7]. Textured interfaces help to decrease different reflections and enhance the light absorption in a solar cell. Making use of different types of textures in a smart way, to enhance light absorption, is the main focus of this work.

1.4.1. Amorphous and Nanocrystalline Silicon

Basic thin-film silicon solar cells consist of a-Si:H and nc-Si:H layers that are deposited using plasma-enhanced chemical vapour deposition (PECVD). The structure of these materials is different than that of c-Si used for wafer-based solar cells. In c-Si, atoms are arranged in a diamond-like lattice structure. Because silicon atoms have four valence electrons, each atom can form four covalent bonds with other atoms. Each atom in a c-Si structure is therefore covalently bonded to four neighbouring Si atoms [10, 21]. A different structure is present in a-Si. Not all Si atoms have four covalent bonds and some small deviations in bond angle and distance occur [21]. This results in so-called *dangling bonds*: valence electrons that do not form a bond with a valence electron of a neighbouring atom. Because dangling bonds cause more recombination, hydrogen is very often incorporated in a-Si layers to form Si-H bonds and passivate the dangling bonds. The resulting material is called *hydrogenated amorphous silicon* (a-Si:H).

Another material structure that is often used in thin-film silicon solar cells is nanocrystalline silicon (nc-Si). Due to their lower band gap, nc-Si cells are often used as bottom cells in a multi-junction structure. This material, also known as microcrystalline silicon (μc-Si), consists of crystalline grains in an a-Si matrix [21]. These grains grow in the form of cones. If two or more cones

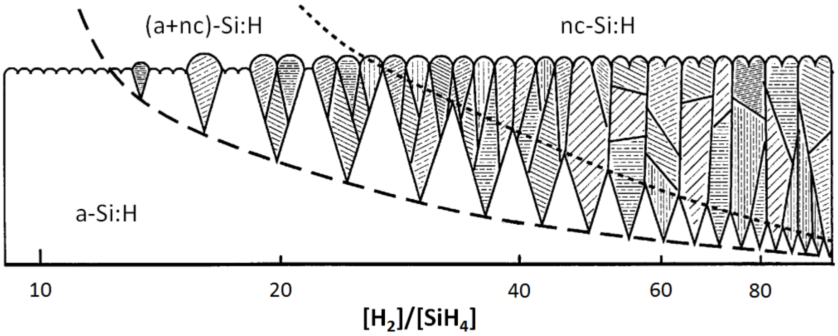

Figure 1.6: Schematic representation of different Si:H layers with amorphous silicon on the left and nanocrystalline silicon on the right. Based on, and adapted from [22].

collide, grain boundaries will appear [21]. The band gap of this material can be tuned by varying the ratio of crystalline to amorphous material. The content of crystalline material depends on the ratio of H_2/SiH_4 during the deposition of the layer (further explained in subsection 3.1.4). A schematic representation of the structure of Si:H layers and the different material structures is shown in figure 1.6.

1.5. External Solar Cell Parameters

To compare solar cells based on different technologies and manufacturers, the characteristics of solar cells are measured under standard test conditions (STC). Under these conditions the irradiance is 1000 W/m^2, the cell temperature is 25 °C, and the solar spectrum is an AM1.5G spectrum [23]. The AM1.5G spectrum will be further discussed in section 2.3.1.

To compare different solar cells in terms of performance, it is important to define performance parameters. The main parameters that determine the performance of a solar cell are the *peak power* (P_{max}), the *open circuit voltage* (V_{OC}), the *short circuit current density* (J_{SC}), and the *fill factor* (FF). These parameters are given by the current density-voltage (J-V) curve (figure 1.8 shows examples) under illumination. Using these parameters, the *conversion efficiency* (η) can be determined using equation 1.2.

$$\eta = \frac{J_{SC} \cdot V_{OC} \cdot FF}{I} \tag{1.2}$$

The J_{SC} is the current per unit of area that flows through the external circuit if terminals of the solar cell are short circuited. This current depends on the incident solar spectrum and the absorption profile of the solar cell [10]. The V_{OC} is the voltage that is measured when the terminals of the solar cell are not connected to an external circuit. The V_{OC} depends on the bandgap of the absorber material and is influenced by the saturation current density of the solar cell, which is a function of the recombination in the solar cell. Hence, V_{OC} is a measure of the recombination in a solar cell. A high V_{OC} corresponds to a solar cell with a low recombination current [10]. The fill factor is equal to the ratio of the maximum power point (mpp) power ($P_{max} = J_{mpp} \cdot V_{mpp}$) that a solar cell can generate to the product of short-circuit current and open circuit voltage:

$$FF = \frac{J_{mpp} \cdot V_{mpp}}{J_{SC} \cdot V_{OC}} \tag{1.3}$$

Another important parameter of a solar cell is the external quantum efficiency (EQE). EQE measurements can be used to examine the optical and electrical performance of a device. The external quantum efficiency is defined as the fraction of incident photons that generate electron-hole pairs that are successfully collected [10]. The EQE is wavelength dependent and can be measured by illuminating a solar cell with monochromatic light with a known photon flux. When the photocurrent I_{ph} that is generated by the solar cell is measured, the EQE can be calculated using equation 1.4.

$$EQE(\lambda) = \frac{I_{ph}(\lambda)}{q \cdot \Psi_{ph,\lambda}} \tag{1.4}$$

This equation includes the elementary charge q and the spectral photon flux $\Psi_{ph,\lambda}$ of the measurement light beam, incident on the solar cell during the measurement. Because the photocurrent depends on the bias voltage over the solar cell, it is important to keep the bias voltage constant throughout the measurement [10]. If an EQE measurement is used to study the implementation of light management techniques, a reverse bias voltage could be applied to ensure the collection of the majority of the generated charge carriers.

1.5.1. Equivalent Solar Cell Circuit

To obtain insight in the electrical behaviour of a solar cell it is useful to create an electrically equivalent model that consists of basic electronic components. The equivalent circuit for a solar cell with shunt resistance R_p and series resistance R_s is shown in figure 1.7.

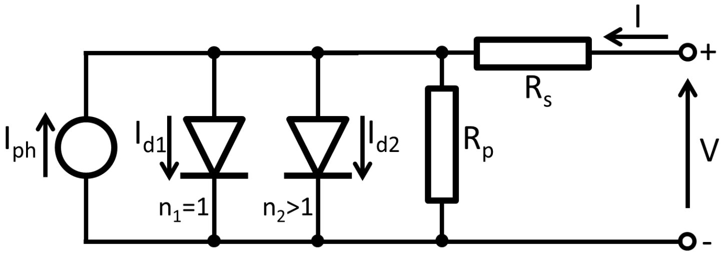

Figure 1.7: Two-diode equivalent circuit of a solar cell, including series and shunt resistance.

The diodes in this circuit represent the *p-n* or *p-i-n* junction in the solar cell. The fill factor of the solar cell is influenced by both the series and shunt resistance. Recombination occurring in the *p-n* or *p-i-n* junction is represented by the two diodes: a diode with ideality factor one and a non-ideal diode with ideality factor greater than one.

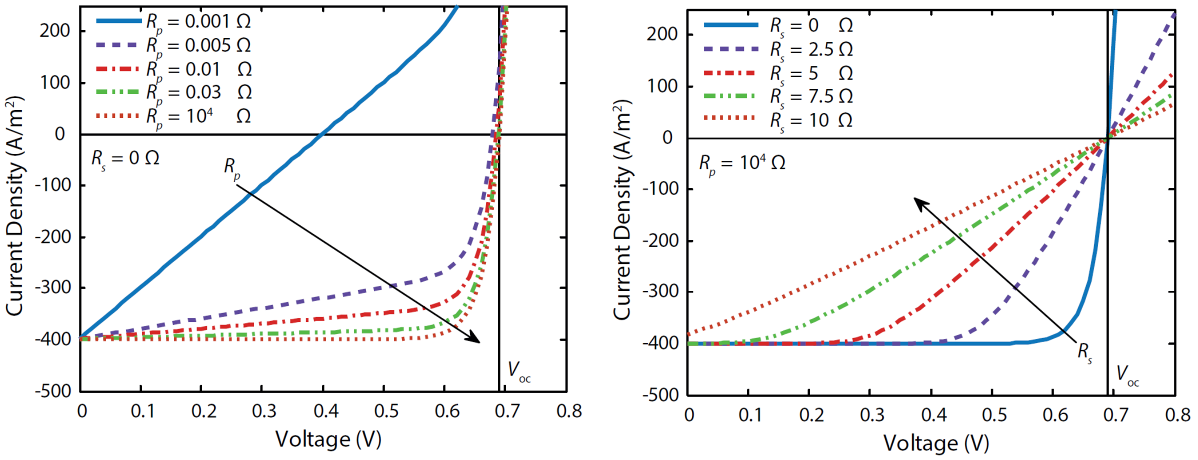

(a) (b)

Figure 1.8: Influence of (a) shunt resistance and (b) series resistance on the J-V curve of a solar cell. Adapted from [10].

The J-V behaviour of the two-diode equivalent circuit can be modelled using a complex equation depending on the series and shunt resistance, the saturation current densities, ideality factors of both diodes, the temperature and the area of the cell. Using that equation it is possible to see the effect of series and shunt resistance on the J-V curve of a solar cell. Figure 1.8a shows J-V curves of a solar cell for different shunt resistances and figure 1.8b shows the curves for different series resistance. When examining J-V curves of produced solar cells this could help to understand where to possibly improve the cell.

1.6. Aim and Outline of This Thesis

Due to the limited thickness of the active layers in thin-film silicon solar cells, light management techniques should be employed in order to enhance the absorption of light. In section 1.4, one of these light management techniques was briefly introduced: the utilisation of textures at the interfaces between different layers of the solar cell.

There are different methods of texturing solar cell interfaces in order to obtain better optical properties, such as an increased optical path length. Either random textures or periodic gratings can be introduced to scatter light into different directions. When different textures or gratings are superimposed, a so-called *modulated surface texture* (MST) is introduced. Random textures, periodic gratings and modulated surface textures will be discussed in more detail in chapter 2. This thesis will focus on the enhancement of light absorption using different substrate textures in *n-i-p* devices. The *n-i-p* configuration was chosen, because such devices have several advantages over cells with a *p-i-n* configuration. The main reasons for choosing the *n-i-p* configuration for this thesis are listed below:

- The substrate material for *n-i-p* solar cells is not restricted by optical properties. Therefore also non-transparent materials can be used [21].
- Due to the absence of a glass superstrate, a 4 % reflection loss at the glass/air interface can be avoided (based on a glass refractive index of $n = 1.5$).

The aim of this thesis is to investigate and optimise different textures and gratings for light trapping purposes. Introducing modulated surface textures by combining random textures and periodic diffraction gratings is of particular interest. Finally, this thesis will discuss the development of a nc-Si:H thin-film solar cell based on such an MST, investigating its effect on the performance of a device. The objective of this work can be summarised by the following statement:

To fabricate and characterise a modulated surface texture substrate based on large, random features, superimposed by smaller, periodic gratings, and to investigate the effect of the substrate on the performance of a nc-Si:H solar cell.

This statement can be subdivided in the following three questions. The structure of this thesis is based on the order of these questions.

1. Is it possible to fabricate an MST structure that consists of a large, random texture, superimposed by a smaller, periodic grating?
2. How do textures, gratings and modulated surface textures influence the propagation of light?
3. Is it possible to fabricate a functioning nc-Si:H solar cell, based on periodic-random MST substrates, and what is the effect of introducing an MST structured back reflector on the performance of an *n-i-p* nc-Si:H solar cell?

This document is structured as follows. Chapter 2 will discuss the concept of light management and gives an overview of the most common techniques that are used in current state-of-the-art solar cells. This chapter will also introduce the temporal coupled mode theory that motivates the use of periodic diffraction gratings. Chapter 3 will describe the methods that have been used during the experimental phase of this thesis project. A brief description of optical characterisation methods and deposition techniques will be presented in this chapter. Chapter 4 presents the results concerning the fabrication and characterisation of different substrates. Optical and morphological properties of random textures, periodic gratings, and modulated surface textures will be discussed. Chapter 5 will discuss the performance of nanocrystalline silicon solar cells that were fabricated on different substrates. Finally, chapter 6 presents the conclusions and recommendations. A summary of the most important results that were obtained during this project will be provided in this chapter.

2

The Importance of Light Management

This chapter will introduce the concept of light management in thin-film silicon solar cells and provides the theoretical background to this thesis. The behaviour of light in absorptive media and different light management techniques will be discussed in sections 2.2 and 2.3, respectively. In section 2.4, properties of random textures and periodic gratings and their impact on light trapping will be explained in detail. Finally, this chapter introduces the concept of modulated surface textures.

2.1. Introduction

The absorption of light in a solar cell is one of the key processes that leads to an electrical power output. An ideal solar cell would absorb all incident light and convert it into electrical energy. The optical performance of a solar cell determines the amount of incident light that is absorbed. There are different techniques that are able to enhance the optical performance of a solar cell. The term *light management* is commonly used to denominate them. More specifically, the aim of light management is to effectively use the energy of the solar radiation. Maximising light absorption in the active layer(s), minimising absorption losses in supporting layers[1] and limiting reflection losses of a solar cell, are the main goals of light management techniques. Light management plays an even more important role in thin-film solar cells, due to the very limited thickness and therefore less absorption of the absorber layer compared to state of the art c-Si devices [7, 21]. It is important to understand why thin layers suffer from low light absorption before employing techniques to increase the absorption. Therefore, a closer look at the behaviour of light in absorptive media is required.

2.2. Light Behaviour in Absorptive Media

The intensity of light travelling through an absorptive medium depends on the optical properties of the material. The optical properties of absorptive media are generally described by their *complex electric permittivity*, $\tilde{\epsilon}$:

$$\tilde{\epsilon}(\lambda) = \epsilon'(\lambda) + i\epsilon''(\lambda) \tag{2.1}$$

Because the refractive index $\tilde{n}(\lambda)$ is defined as the square root of $\tilde{\epsilon}$, this refractive index is a complex number as well [10]:

$$\tilde{n}(\lambda) = \sqrt{\tilde{\epsilon}(\lambda)} = n(\lambda) + i\kappa(\lambda). \tag{2.2}$$

In this expression, $n(\lambda)$ represents the real part of the refractive index. $\kappa(\lambda)$ denotes the imaginary part of the refractive index, which is usually referred to as the *extinction coefficient*. Lambert-Beer's

---

[1] Not all layers in a solar cell contribute to the generation of charge carriers. Layers such as a glass substrate, front and/or back transparent conductive oxide (TCO) layer and metal electrodes are therefore called *supporting layers*.

law describes the behaviour of light propagating inside a medium [10]:

$$I(z,\lambda) = I_0(\lambda) \cdot e^{-\alpha(\lambda)z} \tag{2.3}$$

where $I(\lambda, z)$ is the intensity of the light inside the medium, $I_0(\lambda)$ is the initial intensity at the surface, z is the path length, and $\alpha(\lambda)$ is the absorption coefficient corresponding to the material through which the light propagates. The latter absorption coefficient $\alpha(\lambda)$ is a material property that strongly depends on the wavelength of incident light. This absorption coefficient is related to the wavelength and to the extinction coefficient of the material via:

$$\alpha(\lambda) = \frac{4\pi}{\lambda}\kappa(\lambda). \tag{2.4}$$

The absorption coefficient may differ several orders of magnitude across the wavelength spectrum. A material can therefore be very absorptive at short wavelengths and at the same time almost transparent at long wavelengths. Figure 2.1 shows the absorption coefficients of different silicon-based materials as a function of the photon energy and corresponding wavelength. This figure illustrates the strong wavelength dependency of the absorption coefficient. For semiconductor devices, the absorption coefficient is directly influenced by the band structure. Direct bandgap semiconductors (e.g. CdTe, GaAs) usually have higher absorption coefficients compared to indirect bandgap semiconductors (e.g. a-Si:H, nc-Si:H). Due to the absence of phonon exchange, the light absorption process is more efficient [10]. Equation 2.3 makes clear that the intensity of an electromagnetic wave travelling through a material decreases exponentially as the travelled distance increases.

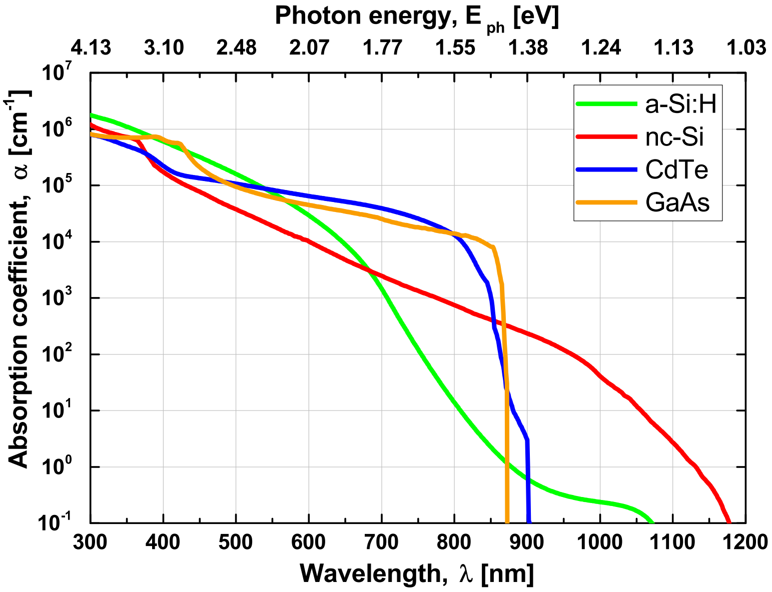

Figure 2.1: Absorption coefficients for a-Si:H (internal measurement, 2015), nc-Si:H [24], CdTe [25] and GaAs [26] as a function of wavelength and photon energy.

Another way to describe the absorptivity of a material for a specific wavelength is the *penetration depth* δ_p. This penetration depth is defined as the depth at which the light intensity has decayed to a fraction $1/e$ of its initial value. When using the penetration depth, Lambert-Beer's law can be written as

$$I(z,\lambda) = I_0(\lambda) \cdot e^{-\frac{z}{\delta_p(\lambda)}}. \tag{2.5}$$

From equations 2.3 and 2.5, an expression for the penetration depth follows:

$$\delta_p(\lambda) = \frac{1}{\alpha(\lambda)} \tag{2.6}$$

As explained in chapter 1, thin-film solar cells make use of active layers with a thickness that is just a fraction of the thickness of a traditional c-Si solar cell. Where state-of-the-art thin-film silicon solar cells have a thickness in the range of a few hundred nanometers to a few micrometers [11], modern c-Si solar cells typically have a thickness around 200 µm [10]. Around the bandgap of c-Si (1.12 eV at 300 K [27]), the penetration depth δ_p increases to the order of millimetres or even centimetres. For penetration depths this great, thin-film solar cells do not have the sufficient thickness required to absorb the majority of the light in the long wavelength range. To enhance the light absorption in thin-film solar cells, light management techniques need to be employed.

2.3. Light Management Techniques

As the aim of light management is to maximise light absorption in the active layer(s) of the solar cell and minimise absorption losses in its supporting layers, it is important to identify the various possible optical loss mechanisms. Optical losses can be caused by non-absorption, thermalisation, reflection, parasitic absorption in supporting layers, incomplete absorption/transmission due to finite thickness, and loss of area. Except for loss of area, each light management technique addresses a specific loss mechanism. In general, light management techniques can be divided into three areas:

- Spectral energy utilisation
- Primary reflectance losses and optical losses in supporting layers
- Light trapping inside absorber layers

2.3.1. Spectral Energy Utilisation

One of the application types where light management plays a role is spectral energy utilisation. Solar cells convert energy in the solar radiation that reaches the Earth into electrical energy. The quantity *spectral irradiance* $I_{e\lambda}$ can be used to describe the solar radiation spectrum. The spectral irradiance quantifies the power per unit wavelength that is incident on the Earth's surface. The AM1.5 spectrum[2] is used as a reference solar spectral distribution as defined in the International Standard IEC 60904-3 [23]. Figure 2.2 provides a graph of the AM1.5 spectrum. The total irradiance of this spectrum is equal to 1000 Wm^{-2}.

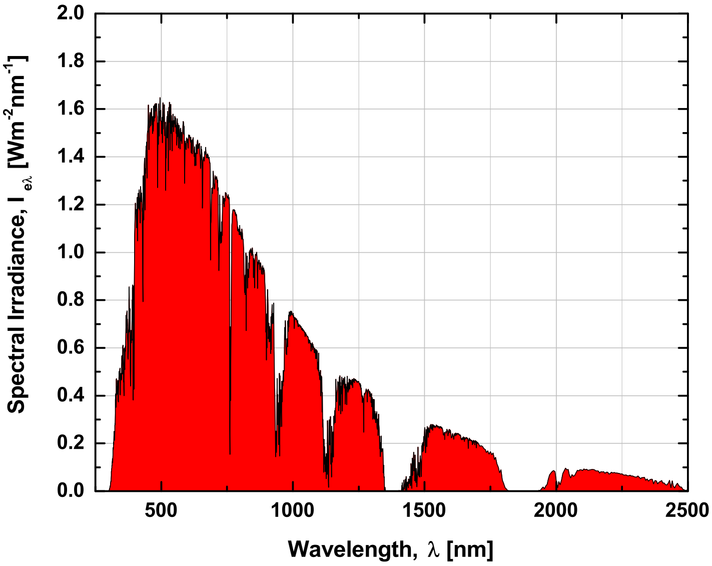

Figure 2.2: Global total spectral irradiance AM1.5. Data adapted from [28].

---

[2] The Air Mass (AM) describes the optical air mass where $AM = \frac{1}{cos(\theta)}$, where θ is the angle between the Sun and the zenith. AM1.5 corresponds to the solar irradiance on a Sun-facing plane surface which is tilted 37° to the horizontal.

The absorber material in a solar cell is usually a semiconductor material that can be characterised by its bandgap energy E_G. Photons that have more energy (E_{ph}) than the bandgap can be absorbed and generate electron-hole pairs. In most cases, photons have a different energy than the bandgap energy of the material. Two energy loss mechanisms arise out of this difference. Electrons and holes are usually occupying energy levels at the top of the valence band and at the bottom of the conduction band [10]. Photons with more energy than the bandgap energy ($E_{ph} > E_G$) release their excess energy as heat in the semiconductor material. This process is called *thermalisation*.

When the energy of photons is lower than the bandgap ($E_{ph} < E_G$), photons are not able to generate electron-hole pairs. In this case, electrons might be excited to a higher energy level, but will never reach the conduction band and will thus return to their initial energy state. This process, which is called *non-absorption*, and the thermalisation process are the two main loss mechanisms in the energy conversion process of solar cells [10]. Because these losses are related to the solar spectrum and the bandgap energy of the semiconductor material, they are referred to as *spectral mismatch* losses.

When no action is taken to reduce the spectral mismatch, these losses will grow to significant numbers. If hydrogenated amorphous silicon (a-Si:H) with a bandgap energy of $E_G = 1.75\ eV$ is used as absorber material, thermalisation losses reach almost 14 % and non-absorption losses increase to 47 %. This means that prior to the energy conversion process, 60 % of the incident irradiance is lost due to spectral mismatch (Figure 2.3a). A common way to reduce the spectral mismatch is making use of *multi-junction* structures (Figure 2.3b). Multi-junction solar cells have been used for many years in the thin-film silicon solar cell industry. These solar cells can be based on two [29, 30], three [31, 32] or more solar cells with different bandgap energies stacked on top of each other. The current world record solar cell (excluding technologies making use of light concentrators) is based on a five-junction cell and reaches an efficiency of 37.8 % under the AM1.5G spectrum [33].

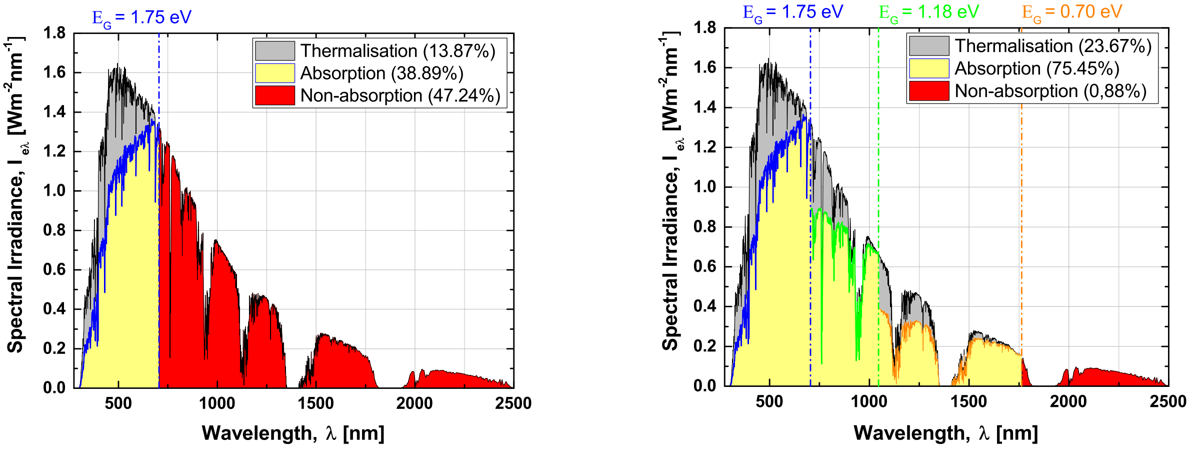

(a) **(b)**

Figure 2.3: (a) Spectral mismatch for an a-Si:H semiconductor and for a (b) multi-junction structure [34].

In order to make effective use of the different bandgap energies, the sub-cells are stacked in a particular order: the widest bandgap in the top cell and the narrowest bandgap in the bottom cell. By stacking the cells in this order, each cell absorbs a particular portion of the electromagnetic spectrum. For instance, the top cell with the widest bandgap will absorb the high energy photons (blue light), while the bottom cell with the narrowest bandgap absorbs the low energy photons (red and near-infrared light).

Combining the a-Si:H device from figure 2.3a with a middle and bottom cell with bandgaps of

1.18 eV and 0.70 eV respectively, results in a multi-junction device. This combination of bandgaps was found to be optimal under 1 Sun illumination by Zeitouny *et al.* [34] when assuming a 0.7 eV Ge bottom cell by simulation. The absorption of the multi-junction device is significantly higher than the absorption of the a-Si:H cell, despite a relative increase in thermalisation losses. This is mainly caused by a high reduction of non-absorption through the use of materials with narrower bandgaps.

For this reason, the application of multi-junctions to reduce the spectral mismatch may seem very attractive. However, designing a multi-junction structure requires some special attention. In single-junction solar cells, the open-circuit voltage (V_{OC}) is ideally fixed once the absorber material is chosen [34]. To increase the efficiency, light management focuses on increasing the short-circuit current density (J_{SC}) by enhancing the absorption in the absorber layer. When multi-junctions are considered, light management focuses on increasing both V_{OC} and J_{SC}. The cells in a multi-junction solar cell are connected in series. The voltage over the multi-junction will thus be the summation of the individual cell voltages, while the current is equal throughout the entire cell. The current density of the multi-junction structure will be limited by the sub-cell that generates the lowest current. To maximise the power conversion efficiency, the sub-cells should have an equal current density at their maximum power point. There are several ways to tune this current density. Changing the layer thickness could be an initial step aimed at increasing or decreasing the light absorption as to generate the desired current density. Increasing the layer thickness of an a-Si absorber, however, increases the effect of light-induced degradation (LID) [35]. Another possible approach is the application of intermediate reflectors [7]. These layers reflect a part of the light (e.g. blue light) and let another part pass (e.g. green and red light). By applying such reflectors, the thickness of the top layer could be reduced, lowering the LID effect.

Another challenge in the design and manufacturing of multi-junction solar cells is that the lattice constants of the various materials are different [10]. When materials with different lattice constants are combined in a multi-junction solar cell, the interfaces between these materials suffer from a lattice mismatch. Not every valence electron can form a bond in this interface, which results in an increased number of dangling bonds. These dangling bonds will act as recombination spots and degrade the cell performance. *Lattice matching* is a method used to solve this problem. When the same lattice constant is chosen for all absorber materials, there will be no interface with an increased number of dangling bonds [10].

2.3.2. Primary Reflectance Losses and Optical Losses in Supporting Layers

A second application of light management focuses on primary reflectance and absorption of light in supporting layers. When incident light reaches a surface between two media with different refractive indices, the light will be partially transmitted and partially reflected. There are two main approaches to reduce reflection at the front surface of a solar cell [36]: (i) using an anti-reflective coating (ARC), and (ii) the use of textured surfaces.

Anti-Reflective Coatings

In order to reduce reflection, two different types of ARC's can be applied. The first method is based on the Fresnel equations in a so-called *Rayleigh film*. The reflection of an interface can be reduced if another layer with refractive index n_1 is introduced between the original media with refractive indices n_0 and n_2 [10]. While every refractive index n_1 that satisfies $n_0 < n_1 < n_2$ will reduce the total reflection, there is an optimum refractive index which is equal to the geometric mean of n_1 and n_2 [36]:

$$n_{opt} = \sqrt{n_0 \cdot n_2}. \tag{2.7}$$

The total reflectivity of a transparent layer with thickness d_1 can be calculated [37] using:

$$R = \frac{r_1^2 + r_2^2 + 2r_1 r_2 \cos 2\theta}{1 + r_1^2 r_2^2 + 2r_1 r_2 \cos 2\theta} \tag{2.8}$$

where r_1, r_2 and θ are given by:

$$r_1 = \frac{n_0 - n_1}{n_0 + n_1}, \qquad r_2 = \frac{n_1 - n_2}{n_1 + n_2}, \qquad \theta = \frac{2\pi n_1 d_1}{\lambda}. \tag{2.9}$$

The expression for the reflectivity in equation 2.8 is at its minimum when $n_1 d_1 = \lambda_0/4$, where λ_0 is the wavelength of light in vacuum. This means that the optimal thickness of the ARC layer is equal to:

$$d_{ARC}^{opt} = \frac{\lambda_0}{4n_1} = \frac{\lambda}{4}. \tag{2.10}$$

The total reflectivity can be plotted versus the refractive index of the ARC material. Figure 2.4 illustrates the effect of adding a layer to an air-silicon interface. For a wavelength of 500 nm, the refractive index of air is $n_0 = 1.0$ and that of silicon is $n_2 = 4.3$. The total reflectivity without an ARC is equal to 38.7 % and can be reduced to approximately 24 % when choosing an optimal refractive index of $n_1 = 2.07$. This example only takes into account one layer of anti-reflective coating, however, it is possible to add more layers in order to reduce the total reflectivity even further. This step wise reduction of the refractive index is called *refractive index grading* [10].

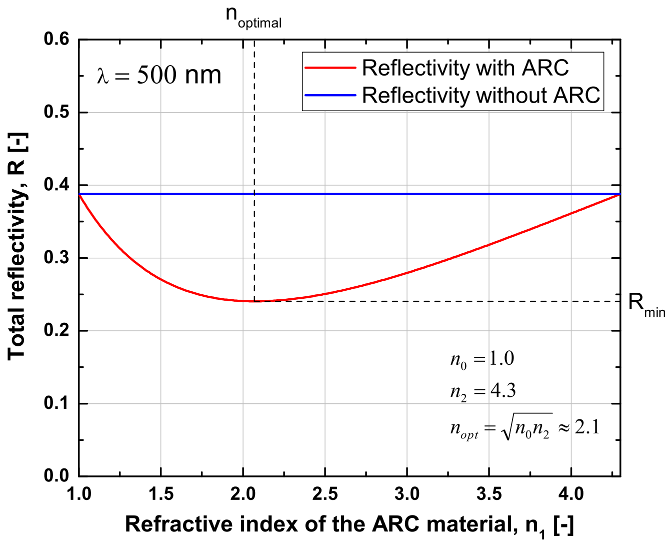

Figure 2.4: Total reflectivity of an air-silicon interface at $\lambda = 500$ nm with and without anti-reflective coating.

An ARC with the optimal thickness (calculated using equation 2.10), is called a *quarter wavelength* ARC. Light that is reflected from the silicon interface reaches the first interface again with a phase shift of 180° [36]. Because these waves are in antiphase, the total amplitude of the reflected wave from the air-ARC material interface is smaller due to destructive interference. The irradiance is proportional to the amplitude of this electromagnetic wave, and therefore the reflected irradiance is reduced as well.

It is important to note that the process of thickness optimisation is particular to each wavelength. The optimal thickness of the ARC will change when another wavelength is taken into account. This means that the maximum reduction of reflectivity is only applicable to a limited band of the spectrum. To broaden this range, a multi-ARC should be applied after carefully choosing multiple materials and tuning their thicknesses [7]. Besides having the right refractive index it is important that the ARC material is transparent and has a large conductivity, if deposited between the TCO and *p*-layer (which can be done for *p-i-n* thin-film silicon solar cells [38]).

Textured Surfaces

Another method to reduce reflection is using textured surfaces. Textured surfaces can be achieved by a anisotropic chemical etching process, which etches a surface at different speeds depending on the etching direction. For a c-Si wafer, this process creates a pyramidal structure where the orientation of the crystal planes define the angles of the pyramids. Usually the silicon surface is parallel to the (100) plane and the intersection of (111) planes forms the pyramids [36]. These pyramids enhance the coupling of light into the device layer and reduce surface reflection. For instance, a part of a normal incident light beam might be reflected to another part of the textured surface, where a fraction of this beam is coupled into the material again. In this way, the front reflection reduces significantly. Besides reducing the front reflection, textured surfaces also contribute to the elongation of the effective path length through the solar cell, and could lead to total internal reflection (section 2.3.3). The principle of surface texturing using pyramid structures is shown in figure 2.5. This case considers the size of the features larger than the typical wavelengths of light so that reflection and transmission of the light beams are fully described by Snell's law and Fresnel equations [10]. The geometrical optics regime is therefore dominant. In thin-film solar cells surface texturing could be introduced at the front TCO layer or by texturing the glass superstrate. The textured interface then consists of craters of different sizes, but the concept of anti-reflection in the geometrical optics regime still holds. In addition to the application of textured surfaces at the air-device interface, surface texturing is also possible for interfaces within the device to reduce reflection.

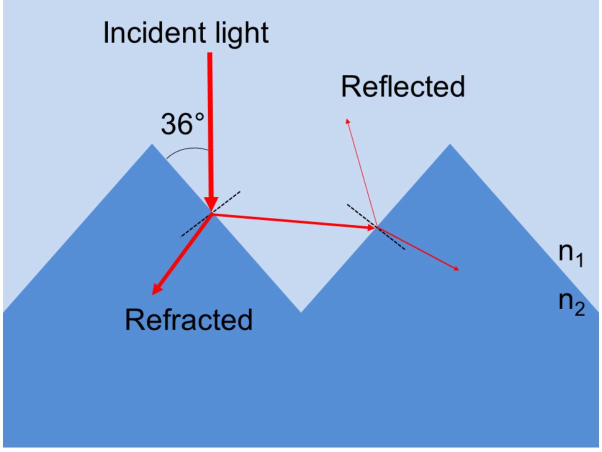

Figure 2.5: The effect of surface texturing with pyramid structures on (100) silicon.

There are, however, some disadvantages associated with textured surfaces. First, these surfaces couple in more of the incident light, including infrared radiation without sufficient energy to generate electron-hole pairs. Light at these wavelengths tends to increase the cell temperature [36]. Second, a disadvantage of textured surfaces is the resulting front contact metal deposition. The so-called metal *busbars* and *fingers* have to follow the sides of the pyramids, increasing the path length. To overcome additional resistive losses, two to three times more metal must be used to maintain the same resistive losses as on a flat surface [36].

Front reflection is not the only source of optical losses. So-called *parasitic absorption* in supporting layers such as TCO layers and doped semiconductor layers leads to additional optical losses. Photons that are absorbed in these layers usually do not generate electron-hole pairs and can therefore be considered as lost. To enhance the energy conversion process, parasitic absorption should be minimised. The development of TCO layers with a low absorption coefficient in the wavelength range of interest for solar cells ($300\,\text{nm} < \lambda < 1200\,\text{nm}$) and a high carrier density, is of uttermost importance [10]. Furthermore, to avoid parasitic plasmonic absorption in metallic back reflectors, alternative solutions to these reflectors are being investigated as well [7].

2.3.3. Light Trapping Inside Absorber Layers

Once photons reach the surface of a solar cell, it is important that they travel to the absorber layer and are trapped inside that layer until they are absorbed. The mechanism that is used to achieve this, is often referred to as *light trapping* and consists of several techniques. The main purpose of light trapping techniques is enhancing the generation of electrons and holes, while keeping the absorber layer as thin as possible. Light trapping techniques can extend the path length of photons through the absorber layer and are therefore able to increase the effective optical thickness. Increasing the optical thickness of a 1 µm thick µc-Si:H absorber layer by 10 or 50 times, results in a photocurrent enhancement of 90 % and 138 % respectively [39]. Specific light trapping techniques, which are usually combined, include [39]:

- In-coupling of photons at the front surface
- Intermediate reflectors in tandem solar cells
- Reflection at the back side
- Scattering at rough interfaces or metallic nano-particles

The first three techniques aim to let the photons reach the absorber layer. The last technique, however, is meant to increase the path length of the photons through the absorber layer. This is related to the design and manufacturing of rough surface textures on a substrate carrier [7].

Light scattering is a physical process in which a light ray is deflected from its original straight path as a result of interaction with small objects. Textured surfaces with feature sizes in the order of micro- and nanometers are able to scatter light. When light is scattered under sufficiently large angles, the phenomenon of *total internal reflection* can occur. Total internal reflection can be explained by applying Snell's law of refraction (equation 2.11). Figure 2.6 illustrates incident, reflected, and refracted light at an interface between two materials with refractive indices n_1 and n_2.

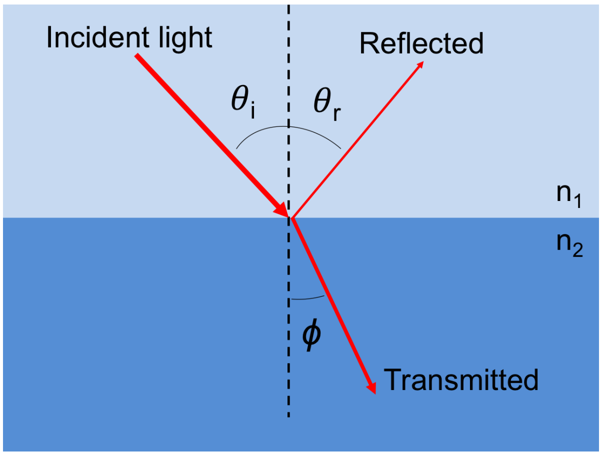

Figure 2.6: Incident, reflected and refracted light rays at an interface between two materials with refractive indices n_1 and n_2.

The behaviour of light at this interface can be explained by Snell's law:

$$n_1 \sin\theta_i = n_2 \sin\phi \tag{2.11}$$

In this equation θ_i is the angle of incidence and ϕ is the angle of refraction with respect to the normal. n_1 and n_2 correspond to the refractive indices of the materials in figure 2.6. Snell's law can be used to express the amplitudes of the reflected and refracted waves in the Fresnel equations. Expressions for both p-polarised and s-polarised light can be derived from these equations. One of the ways to express the amplitude ratios of the reflected waves can be found in equations 2.12 and 2.13, where $n = \frac{n_2}{n_1}$ [40].

$$r_s = \frac{\cos\theta_i - \sqrt{n^2 - \sin^2\theta_i}}{\cos\theta_i + \sqrt{n^2 - \sin^2\theta_i}} \tag{2.12}$$

$$r_p = \frac{-n^2\cos\theta_i + \sqrt{n^2 - \sin^2\theta_i}}{n^2\cos\theta_i + \sqrt{n^2 - \sin^2\theta_i}} \tag{2.13}$$

Rearranging equation 2.11 gives:

$$\sin\phi = \frac{1}{n}\sin\theta_i \tag{2.14}$$

When $n > 1$ the amplitude ratios r_s and r_p in equation 2.12 and 2.13 are real for all values of θ_i. However, if $n < 1$ there will be values of θ_i such that $\sin\theta_i > n$, and thus $\theta_i > \sin^{-1} n$. The angle $\sin^{-1} n$ is called the *critical angle* θ_c. For larger values of θ_i, the amplitudes in equations 2.12 and 2.13 become complex. The reflectivity R can be calculated using equation 2.15.

$$R_s = |r_s|^2 \qquad\qquad R_p = |r_p|^2 \tag{2.15}$$

When r_s and r_p are complex, the total reflection R is equal to 1. This means that for $\theta_i > \theta_c$ all light is being reflected back into the medium. For a glass-air interface, the reflectance as a function of the angle of incidence is shown in figure 2.7.

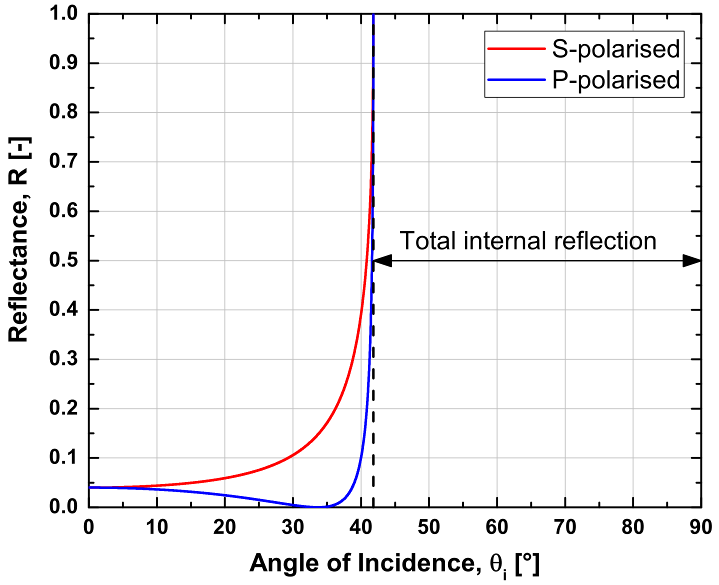

Figure 2.7: Reflectance of s- and p-polarised light at a glass-air interface with $n_{glass} = 1.5$ and $n_{air} = 1.0$. The critical angle is equal to $\theta_c = 41.8°$. For angles of incidence larger than the critical angle, total internal reflection occurs.

Total internal reflection is particularly useful in thin-film solar cells. When light is scattered at angles larger than the critical angle at the back reflector, light could be trapped in the absorber layer until it has been fully absorbed. Even when the angles that result from scattering at the back surface are smaller than the critical angle, the optical path of the light through the absorber layer is elongated. This increases the chance of absorption.

As explained, light scattering is deflecting light rays from their original path by interaction with small objects. Light scattering can be accomplished by introducing nano-textured interfaces. These interfaces can be applied to both front and back surfaces. In current *p*-*i*-*n*-type solar cells, the surface texture of the top TCO layer through which the light enters the cell is the most important for scattering [41]. For this front TCO, usually tin oxide (SnO_2) layers are used, sometimes doped with fluorine (FTO) or zinc oxide (ZnO) [7, 39, 41, 42]. In current *n-i-p*-type solar cells, the back surface is mainly responsible for light scattering. This could be a textured metallic back contact on which the solar cell is deposited. Often, scattering surfaces are based on a random texture. An alternative approach to the scattering of light is making use of periodic gratings or implementing modulated surface textures (MST). Modulated surface textures combine two or more different surface textures with various geometrical properties [39]. MST's allow light scattering at multiple wavelengths due to the their different feature sizes. Periodic gratings are also referred to as angle-selective scattering mechanisms, and introduce the possibility of (pre-)selecting scattering angles [7].

2.4. Random Textures and Periodic Gratings

In state-of-the-art thin-film silicon solar cells, light is usually scattered at surfaces with a random texture [7]. The random texture approach has been successfully employed for years in thin-film silicon modules [43]. Random textures that scatter incident light are often based on sub- or superstrate carriers that are covered with a randomly etched TCO layer. Fluorine-doped tin oxide (FTO) and aluminium-doped zinc oxide (AZO) are examples of TCO layers used to obtain a randomly textured surface. The Japanese company Asahi Glass Company (AGC) produces glass substrates coated with an etched FTO layer, introducing pyramidal-like features on the substrate carrier. Wet-etched AZO introduces a random texture with a crater-like structure. Scanning electron microscope (SEM) images of two random textured front TCO's can be seen in figures 2.8a and 2.8b.

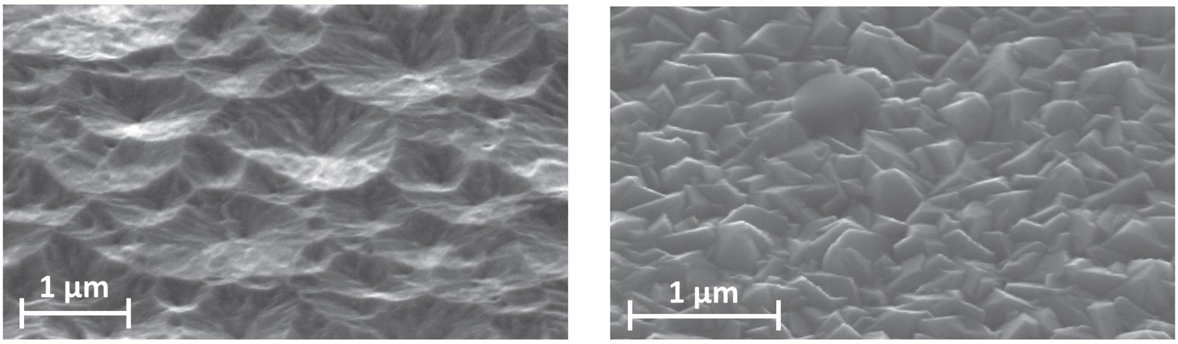

(a) **(b)**

Figure 2.8: SEM images of random textures by (a) wet-etched AZO and (b) Asahi U-type (FTO). Adapted from [7].

Despite the fact that random textures could lead to excellent scattering properties, the current world record conversion efficiencies for a-Si:H/nc-Si:H multi-junction solar cells are set by cells based on periodic gratings [18, 30, 31]. Periodic gratings could be either 1- or 2-dimensional (1D or 2D) and may have different lattice structures and duty cycles. Figure 2.9a shows a 1D periodic grating, and figures 2.9b and 2.9c show two possible lattice structures that could be used when employing 2D periodic gratings. The duty cycle of a 1D grating is defined as the dimension of a feature divided by the period of the grating. The duty cycle of a 2D grating is obtained by dividing the covered area in the unit cell (black squares) by the area of the unit cell (marked by red lines). For solar cell applications, periodic gratings can be fabricated using different techniques, such as (electron beam) lithography, laser scribing, or nano-imprint lithography [7]. The so-called *honeycomb* grating on which the current world record a-Si:H/nc-Si:H tandem cell is based involves a photolithography process combined with a wet etching step [44].

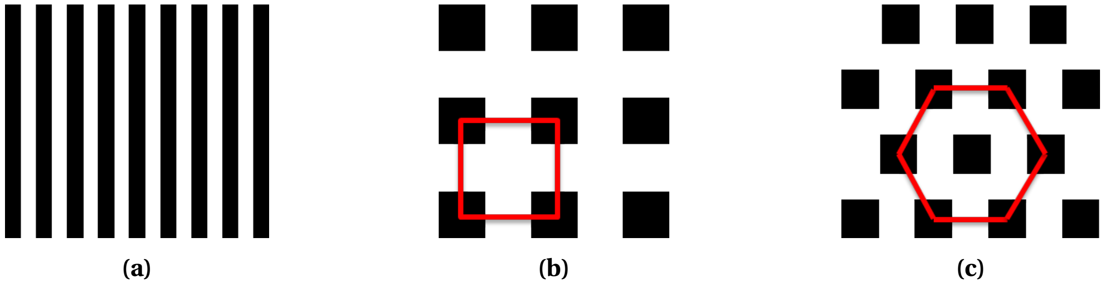

Figure 2.9: Three possible grating configurations: (a) 1D grating with a duty cycle of 0.5, (b) 2D grating with a square lattice structure, and (c) 2D grating with a hexagonal lattice structure.

Besides the different processes that are required to produce random and periodic substrates, the main difference is the way that they scatter incident light. State-of-the-art random textures can fully randomise the incident light and scatter it to wide angles and into a continuum of modes [7, 43]. A texture that fully randomises incident light can theoretically lead to an absorption enhancement factor of $4n^2$, where n is the refractive index of the absorber material. This enhancement factor is also known as the famous *Yablonovitch limit* or *bulk limit* [45]. One of the key points in the derivation of the Yablonovitch limit is that effects that arise from the wave-optics regime can be ignored. This results in the following assumptions that were used to derive the bulk limit [45–47]:

- The film thickness is much larger than the wavelength
- Random textures or periodic gratings, with a period much larger than the wavelength, are used for light trapping
- The single pass absorption is negligible

Periodic gratings with a period similar to the wavelength result in angle selective scattering, in which incident light is scattered to a finite number of angles. The general principle of light absorption enhancement using periodic gratings was shown by Sheng *et al.* [48] in 1983. In this way, a finite number of diffraction orders inside the absorber layer are excited. The direction of these diffraction orders can be predicted by using equation 2.16, also known as the *grating equation*.

$$n_1 sin(\theta_{1m}) = n_2 sin(\theta_{2m}) = \frac{m\lambda}{L} \tag{2.16}$$

In this equation, θ is the angle of propagation, m is the diffraction order and L is the period of the grating. Gratings can be used for light trapping if they are designed such that the largest part of the incident light is coupled into diffraction modes with an angle larger than the critical angle. In this way, light propagates outside the escape cone of the material and will be trapped. The angle selective scattering by diffraction gratings with small periods is a result of the wave effects of light. Since the bulk limit was derived with the assumption that the wave-optics effects can be ignored, this limit is not strictly applicable in this case.

Yu *et al.* [49] developed a formalism to calculate the absorption limit of grating structures, using the so-called *temporal coupled-mode (TCM) theory.* In 2010, Yu *et al.* [47] showed that periodic gratings with a hexagonal lattice structure can increase the maximum absorption enhancement, exceeding the bulk limit by applying the statistical temporal coupled mode theory.

2.4.1. Temporal Coupled Mode Theory

In the temporal coupled mode theory, light trapping is explained by the coupling of incident plane waves into guided resonances. This can be achieved by using a grating with periodicity L that is in the order of the wavelength of the incident plane wave. Each incident plane wave can be coupled to at least one guided resonance at this condition. A plane wave that is coupled into a guided resonance is called a *channel*. In addition to the coupling of plane waves into resonances, there is coupling of resonances to the channels that carry the incident plane waves. These channels are called the *leakage channels*. The number of guided resonances is indicated with M and the number of leakage channels is indicated with N [49]. A single resonance has a very narrow bandwidth. By summing the contributions of all single resonances to the total absorption, the upper limit of absorption can be calculated using equation 2.17 and the definitions from equation 2.18.

$$A = \frac{2\pi\gamma_i}{\Delta\omega}\frac{M}{N} = \frac{2\pi n\gamma_i}{c\Delta k}\frac{M}{N} = \frac{2\pi\alpha}{\Delta k}\frac{M}{N} \tag{2.17}$$

$$k \triangleq \frac{2\pi n}{\lambda}\frac{c}{c} = \omega\frac{n}{c} \quad \text{and} \quad \gamma_i \triangleq \alpha\frac{c}{n} \tag{2.18}$$

In these equations γ_i is the intrinsic resonance loss rate due to material absorption, $\Delta\omega$ is the frequency range, α is the absorption coefficient of the material, and k is the (angular) wave number [47, 49].

The enhancement factor F is defined as:

$$F = \frac{A}{A_{SP}} \tag{2.19}$$

where the single pass absorption A_{SP} is equal to $1 - e^{-\alpha d}$. This expression is reducible to αd following the assumption that the single pass absorption is negligible. Substituting these entities in equation 2.19 results in the following expression for the enhancement factor [47]:

$$F = \frac{A}{\alpha d} = \frac{2\pi\gamma_i}{\alpha d\Delta\omega}\frac{M}{N} \tag{2.20}$$

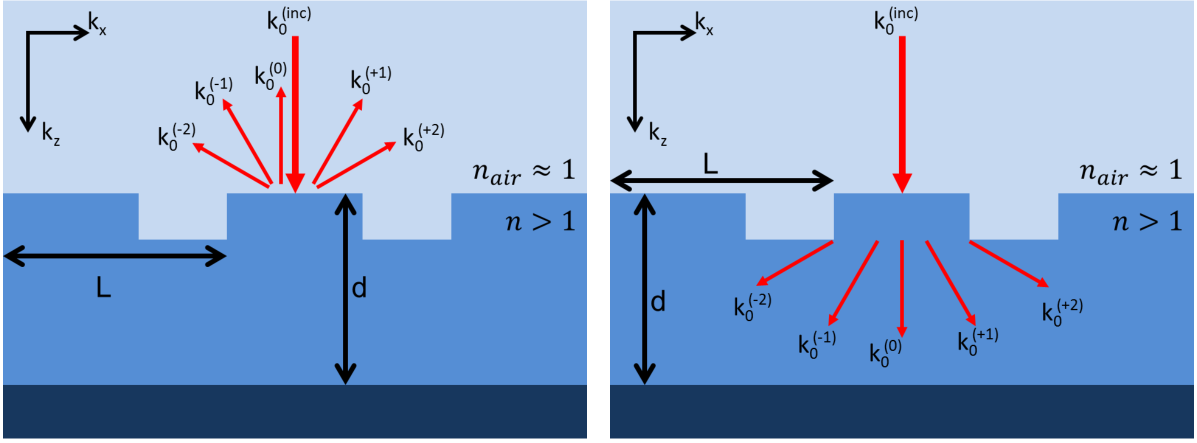

(a) **(b)**

Figure 2.10: Visual representation of plane waves coupled into (a) leakage channels, and (b) resonances by a 1D grating.

For a film with thickness d, endowed with a 1D grating with period equal to L, the leakage channels are visualised in figure 2.10a. In this case, normal incident light is considered. The periodicity of the structure results in plane waves that couple into leakage channels with $k_x = 0, \pm 2\pi/L, \pm 4\pi/L, \ldots$. These plane waves propagate in air, which means that $k_x \leq k_0$ [47]. The number of leakage channels at a certain wavelength λ can be obtained by using equation 2.21,

$$N = 2\left\lfloor \frac{k_0}{2\pi/L} \right\rfloor + 1 = 2\left\lfloor \frac{L}{\lambda} \right\rfloor + 1 \tag{2.21}$$

where $\lfloor x \rfloor$ is the largest integer smaller than x. When $L >> \lambda$, equation 2.22 can be used to approximate the number of leakage channels [47].

$$N = \frac{2k_0}{2\pi/L} = \frac{2L}{\lambda} \tag{2.22}$$

Figure 2.10b shows the plane waves that are coupled into guided resonances for a single polarisation. The guided resonances M in the film as a function of wave vector k, are visualised in the k-space in figure 2.11b. The number of resonances is obtained by equation 2.23 [47].

$$M = \frac{2\pi k \Delta k}{(2\pi/L)(2\pi/d)} = \frac{2n^2\pi\omega}{c^2}\left(\frac{L}{2\pi}\right)\left(\frac{d}{2\pi}\right)\Delta\omega \tag{2.23}$$

This equation is only valid when the refractive index, n, is sufficiently high, such that:

$$\begin{cases} \lambda/n << L \\ \lambda/n << d \end{cases}$$

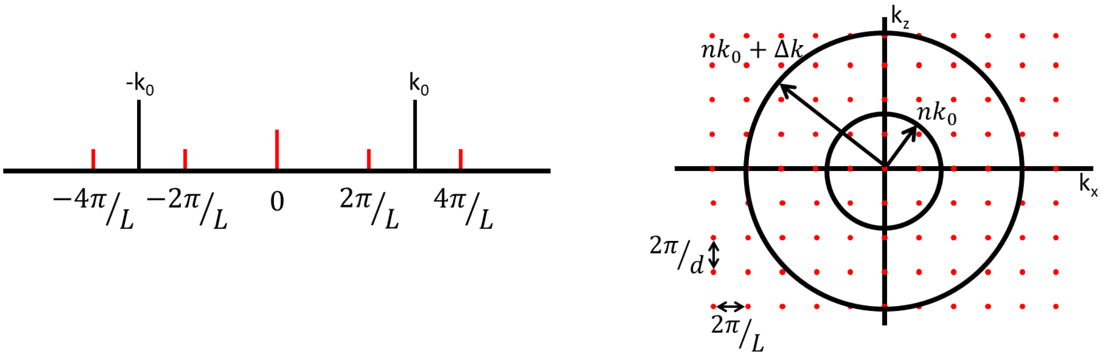

(a) **(b)**

Figure 2.11: (a) Leakage channels and (b) resonances excited by a 1D grating in the k-space. The red lines and dots represent the leakage channels and guided resonances respectively [47].

The upper limit enhancement factor can now be calculated by the insertion of N and M in the result of equation 2.20. When $L >> \lambda$, this results in πn. When $L \approx \lambda$ (such that $\lfloor L/\lambda \rfloor = 0$), the upper limit enhancement factor becomes $2\pi n$. These enhancement factors are significantly lower than the conventional Yablonovitch limit of $4n^2$, because there is only a limited number of guided resonances [47]. To increase the number of guided resonances, and thus the enhancement factor, a 2D grating can be used.

For a 2D square lattice periodic grating, the number of leakage channels and guided resonances increases. Leakage channels are propagating plane waves in air, which are coupled into channels with a spacing of $2\pi/L$, in both x- and y-directions. The number of leakage channels for a 2D square lattice grating is estimated by equation 2.24 for $L >> \lambda$, where the factor 2 takes both polarisations into account.

$$N_{2D} = 2 \cdot \frac{\pi k_0^2}{(2\pi/L)^2} = \frac{2\pi\omega^2}{c^2}\left(\frac{L}{2\pi}\right)^2 \tag{2.24}$$

The number of guided resonances supported by the film in the frequency range $[\omega, \omega + \Delta\omega]$, is equal to [47, 49]

$$M_{2D} = \frac{8\pi n^3\omega^2}{c^3}\left(\frac{L}{2\pi}\right)^2\left(\frac{d}{2\pi}\right)\Delta\omega \qquad \text{for} \begin{cases} \lambda/n << L \\ \lambda/n << d \end{cases} \tag{2.25}$$

Equation 2.20 results in an absorption enhancement factor F of $4n^2$ when $L >> \lambda$. In fact, a random texture could be viewed as a periodic grating with a structure that never repeats, i.e. $L \to \infty$. The resulting enhancement factor perfectly reproduces the conventional bulk limit for a perfect random texture. However, when $L \approx \lambda$, the absorption enhancement factor is equal to $4\pi n^2$, a value significantly higher than the bulk limit. Enhancement factors beyond the conventional bulk limit can be reached for a wide range of wavelengths [47]. However, when the number of leakage channels is small (i.e. when $L \approx \lambda$), a strong angular dependency exists. A graph of the enhancement factor as a function of grating period over wavelength is shown in figure 2.12 for normal incident light.

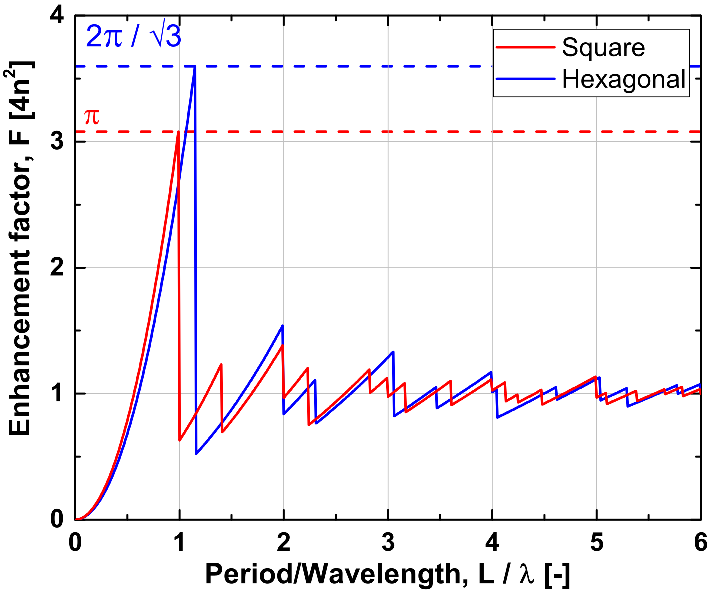

Figure 2.12: Enhancement factor F for a square and hexagonal lattice structure. The enhancement factor is normalised to the $4n^2$ limit.

When a hexagonal lattice is used instead of a square lattice, the maximum absorption enhancement factor can be increased even more. The distance between two leakage channels in a square lattice is $2\pi/L$. In a hexagonal lattice structure this distance increases to $(2/\sqrt{3})\cdot 2\pi/L$. The wavelength range in which the hexagonal lattice grating operates with only 2 leakage channels is thus larger than to the square lattice structure. Therefore, the maximum absorption enhancement factor increases to $F = 8n^2\pi/\sqrt{3}$ for a hexagonal lattice structure [47].

Using the temporal coupled mode theory for light absorption enhancement, Yu *et al.* [47] introduced a new absorption enhancement limit in 2010, higher than the Yablonovitch limit. Exceeding the Yablonovitch limit is possible in a broad range of wavelengths when using 2D grating structures. This enhancement, however, has a very strong angular dependency.

2.4.2. Modulated Surface Textures

As pointed out in this section, both periodic gratings and random textures have the possibility to be employed in advanced light trapping structures. Battaglia *et al.* [43] have shown that both random pyramidal textures on ZnO and periodic nanocavities can lead to high initial conversion efficiencies of 10.9 %. As both light trapping mechanisms have been proven effective, it remains a controversial question whether periodic or random structure are better suited to yield optimal results [43].

Another well known light management technique is the use of modulated surface textures. As briefly introduced in section 1.6, MST's arise when two or more surface textures with different characteristic dimensions are combined. One way of manufacturing an MST is to stack multiple layers, while introducing a different texture in each layer. If the layers are thin enough, the texture of the individual layers will be transferred to the next interface [50]. The top layer of the stack will contain the morphological surface characteristics of all individual layers. Figure 2.13 shows a stack of three interfaces with the modulated surface texture as a result. When geometrical features with different dimensions are combined, higher levels of light scattering could be reached over a broader wavelength range compared to one individual morphology [50].

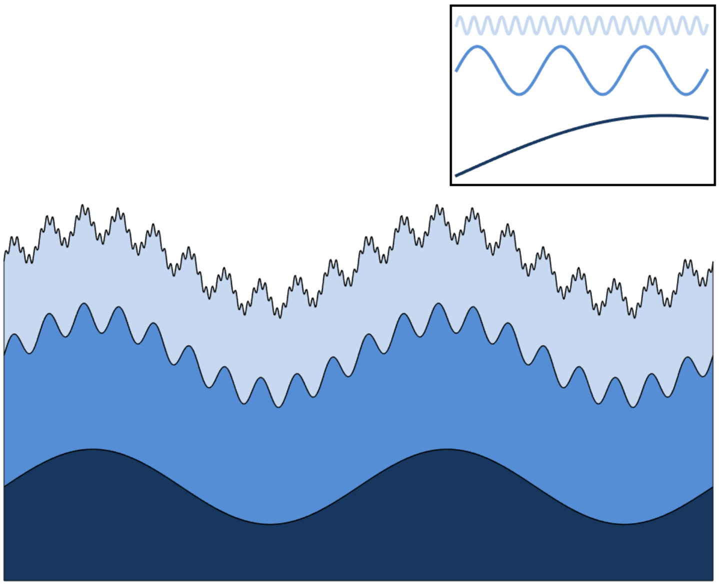

Figure 2.13: Example of a modulated surface texture containing three periodic structures, individually visualised in the right top of the figure.

Although figure 2.13 shows an MST based on periodic structures only, MST substrates could consist of only random textures, or a combination of textures and gratings. A record initial efficiency of 14.8 % of a a-Si:H/nc-Si:H tandem solar cell was obtained by Tan [51] based on an MST consisting of two different random textures. Wet-etched glass was used as the first layer of the modulated surface texture with features in the order of 1 to 5 µm. A hydrogen-doped indium oxide (IOH) layer and a nano-textured i-ZnO layer were deposited on top of the etched glass, resulting in an MST consisting of micro and nano features. Isabella [7] obtained MST's using wet-etched glass and a wet-etched ZnO:Al layer, resulting in a single-junction a-Si cells with a significantly higher current density compared to cells on flat glass superstrates.

Another possible MST configuration is a combination of a relatively large periodic grating at the bottom and a smaller random texture on top. This combination was investigated by Isabella [7] in 2012. A lacquer-based laser-scribed 1D grating with a period of 1000 nm was used. On top of the grating a 1 µm ZnO:Al layer was sputtered and wet etched, resulting in a random/periodic MST. The result of combining random and periodic structures was broad angular light scattering combined with diffraction orders at specific diffraction angles. In 2015, Sai *et al.* [31] fabricated a record efficiency triple-junction a-Si:H/µc-Si:H/µc-Si:H solar cell based on a 2D grating, combined with the intrinsic nano roughness of the µc-Si layer. This 2D grating incorporated a hexagonal grating structure, which is known as a *honeycomb-textured substrate*. These substrates have shown excellent light trapping behaviour and have lead to a significant increase in the total current density of the fabricated triple-junction cell [31].

Due to the work of the previously mentioned researchers and others, substrates based on modulated surface textures have become a well-established method for light trapping enhancement. Despite the extensive research in this field, there are still two unexplored possibilities of building an MST structure. Modulated surface textures based on multiple periodic gratings with different periods have not been reported yet. Research on combining gratings with different periods focused on using decoupled front/back gratings [52]. By applying a large-period grating on the back side of a solar cell and a small-period grating on the front side, light in-coupling of both gratings could be exploited.

Finally, modulated surface textures based on relatively large random textures with superimposed smaller periodic gratings have not yet been explored either. Combining the broadband light scattering of a random texture with angle selective scattering of a periodic grating has proven to contribute significantly to the performance of solar cells [31]. Using a micro-texture instead of the nano-texture that was used by Sai *et al.* [31] could result in higher V_{OC} and FF in nc-Si:H solar cells [53]. This work aims at using the wet-etched glass that was used by Tan [51], and superimpose a periodic grating in order to obtain a modulated surface texture. Table 2.1 shows an overview of the different modulated surface textures that were discussed in this section. This table also indicates which type of structures were used to fabricate the modulated surface texture stack.

Table 2.1: Overview of modulated surface texture stacks discussed in this section. *Large* and *small* refer to the relative feature dimensions that are used.

		Small	
		Periodic grating	**Random texture**
Large	**Periodic grating**	Not reported	Isabella [7] Sai *et al.* [31]
	Random texture	This work	Isabella [7] Tan [51]

3

Fabrication and Characterisation Techniques

This chapter presents an overview of all techniques that were used during the manufacturing and experimental phases of this work. The first section will explain all deposition and microfabrication techniques that were used to create the substrates and solar cells. The second section will focus on the experimental methods that were required to characterise samples and to evaluate the manufacturing process.

3.1. Deposition and Microfabrication Techniques

3.1.1. Radio-Frequency Magnetron Sputtering

In section 1.4, front and back transparent conductive oxide (TCO) layers were introduced as important layers in thin-film solar cells. Besides using a TCO layer as a highly transparent and conductive layer, this work introduced TCO layers for glass texturing purposes as well. The TCO layers that were deployed during this project were: indium tin oxide (In_2O_3:Sn, ITO) and aluminium-doped zinc oxide (ZnO:Al, AZO). These TCO layers were deposited using radio-frequency (RF) magnetron sputtering. RF magnetron sputtering allows the deposition of thin films on a substrate by bombarding a target material with highly energetic atoms or ions.

ITO layers were sputtered using a Polyteknik AS cluster tool [54]. Figure 3.1a presents a schematic overview of the deposition chamber, and figure 3.1b shows a picture of the cluster tool in the EKL cleanroom. In this system, Argon gas is used as a sputter gas, and an ITO target consisting of 10 % SnO_2 and 90 % In_2O_3 was used for the deposition of the ITO layers. Sputtering power, heater temperature, deposition pressure, and input gas composition could be adjusted in a deposition recipe. A plasma frequency of 13.56 MHz was maintained during all depositions. A major advantage of using an RF power supply, instead of a direct current (DC) power supply, is that the sample is alternately attacked by ions and electrons. This avoids a build-up of charge at non-conducting samples, such as glass [7].

AZO films were sputtered in a multi chamber thin-film plasma processing cluster tool in the EKL cleanroom, which will be elaborated in section 3.1.4. This cluster tool consists of six deposition chambers, of which one is used for sputtering of AZO. The same plasma frequency and working principles, used in the Polyteknik cluster tool, are used for AZO sputtering in this chamber. This chamber contains a target consisting of 2 % Al_2O_3 and 98 % ZnO.

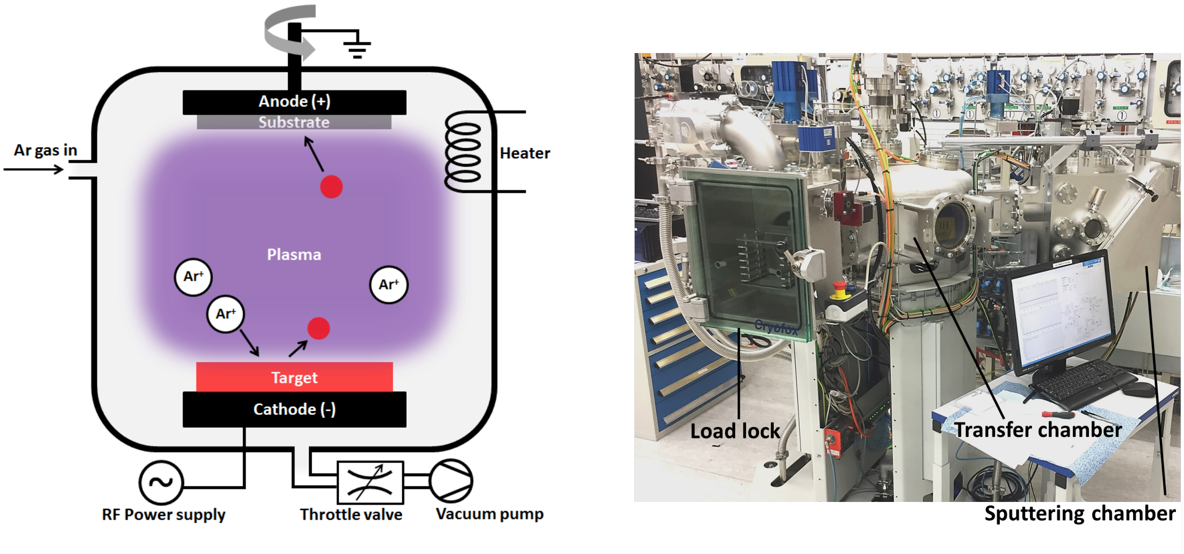

(a)

(b)

Figure 3.1: (a) Schematic overview of the deposition chamber for RF magnetron sputtering, and (b) picture of the Polyteknik AS cluster tool in the Else Kooi Laboratory (EKL) cleanroom.

3.1.2. Glass Texturing by Wet Etching

Randomly textured glass substrates were obtained by wet etching using the following procedure. Corning glass (10x10 cm^2, Eagle XG) was thoroughly cleaned for 10 minutes in ultrasonic baths, with acetone and isopropanol (IPA) consecutively. Glass substrates were dried in a nitrogen flow and mounted in sample holders for ITO sputtering. This cleaning procedure was very important to obtain high quality ITO layers. ITO layers (150-250 nm) were sputtered using a power of 200 W in the sputtering tool in the EKL cleanroom. These ITO layers acted as a sacrificial layer to initiate the etching process. Simultaneously, ITO acted as a catalyst for the etching reaction, increasing the etching speed. Textured glass substrates were obtained by etching samples in a solution of HF (49wt%) and H_2O_2 (31wt%) with a volume ratio HF:H_2O_2:H_2O of 1:2:10. Samples were etched for 30 minutes and were rinsed and cleaned in deionised (DI) water. After drying the samples in a nitrogen flow, they were cleaned in ultrasonic baths with acetone and IPA, again for 10 minutes.

3.1.3. Electron Beam and Thermal Evaporation

Metal layers that were used as a back reflector and as front and back contacts in solar cells were obtained by electron beam (e-beam) and thermal evaporation. Both techniques involve the evaporation of metal under a high vacuum, and condensation of metal on the substrate. The low pressure in the chamber avoids contamination of the film by undesirable residual gases, and increases the mean free path length of metal atoms [55]. To increase the uniformity of the metal layer, a slowly rotating (10-20 rpm) sample stage is used during the evaporation process [55]. Metal evaporation has several advantages over metal sputtering. Generally, a higher deposition rate can be achieved, and less damage is done to the surface of the substrate when thermal evaporation is used [7].

E-beam evaporation technique uses a high energetic electron beam that is focused on a heat resistant crucible containing a target material. A magnetic field is used to control the focal point of the electron beam. The thermal evaporation technique on the other hand, uses a crucible through which a high current flows. This crucible will heat up and reaches a temperature beyond the melting point of the target material.

It is important to monitor the layer thickness and deposition rate during the evaporation process. A quartz crystal deposition rate monitor (QCM) is often used to observe and control the rate during evaporation [55]. The quartz crystal is made of a piezoelectric (PTZ) material that changes its volume when a voltage is applied. If a high frequency voltage is applied, the quartz crystal will oscillate with a frequency depending on the crystal size, mass, and orientation [55]. When a metal layer is evaporated onto the crystal surface, the mass of the crystal changes, resulting in a different oscillation frequency. Based on this change in frequency, deposition rate and film thickness can be monitored. The QCM can be included in a feedback system that regulates the current through the boat, and power of the electron beam, to accurately control the metal evaporation rate [55].

In this work a Provac PRO500S [56] metal evaporation tool was used. Figure 3.2 shows a picture of this metal evaporator in the EKL cleanroom. This tool can process up to four 10x10 cm^2 substrates simultaneously. Both e-beam and thermal evaporation techniques can be used in the PRO500S system. The e-beam evaporation technique is used for titanium, silicon dioxide, chromium and aluminium. The desired target material can be selected by rotating a circular crucible with four pockets. Thermal evaporation is used to obtain layers of silver. Both evaporation sources include a shutter to control when to start and stop the deposition sequence. For back reflectors and solar cell back contacts, a full area deposition was used. For the front contacts of solar cells, metal was evaporated using a shadow mask to obtain a metal front grid. Back contacts, that also act as back reflectors, were deposited as a stack of 500 nm Al / 30 nm Cr / 300 nm Ag. For samples that only required a back reflector, 300 nm Ag was used.

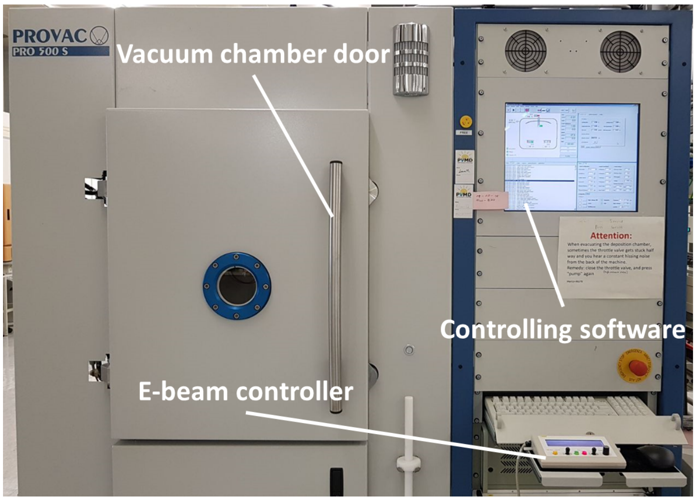

Figure 3.2: Provac PRO500S metal evaporation tool in the EKL cleanroom (photo courtesy of Mr. Y.F. Zhao).

3.1.4. Plasma Enhanced Chemical Vapour Deposition

Silicon layers that were used in this work were deposited by an RF plasma enhanced chemical vapour deposition (PECVD) process. The PECVD process deposits thin layers of material from a gas state (e.g. SiH_4) in the reaction chamber to a solid state (eg. a-Si:H) on the substrate. Gases that are lead into the chamber are called *precursor gases*. Depending on which precursor gases are present in the process chamber during deposition, silicon layers can be made intrinsic, *n*- or *p*-doped, both in amorphous or nanocrystalline state. The PECVD process allows deposition of high quality films at relatively low operating temperatures, around and below 200 °C [10]. A plasma is created between two electrodes in an ultrahigh vacuum (UHV) reaction chamber to start the deposition process. One of these electrodes is grounded, the other electrode is connected to an alternating current (AC) power supply (either RF or very high frequency (VHF)). Precursor gases flow into the deposition chamber through a showerhead electrode, which is a perforated, metal electrode. The precursor gases will get ionised in the plasma and generate different particles such as ions, neutral atoms, molecules, and electrons [10]. Generated particles will interact with the substrate, which results in the deposition of a thin film of material. The quality and structure of the thin layers can be controlled by varying different parameters, such as the plasma frequency, pressure, substrate temperature, electrode distance, and gas-phase composition [21]. Figure 3.3 shows a schematic overview of a PECVD process chamber.

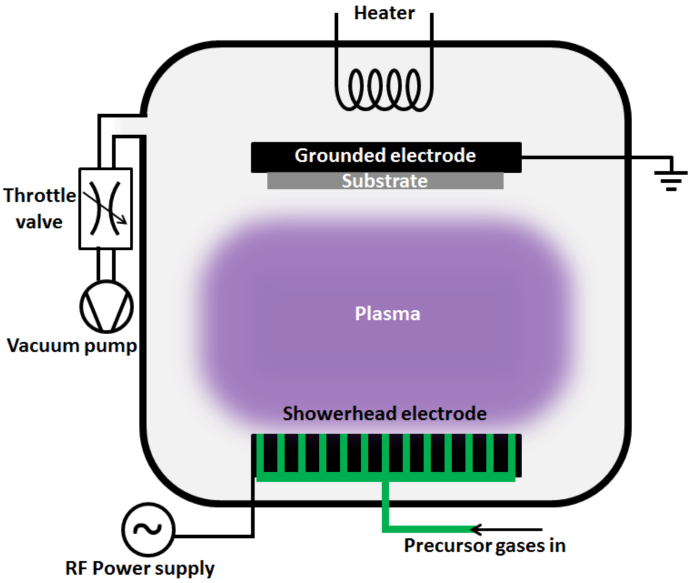

Figure 3.3: Schematic overview of a deposition chamber for PECVD processes.

The PECVD cluster tool used in this work was located in the EKL cleanroom. This so-called *AMIGO* deposition tool by Elettrorava S.p.A. [57] contains six deposition chambers and a loadlock chamber, connected to a central transfer chamber. A robot arm is installed to move samples between different deposition chambers through the transfer chamber. This ensures that there is no break of vacuum and undesired oxidation can be avoided. For depositions of *p*- and *n*-type a-Si:H and a-SiO_x:H layers, the frequency of the AC power supply was fixed at 13.56 MHz. For the deposition of nc-Si:H layers, a VHF of 40.68 MHz was applied.

3.1.5. Ultraviolet Photolithography

Periodic gratings on flat glass and periodic gratings for modulated surface textures were obtained by an ultraviolet (UV) photolithography process. UV photolithography is a method to transfer a geometrical pattern from a mask to a light sensitive polymer, known as *photoresist*. Prior to photoresist coating, samples were heated to 150 °C using a hotplate and exposed to an Hexamethyldisilazane (HMDS) vapour prime process for 7 minutes. HMDS vapour priming promotes the adhesion of the photoresist to a sample. Samples were coated with photoresist using a spin coating process (figure 3.4a). The sample was attached to a vacuum chuck in a spin coating tool. A Brewer Science Apogee manual spin coater [58] was used to apply the photoresist layer. This spin coater allowed spin speeds between 0 and 6000 rpm. The thickness of the photoresist layer depends mainly on the rotational speed and time of the spin coating process.

After the HMDS process, samples were completely covered with SPR3012 positive photoresist [59], using the static dispense method. The spin coating procedure consisted of a low speed step (500 rpm, 10 s) and a high speed step (2250 rpm, 30 s) with an intermediate acceleration of 1000 rpm/s. This resulted in a photoresist layer of approximately 1200 nm. After the spin coating process, samples were exposed to a soft baking step of 2 minutes at 95 °C to reduce the solvent concentration in the resist, and to obtain a stable photoresist layer (figure 3.4b). Samples were then transferred to a Karl Suss MA6 contact mask aligner [60] in the EKL facility. A short optimisation study was carried out to find the right exposure parameters, resulting in an exposure time of 10 s. After mounting the mask in the mask holder, the low vacuum contact mode was used for exposure (figure 3.4c). The basic operating principle that allows pattern transfer is a change in solubility of the photoresist in a developer solution. Photoresist contains a *photoactive compound* (PAC) that makes the photoresist sensitive to light. A common PAC used in photoresists is diazonaphtoquinone (DNQ) [61]. DNQ molecules (not soluble in a developer) absorb UV light in the range of 350-450 nm, allowing a chemical reaction that forms a compound known as carboxylic acid (very soluble in developer). The difference in solubility between unexposed and exposed photoresist forms the basis of patterning the photoresist [61].

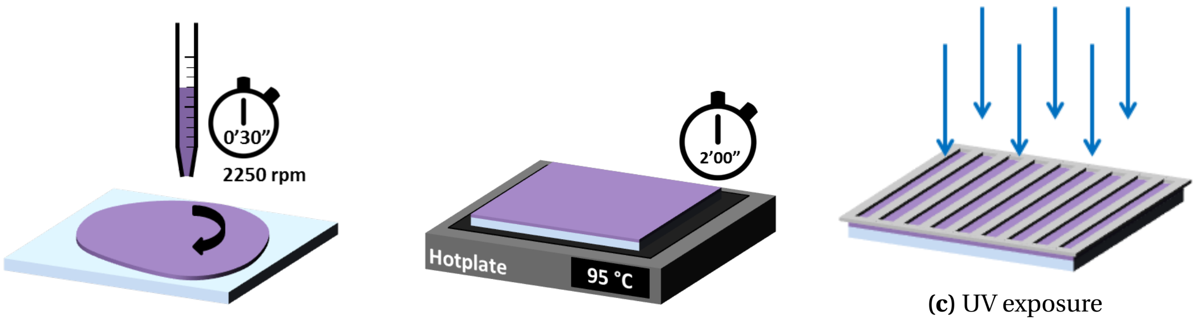

(a) Spin coating photoresist.

(b) Soft baking.

(c) UV exposure (low vacuum contact).

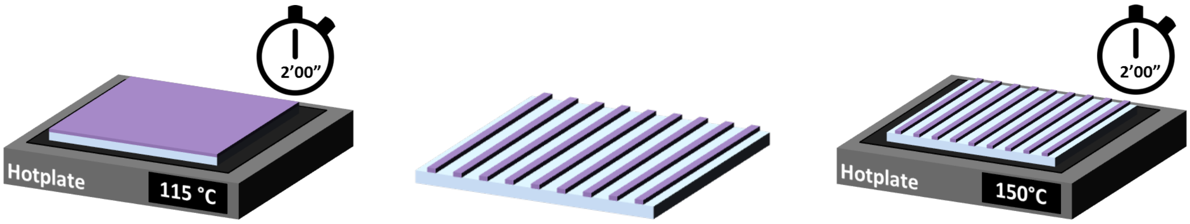

(d) Post exposure baking.

(e) Development.

(f) Hard baking.

Figure 3.4: Photoresist steps to obtain periodic gratings (one-dimensional in this figure) or modulated surface textures.

Samples were subjected to a post exposure baking step for 2 minutes at 115 °C to reduce standing wave effects, caused by interference in the film during exposure (figure 3.4d). After 5 minutes of cooling down, the photoresist was developed using MF322 developer [62] for 70 seconds (figure 3.4e). After development, samples were carefully rinsed in DI water, and dried in a nitrogen flow. Samples were placed on a hotplate for a final hard baking step. This step lasted for 2 minutes at 150 °C, to obtain more thermal stability of the photoresist pattern for further processing (figure 3.4f).

3.2. Characterisation Techniques

3.2.1. Atomic Force Microscopy

Atomic force microscopy (AFM) is a scanning probe microscope technique to study the surface morphology of a sample. A sharp, reflective, metallic tip, that is attached to a cantilever, is used to scan the surface of a sample. A scanning electron microscope (SEM) image of the AFM tips used in this work is shown in figure 3.5b. A laser beam that is incident on the top side of this tip is reflected onto a photodiode. When the tip travels near the surface of a sample (several nm distance), forces between the surface and the tip deflect the cantilever, causing the reflection of the laser beam on the photodiode to shift.

Samples are mounted on a piezoelectric (PZT) stage that can move in x-, y- and z-directions. The PZT stage moves during the scan, while the tip stays in a fixed position. A closed loop control system moves the PZT stage in the z-direction, based on the tip deflection that is measured by the displacement of the laser beam on the photodiode. The average distance between AFM tip and surface is kept constant by the control system. The AFM setup is schematically visualised in figure 3.5a. There are different modes in which an AFM setup can operate. The *contact* or *static* mode, ensures that the tip is in full contact with the surface of the sample. The surface morphology can be studied with atomic scale resolution, however, the sample could get damaged due to strong friction between tip and sample [63]. In *non-contact* mode, the cantilever usually vibrates with a frequency close to the resonance frequency. Forces between AFM tip and surface will influence the vibration frequency, phase, and amplitude, from which the surface morphology can be reconstructed [63]. The final operation mode is the *semi-contact* or *tapping* mode. This is a combination of the static and non-contact mode. The AFM tip will only touch the surface at maximum deflection of the cantilever. This mode minimises friction between tip and surface, and harms the surface less than the contact mode [63].

In this work, an nTegra NT-MDT atomic force microscope [64] was used. Monocrystal silicon tips with polysilicon cantilevers of NT-MDT HA_NC type [65] (≤ 10nm tip radius, 30° tip cone angle) were used in semi-contact mode. Scans of maximum 100x100 µm^2 were allowed, with a fixed number of points of 128x128, 256x256 or 512x512. The surface was scanned line by line until a full area 3D plot could be presented. Scan speeds and frequencies were always kept below 50 µm/s and 1 Hz. Non-conductive samples were covered with a 20 nm Ag layer to avoid charge build-up at the surface. Data were analysed with Gwyddion V2.49 software [66].

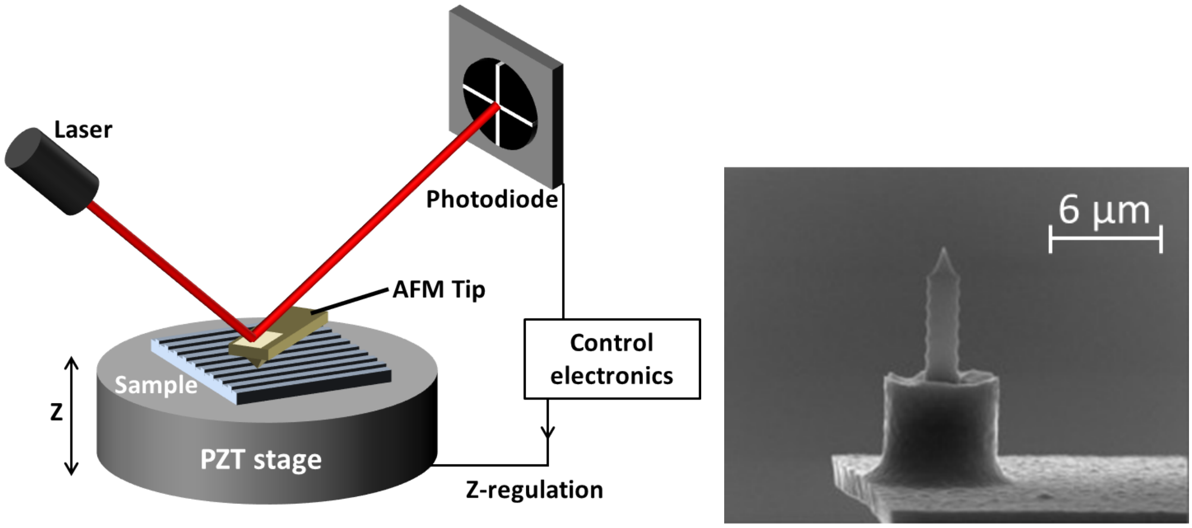

(a) (b)

Figure 3.5: (a) Schematic of an atomic force microscopy setup. (b) SEM image of an NT-MDT HA_NC AFM tip with the reflective side pointing downwards. Adapted from [65].

3.2.2. Spectrophotometry

Optical characterisation of samples was done by using spectrophotometry. Spectrophotometers are able to measure the intensity of a light beam as a function of the wavelength. This technique allows measurements of direct and diffuse reflectance, transmittance, and angular intensity distribution (AID). The wavelength range in which a spectrometer operates is usually divided into three sub-ranges: near infrared (NIR), visible light (Vis) and UV. In a typical spectrophotometer, light from a halogen (NIR, Vis) or deuterium (UV) light source travels via mirrors and a filter wheel to a diffraction grating. The incident radiation is dispersed to produce a spectrum. By rotating the diffraction grating, the desired wavelength can be reflected onto a slit, which restricts the output spectrum to a near-monochromatic beam [67]. In so-called *single beam* spectrophotometers, the beam is then reflected onto the sample. The reflected or transmitted light is measured and compared to the calibration spectrum. When a so-called *double beam* spectrophotometer is used, the light beam leaving the diffraction grating is split into a measurement and reference beam. The intensity of the measurement beam that is transmitted or reflected by the sample is then compared to the intensity of the reference beam. In both cases, measured spectra are reported in relative terms (i. e. percentages).

A double beam Lambda 950 spectrophotometer by Perkin Elmer [68] was used in this work. This spectrophotometer contains a deuterium arc lamp for the UV region and a tungsten-halogen lamp for the Vis and NIR regions. Overall, a spectrum from 175 nm to 3300 nm can be covered with this spectrophotometer with a small resolution (UV/Vis ≤ 0.05 nm, NIR ≤ 0.20 nm) [7, 11, 67]. Different accessories can be connected to the spectrophotometer: the Integrating Sphere (IS) by Perkin Elmer and the Automated Reflectance/Transmittance Analyser (ARTA) by OMT Solutions B.V. [69]. Both accessories contain two detectors, embedded in the internal walls of the integrating spheres: a thermoelectrically-cooled lead sulfide (PbS) detector (NIR) and an extended range photomultiplier tube (UV/Vis) [67, 70]. The detectors switch at a wavelength of 860.60 nm, the weakest region for both detectors [7]. Figure 3.6a shows the Lambda 950 spectrophotometer with the IS accessory mounted and figure 3.6b shows the ARTA accessory.

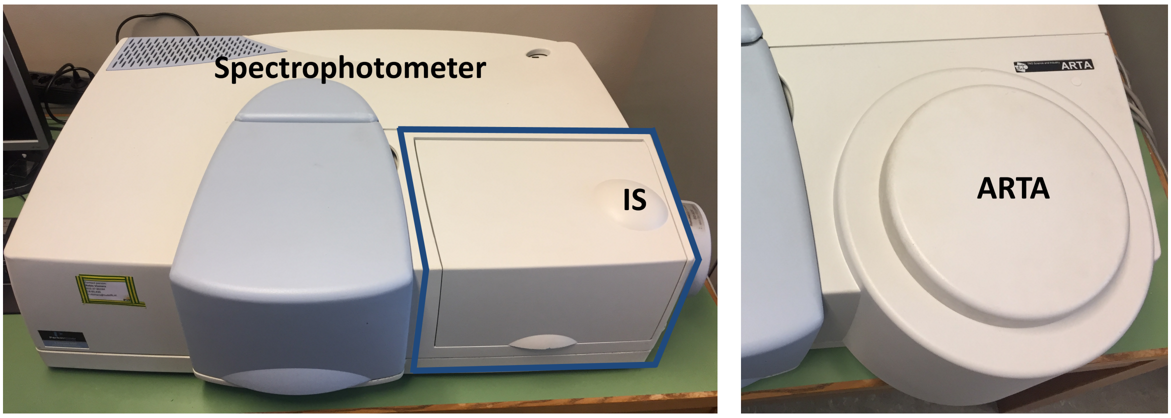

(a) **(b)**

Figure 3.6: Perkin Elmer Lambda 950 spectrophotometer with (a) the IS accessory, and (b) the ARTA accessory mounted

The IS accessory contains an integrating sphere with a diameter of 150 mm. The internal surface of the sphere is coated with Spectralon® [71] [1]. The IS accessory has two ports in which a sample can be placed: a transmittance port and a reflectance port (figure 3.7a). Total transmittance (T_T) measurements can be obtained by placing a small Spectralon® disk at the reflectance port. For diffuse transmittance (T_D) measurements, the Spectralon® disk can be removed, leaving a hole through which the specular component of the transmitted light can leave the sphere. Similarly, total reflectance (R_T) and diffuse reflectance (R_D) can be obtained by placing a sample at the reflectance port. In- or excluding a removable part of the integrating sphere distinguishes between the dif-

---

[1] Spectralon® is a highly diffuse, reflecting material that behaves like a Lambertian surface. A Lambertian surface scatters light in all directions, following Lambert's cosine law: $I = k \cdot \cos\theta$, where I is the intensity of light, k is a proportionality factor and θ is the scattering angle [7, 11]

fuse and total reflectivity. When total transmittance and reflectance of a sample are measured, it is straightforward to calculate the absorption in a sample: $A_{sample} = 1 - R_T - T_T$.

To evaluate how much transmitted or reflected light is diffuse, and how much is direct, the *haze* parameter is introduced. When the total and diffuse components of reflection or transmission are both known, it is possible to calculate this haze parameter. Haze for transmitted light $H_T(\lambda)$ can be calculated using equation 3.1. Similarly, the haze of reflected light $H_R(\lambda)$ can be calculated by dividing the diffuse reflected light $R_D(\lambda)$ by the total reflected light $R_T(\lambda)$.

$$H_T(\lambda) = \frac{T_D(\lambda)}{T_T(\lambda)} \tag{3.1}$$

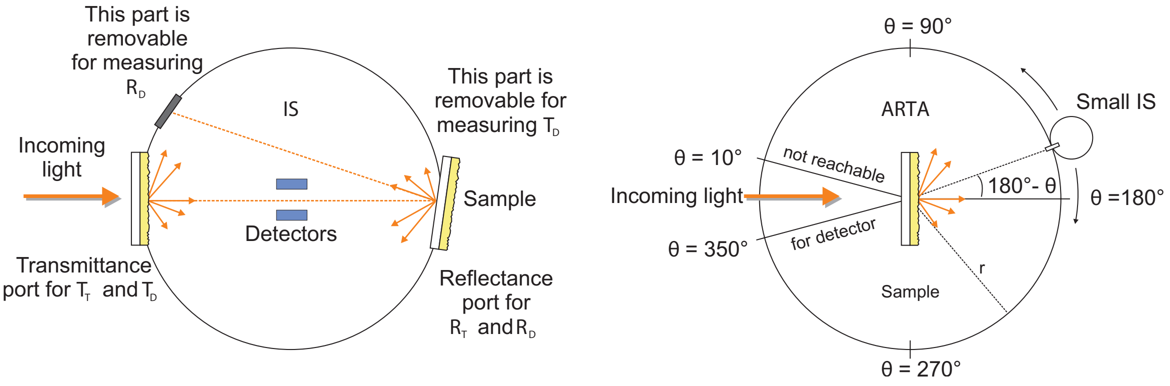

(a) **(b)**

Figure 3.7: Sketches of the (a) IS and (b) ARTA accessories for the Perkin Elmer Lambda 950 spectrophotometer. Adapted from [7].

The ARTA accessory consists of a drum (320 mm diameter) in which a small integrating sphere is mounted. This small integrating sphere can rotate in the horizontal plane, driven by a motorised rotation stage. The reference beam arrives at the integrating sphere through a mixed fibre bundle that contains 50% UV/Vis fibres and 50% Vis/NIR fibres to cover the whole UV/Vis/NIR range [70]. This fibre bundle is mounted in a flexible cable guide that limits the bending of the fibres. A sample is placed on a second, motorised rotation stage in the centre of the drum. Because both the sample stage and the detector stage can rotate, it is possible to measure specular transmission (T_S) and reflection (R_S) at different angles of incidence [7]. A sketch of the ARTA accessory is shown in figure 3.7b. The internal surface of the drum is black to avoid stray-light [70]. Using this setup, the intensity of scattered light as a function of scattering angle and wavelength can be obtained. ARTA measurements result in the angular intensity distribution (AID) of a sample. The ARTA accessory measures the absorbance A, which is related to the AID via:

$$AID(\lambda, \theta) = 10^{-A(\lambda,\theta)}. \tag{3.2}$$

For anisotropic samples, the AID is a function of the azimuth angle ϕ as well. Repeating measurements for different azimuth angles would be required. Before measuring with the ARTA accessory, a calibration without a sample is required, so that $A \equiv 0$ [7].

3.2.3. Spectroscopic Ellipsometry

Ellipsometry is an optical measurement technique that is based on the polarisation state of light that is reflected or transmitted by a sample. The term ellipsometry originates from the fact that linear polarised light often changes to an elliptical polarisation state upon light reflection [72]. Ellipsometry refers to single-wavelength ellipsometry, in which a monochromatic light source is used.

Spectroscopic ellipsometry (SE), however, makes use of broadband light sources [11]. SE can be used to investigate dielectric properties of thin films, such as complex refractive index or dielectric function. This technique can also be employed to study the roughness, thickness, composition, and other material properties of thin films [21]. In this work, SE was mainly used to investigate the thickness of photoresist and ITO layers.

An ellipsometry setup measures the amplitude ratio Ψ and phase difference Δ between p- and s-polarised light waves. Because direct interpretation of these values is complicated, the construction of an optical model is required for data analysis [72]. During measurements, linearly polarised light illuminates a sample from an angle of incidence larger than 0° (normal incidence). The specular component of the reflected light falls on a detector that is positioned symmetrically to the light source [11]. If the optical model is defined properly, model parameters can be fitted to measured data in order to obtain the desired characteristics of the sample. Because ellipsometry is a non-destructive and non-contact measurement technique, allowing accurate characterisation of thin films, it is widely used in different fields of application.

In this work, a J.A. Woollam ESM-300 spectroscopic ellipsometer, an M-2000DI lamp power supply and an EC-400 electronics control module [73] were used. This ellipsometer contains two light bulbs to ensure a broadband light source: a deuterium light bulb and a Quartz-Tungsten-Halogen (QTH) light bulb. This light source is mounted on a robotic arm that can change the angle of incidence. Reflected light from the sample falls onto a detector unit that is mounted on a second robotic arm, symmetrically positioned with respect to the first robotic arm. This detector unit contains two detectors, one for NIR light, and one for UV/Vis light. In figure 3.8, a picture of the SE setup in the measurement room is presented.

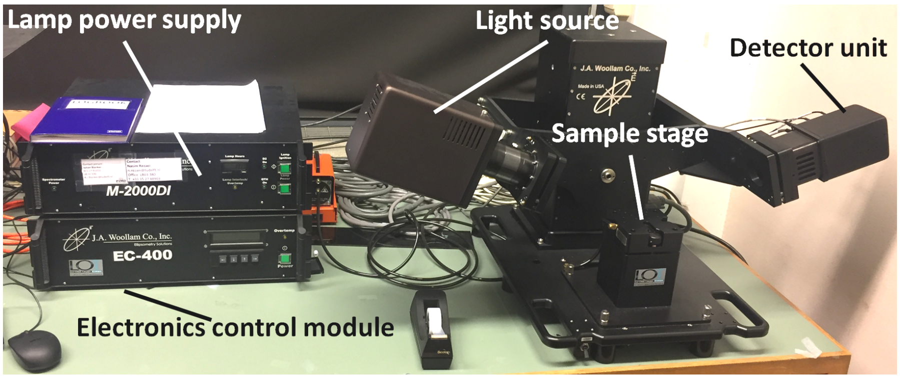

Figure 3.8: J.A. Woollam ESM-300 Spectroscopic Ellipsometer in the PVMD measurement room.

3.2.4. Illuminated Current Density-Voltage

As explained in section 1.5, the performance of a solar cell depends on sol-called external solar cell parameters. Many of these external parameters are determined by the current density-voltage (J-V) characteristics of a solar cell. From J-V measurements, open-circuit voltage (V_{OC}), short-circuit current density (J_{SC}), fill factor (FF), and efficiency (η) can be extracted. To obtain reliable results, it is important to carry out the measurements under standard test conditions (AM1.5 spectrum, 1000 W/m^2, 25 °C). A solar simulator is used to produce the required spectrum and intensity. Usually, a temperature controlled sample stage is used to keep the temperature of the solar cell at 25 °C.

In this work, a class AAA Wacom WXS-156S-10,AM1.5G continuous solar simulator [74] was used in this work to measure the J-V curves and external parameters of fabricated solar cells. This solar simulator contains xenon and halogen light bulbs to simulate the entire AM1.5 spectrum. Although the spectrum of the solar simulator does not exactly match the AM1.5 spectrum, spectral matching is within a 25 % range for every 100 nm wavelength increment. Two Fraunhofer ISE monocrystalline Si reference cells were used to verify the spectral match of the solar simulator. If necessary, the power of the light source could be slightly adjusted to obtain better spectral matching. All measurements were carried out using a shadow mask with the dimensions of fabricated cells (4x4 mm^2 or 1x1 cm^2). This was done to avoid generation of charge carriers in areas that were not part of the devices. Samples were placed on a temperature controlled sample stage and were connected using two probes. During illumination, a sweep of the the operating voltage was obtained by changing the load resistance. Plotting all measurement points resulted in a J-V curve corresponding to the device under test. A typical J-V curve is shown in figure 3.9. The maximum power point is indicated by *mpp*.

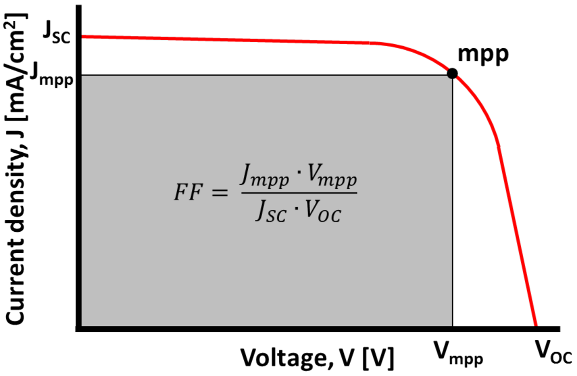

Figure 3.9: Typical illuminated J-V Curve for a solar cell. External parameters are indicated along the axes.

3.2.5. External Quantum Efficiency

The external quantum efficiency (EQE) is defined as the fraction of photons generating electron-hole pairs in the solar cell that can be successfully collected [10]. EQE measurements can be used to analyse whether light management techniques are successfully employed in a solar cell. The EQE of a solar cell can be obtained by illuminating the device under test with monochromatic light and measuring the generated photocurrent. The photon flux of this monochromatic light should be known for each wavelength. A calibrated photodiode could be used to determine this photon flux. Using the measured photocurrent, $I_{ph}(\lambda)$, and the spectral photon flux, $\Psi_{ph,\lambda}$, the EQE of the device can be calculated using equation 3.3, that was briefly introduced in section 1.5.

$$EQE(\lambda) = \frac{I_{ph}(\lambda)}{q \cdot \Psi_{ph,\lambda}} \tag{3.3}$$

Besides the external quantum efficiency, it is possible to obtain a value for the photocurrent density (J_{ph}). This value can be calculated using equation 3.4, where $\Phi_{AM1.5G}(\lambda)$ is the spectral photon flux of the AM1.5G spectrum. Values for J_{ph} obtained by a continuous solar simulator are generally less reliable due to incorrect area definitions or generation of charge carriers outside the defined device area [7].

$$J_{ph} = -q \int_{\lambda_{min}}^{\lambda_{max}} EQE(\lambda) \cdot \Phi_{AM1.5G}(\lambda)\, d\lambda \tag{3.4}$$

External quantum efficiency results for fabricated cells were obtained using an in-house built spectral response setup. This setup consists of a 150 W xenon arc light source, in an Apex illuminator with a motorised filter wheel, and a Newport Oriel Cornerstone 130 monochromator [75] to produce monochromatic light. The monochromator contains two gratings that can be rotated in order to select the desired wavelength. Measurements were taken in a range from 300 nm to 1150 nm in steps of 10 nm. The filter wheel contains three different high pass filters that filter out any undesired high orders.

To distinguish between an offset current and the photocurrent that is generated by the solar cell, light is chopped by a chopper wheel that rotates at a certain frequency. A lock-in amplifier is used to remove the offset current and to improve the signal/noise ratio. In the setup that was used, monochromatic light reached a chopper wheel rotating at a frequency of 123 Hz via a system of mirrors. The measurement beam was focused in a small spot ($\leq 3\,\mathrm{mm}$ diameter) on the device under test via a second system of mirrors.

This device under test was connected to a Signal Recovery 7225 DSP lock-in amplifier [76] via a small in-house built filtering circuit. The chopper wheel controller produced a reference signal at the frequency of the chopper wheel rotation, and sent it to the lock-in amplifier. Using this reference signal, the lock-in amplifier only amplified the signal corresponding to the photocurrent of the device under test. Software that was developed in-house within the LabVIEW platform [77] was used to control the measurement setup. For measurements that required a bias voltage, a Kepco BOP 100-1M power supply [78] was used. A schematic overview of the spectral response setup is presented in figure 3.10. The spectral photon flux of the measurement light source was measured using a silicon photodiode that is regularly calibrated by Fraunhofer ISE.

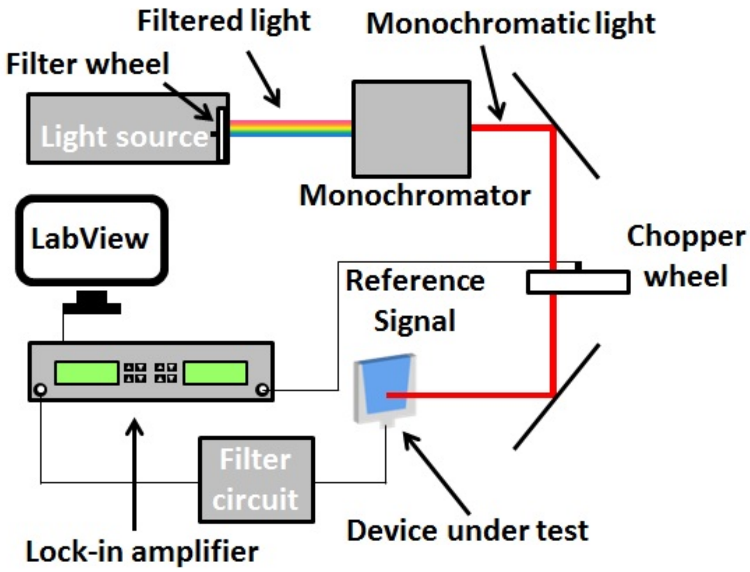

Figure 3.10: Schematic overview of the external quantum efficiency measurement setup used in this work.

4

Substrate Fabrication and Characterisation

This chapter presents the results of the fabrication and characterisation of various substrates, in the same order as the fabrication process. Morphological and optical characteristics will be discussed in separate subsections. The first section contains the results of random textured substrates. In the second section, results for substrates based on periodic gratings will be discussed. The third section will elaborate on the results of modulated surface texture (MST) substrates. Finally, the fourth section will compare different substrates in terms of their effect on light absorption. This chapter will answer the first two questions that were introduced in section 1.6.

4.1. Random Textures

Section 2.3 explained that the inclusion of random textures in thin-film silicon solar cells can significantly increase the efficiency, by reducing front reflection and enhancing light trapping inside absorber layers. Chapter 3 introduced the technique that was used to fabricate random textured substrates. This methodology was first reported by Tan *et al.* [53]. After the first indium tin oxide (ITO) depositions and wet etching steps, non-uniform textured samples were obtained. Therefore, ITO uniformity optimisation was necessary.

4.1.1. ITO Uniformity Optimisation

The uniformity of random textures on glass substrates depends mainly on the uniformity of the sputtered ITO layer. The Polyteknik cluster tool allows rotation of substrates during deposition, to increase the uniformity of sputtered layers. Tan *et al.* [53] used a different, Kurt J. Lesker RF magnetron sputtering system for the deposition of ITO layers. Because the configuration of this system differs significantly from the Polyteknik tool used in this work, different deposition parameters were required. When the optimal deposition parameters reported by Psomadaki [79] were used, the etching step removed the complete ITO layer, without etching the glass substrates. The etching of the glass substrate starts at the ITO grain boundaries. The formation of grains in ITO layers depends on deposition parameters such as substrate temperature, layer thickness and gas mixture. At deposition temperatures lower than 150 °C, ITO layers were found to be amorphous [80]. The lack of grain boundaries could have been the reason why the glass was not affected by the wet etching step. The substrate temperature was increased to 150 °C to obtain the first textured glass substrates. Due to a different distance and orientation of the target relative to the substrate, the deposition power was lowered, in order to achieve a similar power density to that used in the Kurt. J. Lesker deposition tool.

The sample that is shown in figure 4.1a was obtained by using the initial deposition parameters listed in the table 4.1. It is evident that this sample does not display a uniformly distributed texture. To improve uniformity, first, the rotational speed of the sample was changed from 5 rpm to 10

(a) (b)

Figure 4.1: (a) Sample obtained by applying the initial deposition parameters listed in table 4.1 and (b) sample obtained by the optimised deposition parameters optimised for the Polyteknik cluster tool (table 4.1).

rpm. Multiple samples with different layer thicknesses (150, 200 and 250 nm) were fabricated. Unfortunately, no significant change in uniformity was observed for any layer thicknesses. Secondly, substrate temperature during deposition was varied. Samples with substrate temperatures ranging from 150 to 300 °C were manufactured. Layers of 150, 200 and 250 nm were deposited once again. By visual inspection, it was found that the majority of the samples, deposited with a substrate temperature of 300 °C, showed a much more uniform texture after the wet etching step. The best results (in terms of uniformity) were obtained for an ITO thickness of 200 nm. One of the samples that was obtained by applying the optimised deposition parameters listed in table 4.1, is shown in figure 4.1b. Although it is important to have a reproducible and uniformly textured substrate, a morphological analysis and optical characterisation are required to decide which deposition parameters lead to a substrate that contains the desired properties for the fabrication of an MST.

Table 4.1: Optimised deposition parameters, reported by Psomadaki [79], and deposition parameters used in this work for the first textured glass samples.

Deposition Parameter	**Reference [79]**	**Initial**	**Optimised**
Power	300 W	200 W	200 W
Substrate temperature	100 °C	150 °C	300 °C
Pressure	10 µbar	10 µbar	10 µbar
Layer thickness	200 nm	200 nm	200 nm

4.1.2. Morphological Analysis

Textured glass substrates were subjected to an AFM scan to study surface morphology. After covering textured glass substrates with 20 nm of silver (Ag), to avoid a charge build-up on the surface, AFM scans were made. The surface of a randomly textured glass substrate (optimised deposition parameters from table 4.1) showed a structure consisting of various craters. Similar results were obtained by Psomadaki [79] after optimising the deposition parameters for the Kurt. J. Lesker sputter tool. Craters varied in diameter from 0.5 to 9 µm, with an average crater diameter of approximately 2.3 µm. The depth of the craters varied from several 100 nm for small craters, to approximately 1.7 µm for the largest craters.

Craters were individually marked and two statistical parameters (depth and equivalent diameter)

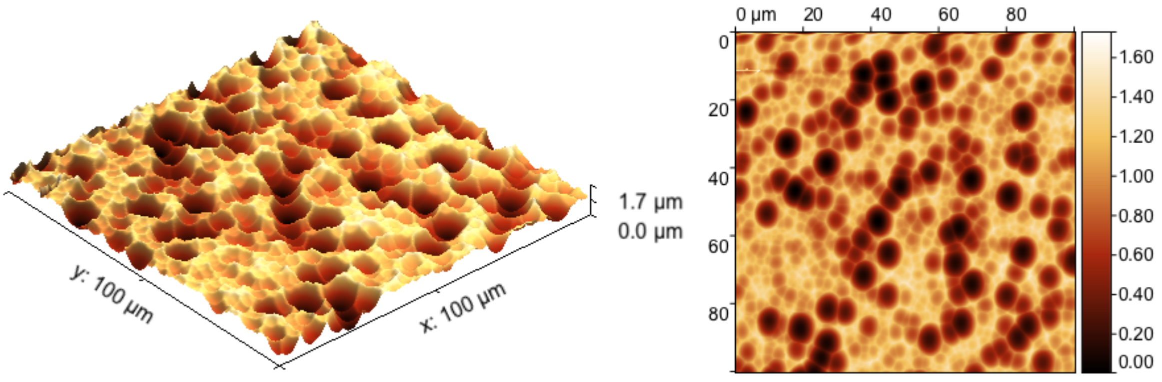

(a) **(b)**

Figure 4.2: (a) Orthogonal projection corresponding to (b) a 100x100 µm AFM image of a textured glass substrate, obtained after sputtering 200 nm ITO and 30 minutes etching.

were retrieved, using Gwyddion software [66]. Assuming that the shape of crater boundaries could be approximated by a circle, the distribution of equivalent crater diameters is shown in figure 4.3a. This distribution indicates that more than half of the craters on the 100x100 µm AFM scan has an equivalent diameter of less than 2 µm. The average crater depth on the scanned surface is 0.7 µm. The distribution of the crater depth is shown in figure 4.3b.

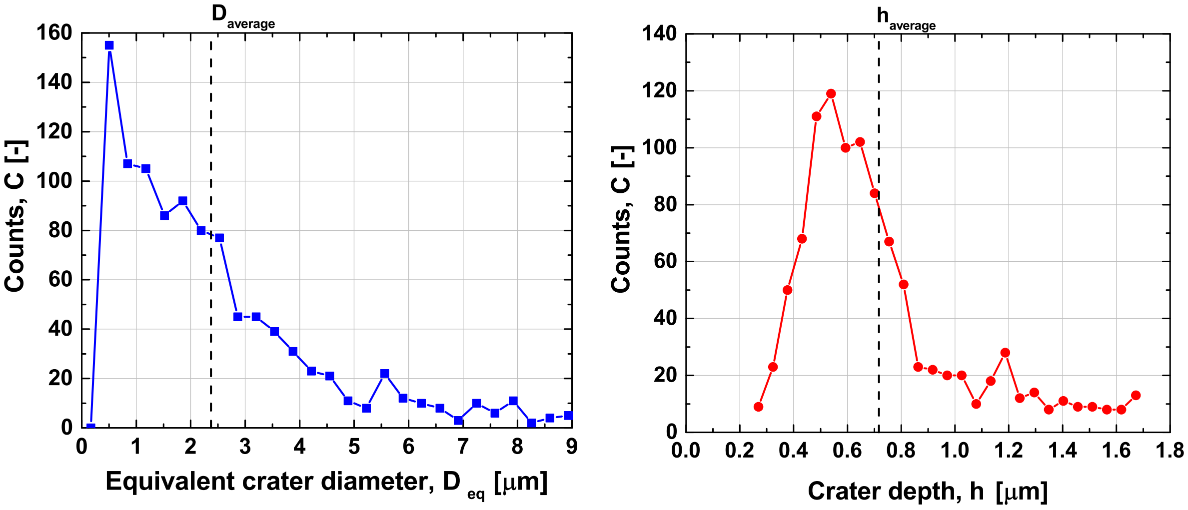

(a) **(b)**

Figure 4.3: (a) Distributions of equivalent crater diameter D_{eq} and (b) crater depth h. Dashed vertical lines indicate weighted average values for both parameters.

A textured surface can be characterised by its root mean square roughness (σ_{RMS}). This parameter gives an indication of the vertical deviation of surface features from their average value. Equation 4.1 gives the definition of this parameter [7],

$$\sigma_{RMS} = \sqrt{\frac{1}{N} \cdot \sum_{i=1}^{n} (z_i - \hat{z})^2} \tag{4.1}$$

where N is the number of points, z_i is the height of the i_{th} measurement point, and $\hat{z}$ is the average surface height. Since the deposition of ITO and the resulting texture are not perfectly uniform, five different areas of one sample were scanned.

To determine the minimum distance between these five areas, the correlation length L_C of the full 100x100µm^2 surface was calculated. Correlation represents the average lateral component of features at the surface [7]. To determine the correlation length, an autocorrelation function (ACF) was extracted from the AFM image. Cutting the peak of this ACF at $1/e$ of its maximum, results in a disk with a diameter equal to the correlation length L_C [7]. The value of the correlation length that was obtained for this sample was equal to 4.07 µm.

Five 20x20 µm^2 areas, separated by $5 \cdot L_C$, were scanned individually. The surface roughness of the AFM scan presented in figure 4.3 was averaged over these five scans and was equal to $\sigma_{RMS} = 352.6 \pm 39.1$ nm. To have more insight in how the depth of craters relates to their size, an analysis based on the distributions of the equivalent crater diameter and depth (figures 4.3a and 4.3b) was carried out. The aspect ratio (AR) of craters was calculated using equation 4.2. The aspect ratio of the randomly textured sample was equal to 0.12 ± 0.017. Surface parameters of the randomly textured sample are summarised in table 4.2.

$$AR = \frac{\sigma_{RMS}}{L_C} \tag{4.2}$$

Table 4.2: Summary of surface parameters that were presented in this section.

Parameter	Symbol	Value
Weighted average equivalent crater diameter	$\mathrm{D_{eq}}$	2.37 µm
Weighted average crater depth	h	0.717 µm
Root mean square roughness	σ_{RMS}	352.6 ± 39.1 nm
Aspect ratio	AR	0.12 ± 0.017
Correlation length	$\mathrm{L_C}$	4.07 µm

4.1.3. Optical Characterisation

The optical behaviour of textured glass samples was evaluated using spectrophotometry. Because properties of textures are directly related to the conditions under which the ITO layers were deposited, various samples were studied. The crystallinity of ITO layers depends both on temperature and layer thickness [80]. This crystallinity has a strong influence on the size and shape of features that result from the etching process [79]. A different feature size or shape could result in different optical behaviour. Therefore, samples were covered with 150, 200 and 250 nm ITO with a rotational speed of 5 and 10 rpm. After 30 minutes of etching, samples were dried and visually inspected. Substrates that were covered with a 250 nm layer contained some ITO traces after etching. Therefore, these two substrates were subjected to a further etching step of 20 minutes. After all samples were rinsed, cleaned in an ultrasonic bath, and dried, transmittance (total & diffuse) was measured. Haze $H_T(\lambda)$ of these samples was calculated using equation 4.3. The result is shown in figure 4.4.

$$H_T(\lambda) = \frac{T_D(\lambda)}{T_T(\lambda)} \tag{4.3}$$

From this graph it is obvious that substrates covered with 250 nm ITO do not perform well in terms of light scattering. Even after 50 minutes of wet etching, only a very light texture on the glass substrate was obtained. Figure 4.4 shows that a glass substrate with 250 nm ITO, deposited at 5 rpm, transmits more than 50% of the incident light without scattering. This sample, and the sample with 250 nm ITO deposited at 10 rpm, are therefore not useful for light trapping purposes. These results are in accordance with the findings of Psomadaki [79].

Textures obtained by sputtering 150 and 200 nm ITO layers show enhanced light scattering over the full spectrum. Although samples based on a 150 nm ITO layer show a more constant haze in

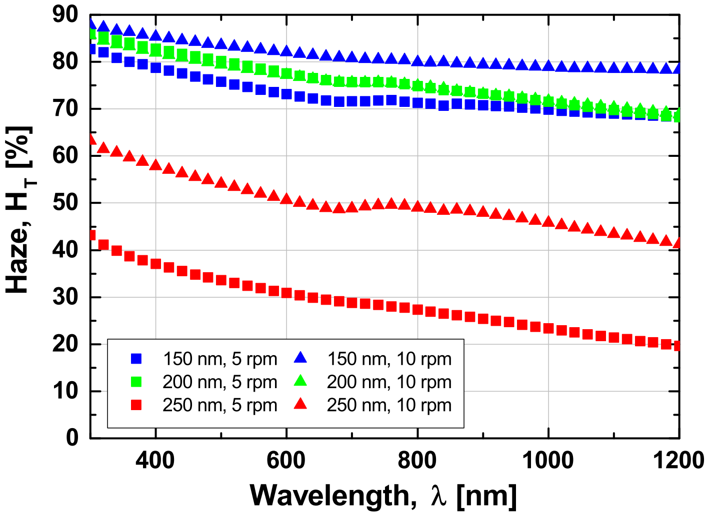

Figure 4.4: Haze $H_T(\lambda)$ of six randomly textured Corning glass substrates.

the long wavelength range (> 800 nm), samples obtained by etching 200 nm ITO layers were more reproducible, both in texture uniformity and haze. Therefore, a decision was made to use the optimised deposition parameters, listed in table 4.1, to fabricate the randomly textured substrates for further research.

The haze graph of figure 4.4 is based on the ratio between diffuse and total transmission. This ratio depends on the size of the opening through which the specular component leaves the integrating sphere. To investigate the direction in which the incident light is scattered, the angular intensity distribution was measured in transmission mode ($\mathrm{AID_T}$). The $\mathrm{AID_T}$ obtained for a randomly textured glass substrate is shown in figures 4.5a and 4.5b. Note that the small peaks for wavelengths longer than 860 nm (detector switching point, subsection 3.2.2) are most probably caused by noise in the lead sulfide (PbS) detector.

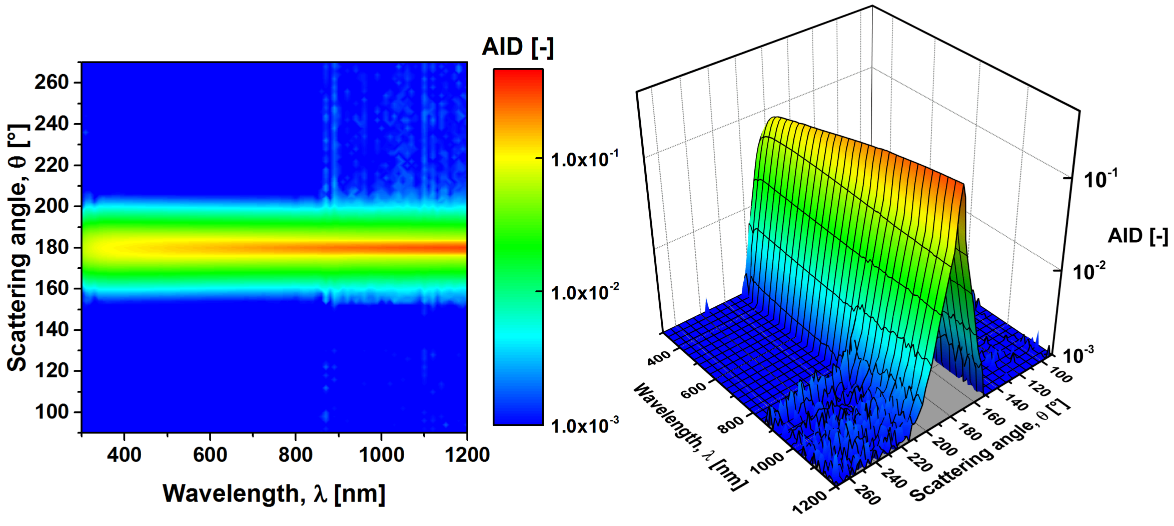

(a) (b)

Figure 4.5: (a) $\mathrm{AID_T}$ plot of a randomly textured substrate and (b) a 3D projection. The colours in the 3D plot correspond to the levels of the colour bar in the 2D $\mathrm{AID_T}$ image.

During measurements that lead to these AID_T plots, the sample was positioned at 90° with respect to the incident light beam. The measurement light beam entered the ARTA drum (figure 3.7b) at an angle of 0° by definition. The angle at which scattered light reaches the detector on the other side of the sample, was defined as the scattering angle ($90° \leq \theta \leq 270°$). The angular intensity distribution plots show that scattering of incident light occurs for a broad wavelength range. Light scattering is almost uniform throughout the 300-1200 nm range. The scattering mechanism that could explain this behaviour is a solution of the Maxwell equations that was found by Mie [81]. Mie scattering occurs when the geometrical dimensions of the features are larger than the wavelength of incident light. Mie scattering is weakly wavelength-dependent and has a strong directional behaviour [7]. This is clearly visible in figure 4.5a, where most of the light is scattered within a 40° cone, leading to scattering angles between 160° and 200°.

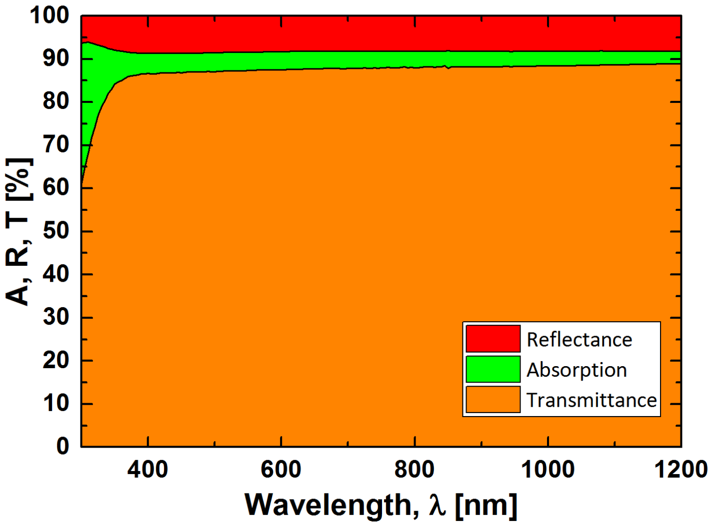

Figure 4.6: Reflectance, absorption and transmittance of a textured glass sample.

The direct component ($\theta \approx 180°$) of the transmitted light seems to have a lower intensity for short wavelengths. Because the results were obtained by measurements in transmission mode, this could have been caused by absorption of near-ultraviolet (UV) light in the glass. The result of a total transmittance-reflectance measurement (figure 4.6) shows that for wavelengths shorter than 400 nm, absorption in the substrate significantly increases. If this surface morphology would be used as a substrate in an *n-i-p* solar cell, absorption in glass would not affect the device performance, since a back reflector would be present, and all near-UV light would be absorbed in the front TCO layer or top-part of the solar cell.

4.2. Periodic Gratings

As explained in section 2.4, the application of wavelength-scale periodic gratings is an attractive alternative to random textures. Periodic gratings allow high intensity scattering of light in pre-selected angles. Random textures scatter the majority of incident light in a narrow cone around the direct component (figure 4.5a) and only very few incident light is scattered to larger angles. Periodic gratings, however, allow scattering to wide, distinct angles, while keeping a relatively high intensity. Gratings were fabricated using a photolithography process. As explained in subsection 3.1.5, a mask was required for this process.

4.2.1. Photolithography Masks

Yu *et al.* [49] used the Temporal Coupled Mode (TCM) theory, that was discussed in section 2.4.1, to calculate the absorption limit of grating structures, making use of simulations. Results showed that the value of the absorption enhancement factor (F) depends on the ratio between grating period (L) and wavelength. The maximum absorption enhancement factor for two-dimensional (2D) square and hexagonal gratings is reached for L/λ close to 1, as shown in figure 2.12. For one-dimensional (1D) gratings, maximum absorption enhancement is reached for all integer multiples of L/λ. Section 2.2 explained that the absorption coefficient of nc-Si:H for long wavelengths is relatively low. As this thesis focuses on substrates for nc-Si:H solar cells, periodic gratings will only affect long wavelength light that has not been absorbed after a single pass. Therefore, the decision was made to focus on wavelengths around 1000 nm when designing photolithography masks. To reach the maximum enhancement factor, gratings with a period of 1000 nm should be fabricated. If a grating with a duty cycle of 0.5 would be considered, the feature dimension should be 500 nm. However, since the UV photolithography process using the contact aligner in the EKL facility did not allow sub-micron features, the decision was made to focus on an L/λ ratio around 2. For the wavelength of interest ($\lambda = 1000$ nm), grating periods around 2000 nm result in the desired L/λ ratio.

Two photolithography masks, each containing four quadrants, were designed using Tanner L-edit IC-Layout software [82]. The first mask was used to fabricate 1D gratings with a different period in each quadrant: 1800, 2000, 2200 and 2400 nm. The duty cycle of all 1D gratings was fixed at 0.5. For the 2D grating mask, 1x1 μm^2 square features were used. This mask consisted of two quadrants with square, and two quadrants with hexagonal 2D gratings ($L = 2000$ and $L = 2400$ nm). The duty cycle of the square lattice gratings was equal to 0.25. The geometry of the hexagonal lattice gratings resulted in a duty cycle of 0.21. Photographs of the photolithography masks are shown in figures 4.7a, 4.7b and 4.7c. The reflection of white light, incident on the masks during the capture, clearly shows the different diffraction patterns for three different grating configuration.

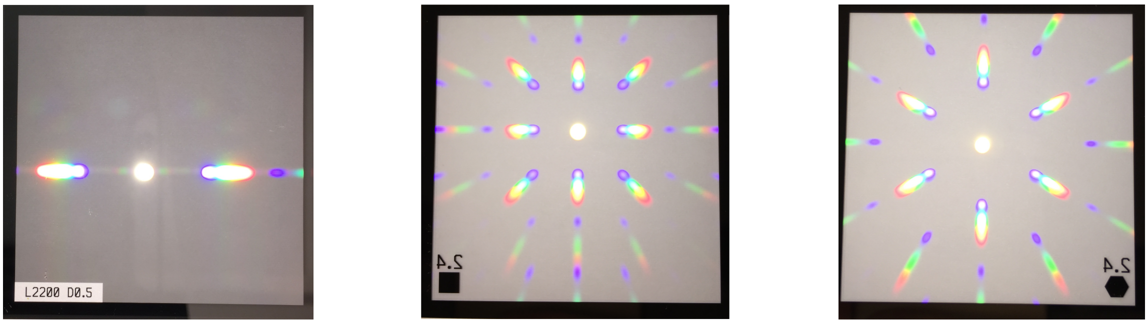

(a) (b) (c)

Figure 4.7: Photographs of three quadrants of the photolithography masks: (a) 1D grating ($L = 2400$ nm, $D = 0.5$), (b) 2D square lattice grating ($L = 2400$ nm, $D = 0.25$) and (c) 2D hexagonal lattice grating ($L = 2400$ nm, $D = 0.21$).

4.2.2. Morphological Analysis

In order to study the surface morphology of periodic gratings after the lithography process, surfaces were scanned using the AFM technique. To investigate the effect of the development time on the size and shape of 1D gratings, various samples were analysed. Development times between 30 and 120 s were evaluated in steps of 15 s. AFM scans of three different samples obtained from this series are presented on page 49. Figures 4.9a to 4.9f show the surface morphologies that resulted from development steps of 30, 75 and 120 s, respectively. Interesting parameters to evaluate are average peak to valley height and shape of the features that were reproduced by the photolithography process. The average peak to valley height of the samples was expressed as R_{3z}: *Average third highest peak to third lowest valley height.* This parameter was calculated over the entire AFM scan for all samples.

The mask that was used for all 1D gratings should result in rectangular features. However, the sample that was developed for 30 s resulted in a surface that consisted of relatively wide features with narrow valleys in between. It is clear that the MF322 developer did not have enough time to remove all photoresist between the unexposed features. The value of R_{3z} for this sample is equal to 671 nm. Developing for 75 s lead to more rectangular structures and a higher peak to valley height (R_{3z} = 833 nm). A small, but quite narrow valley on the left side of the features appears in figure 4.9d. This behaviour became more dominant up to a development time of 105 s. For a development time of 60 s, the area between the features was more flat and did not show this valley. A development time of 120 s resulted in a surface containing waves instead of rectangular features. As development time passed, the developer might have affected the unexposed photoresist, resulting in features with less steep sidewalls. Table 4.3 presents the R_{3z} values for all samples that were analysed. These values were obtained from glass samples that were prepared under the same conditions. After photoresist exposure, the 10x10 cm^2 samples were cut in four equal pieces and subjected to different development times.

Table 4.3: Average third highest peak to third lowest valley height (R_{3z}) for different development times.

Development time [s]	**R_{3z} [nm]**	**Development time [s]**	**R_{3z} [nm]**
30	671	90	1017
45	771	105	932
60	710	120	630
75	883		

Up to a development time of 90 s, the peak to valley height seems to follow an increasing trend. More than 90 s development leads to a decrease in peak to valley height. Features with a large R_{3z} were preferred to ensure the preservation of grating features after metal deposition or combination with random textures. Besides that, relative smooth surfaces are preferred for defect free growth of nc-Si:H layers. Based on these two requirements, a development time of 70 s was chosen to have a relative high R_{3z} value and avoid the appearance of narrow valleys between features.

An aluminium layer of 750 nm was evaporated on top of the 1D grating to evaluate the effect of the metal layer on the shape of the features. Figure 4.8 shows the average height profile of a 10 μm 1D periodic grating section (L = 2000 nm) after 750 nm aluminium evaporation (averaged over a width of 15 μm). The distance between two consecutive features has become narrower, but features were well maintained and did not transform into a wave-like structure.

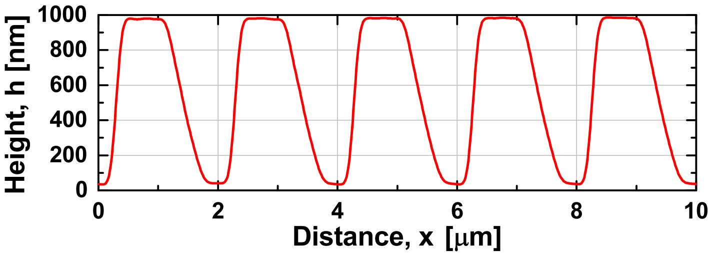

Figure 4.8: Average profile height of a 10 μm section of a 1D periodic grating (L = 2000 nm, D = 0.5), averaged over a width of 15 μm.

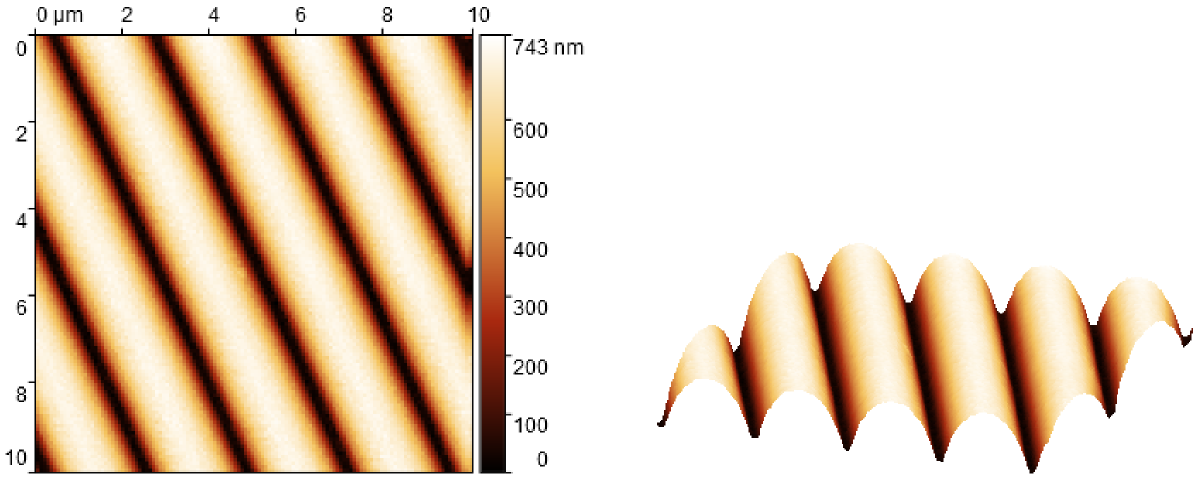

(a) 2D AFM image: 30 s development time

(b) 3D projection of figure 4.9a

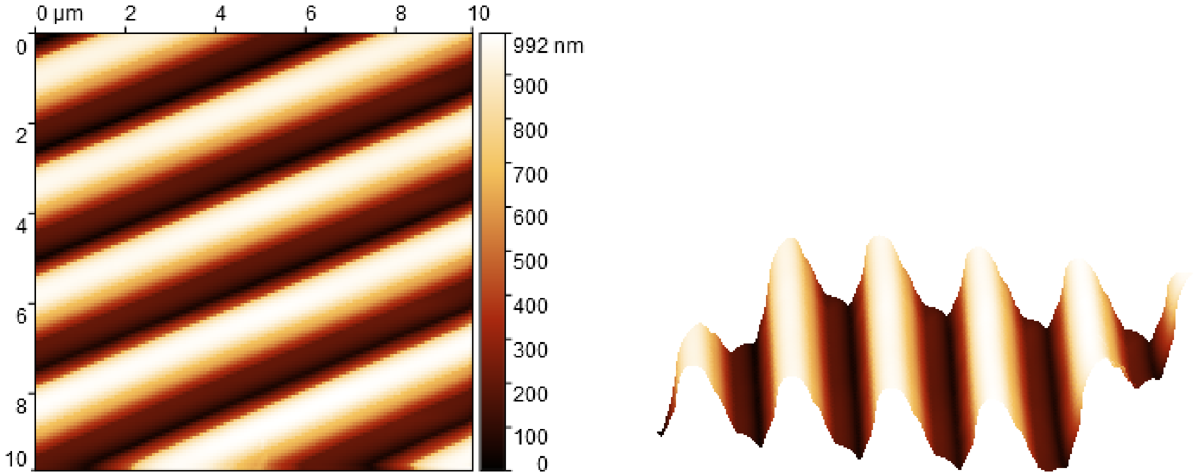

(c) 2D AFM image: 75 s development time

(d) 3D projection of figure 4.9c

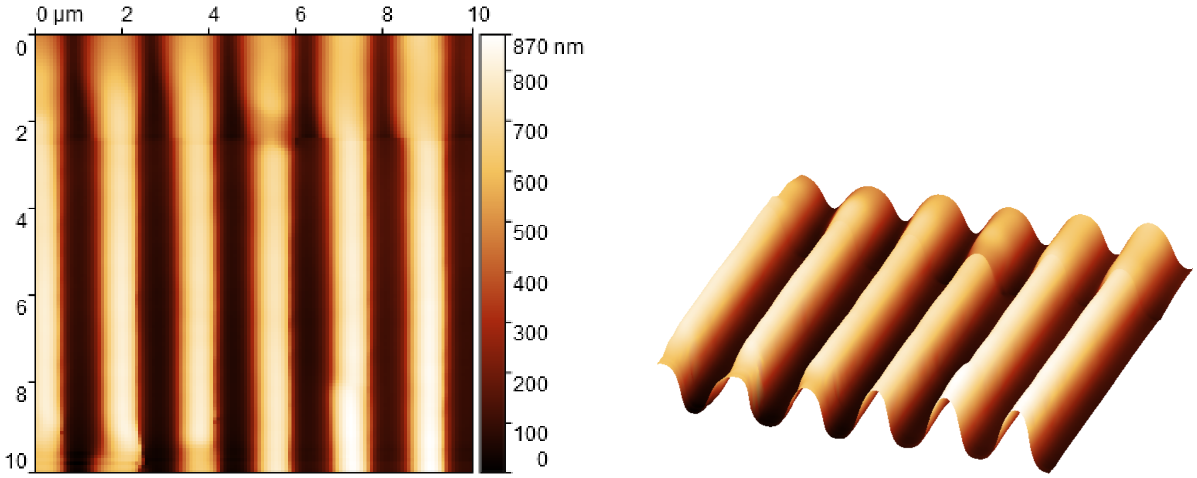

(e) 2D AFM image: 120 s development time

(f) 3D projection of figure 4.9e

Figure 4.9: AFM images for three different development times: 120 s ($R_{3z} = 630$ nm), 75 s ($R_{3z} = 883$ nm) and 30 s ($R_{3z} = 671$ nm). The colours in each 3D projection are in accordance with the colour scale bar in the corresponding 2D image.

After the optimisation of 1D periodic gratings, the same process was used to develop 2D gratings. After spin coating photoresist with higher rotational speeds (up to 2750 rpm) and evaporating 500 nm aluminium, the 2D periodic grating of figure 4.10 was obtained. This grating had a relatively high aspect ratio of 0.64 ± 0.02. Faster rotation during the spin coating process did not yield a lower aspect ratio. The AFM image of figure 4.10 shows that the hexagonal pattern is reproduced, while some small defects are present on the surface. The lines on the picture are artefacts of the AFM scan and not part of the surface morphology.

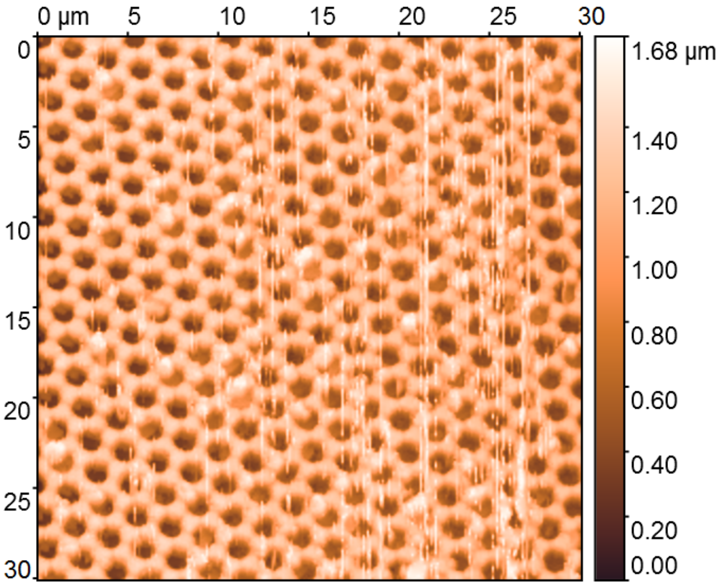

Figure 4.10: AFM image of 2D hexagonal grating with a period of $L = 2000$ nm.

4.2.3. Optical Characterisation

Similar to the optical characterisation of random textures (subsection 4.1.3), the optical behaviour of substrates based on periodic gratings was evaluated using spectrophotometry. The measurements were carried out using 1D gratings in photoresist on glass, measured in air ($n_{air} \approx 1$), in the wavelength range of interest: 300-1200 nm. The measurement light beam was incident on the glass substrate, continuing to the glass-photoresist interface, and leaving the sample from the patterned photoresist-air interface. Grating samples were vertically mounted in the ARTA accessory (subsection 3.2.2), such that the diffraction pattern was distributed within the plane of rotation of the small, rotating integrating sphere (IS). The full wavelength range was measured for every 2°, along a semicircle from 90° to 270° with respect to the incident light beam.

From a theoretical point of view, a diffraction pattern can be predicted using the grating equation (equation 2.16) that was introduced in section 2.4. Another expression of this equation can be obtained to find the scattering angle θ [7].

$$\theta = \sin^{-1}\left[\frac{m \cdot \lambda}{n_2 \cdot L} + \frac{n_1}{n_2} \cdot \sin\theta_{inc}\right] \tag{4.4}$$

This equation includes the refractive indices n_1 and n_2 for the incident and diffractive media, respectively. Because measurements were taken in air, these refractive indices were equal to 1. θ_{inc} represents the incident angle of the measurement beam. As explained in subsection 3.2.2, this angle was defined as 0°. Including these values in equation 4.4 results in a simplified expression for the scattering angle, presented in equation 4.5.

$$\theta = \sin^{-1}\frac{m\cdot\lambda}{L} \tag{4.5}$$

The expression for the scattering angle now only depends on the diffraction mode m, the wavelength λ, and the grating period L. Scattering angles of multiple symmetrical diffraction orders were calculated for every wavelength from 300 to 1200 nm, for the fabricated grating periods. $\mathrm{AID_T}$ measurements were taken for gratings with periods of 1800, 2000, 2200 and 2400 nm. Figures 4.11 and 4.12 show the $\mathrm{AID_T}$ graphs including the diffraction modes (dashed lines), calculated using the grating equation. $\mathrm{AID_T}$ values lower than $1\cdot10^{-3}$ were filtered out to reduce measurement noise and make the graphs more clear.

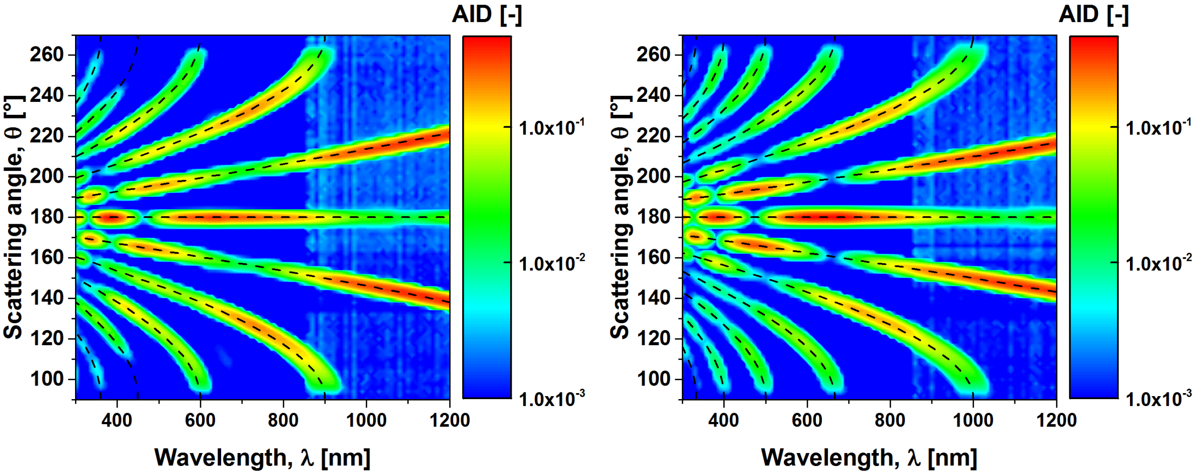

(a) (b)

Figure 4.11: $\mathrm{AID_T}$ plots of periodic gratings in photoresist on flat glass, with periods equal to (a) $L = 1800$ nm and (b) $L = 2000$ nm.

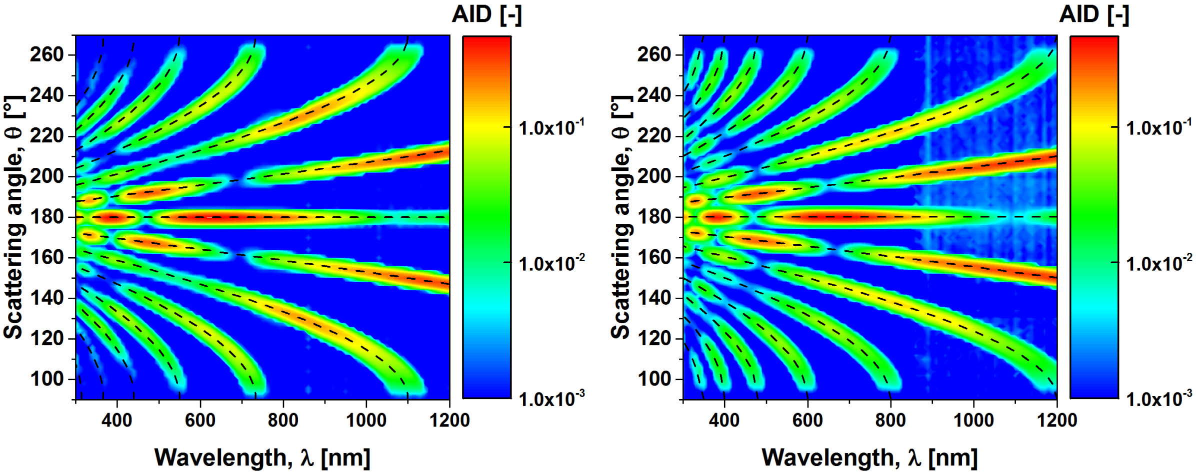

(a) (b)

Figure 4.12: $\mathrm{AID_T}$ plots of periodic gratings in photoresist on flat glass, with periods equal to (a) $L = 2200$ nm and (b) $L = 2400$ nm.

The AID_T graphs show that measured scattering angles match the values that were calculated using equation 4.5. This is an indication that the periodicity of the gratings in photoresist is well reproduced. All AID_T plots show that wide angle scattering up to almost 90° can be achieved when using periodic gratings. Where random textures only reach AID_T values of $1 \cdot 10^{-2}$ for angles relatively close to 180° (figure 4.5a), periodic gratings allow high intensity scattering for distinct, much wider angles. Furthermore, these results show that the intensity distribution can be adjusted by carefully tuning the grating period. Increasing the period of the grating leads to an increase in the number of excited diffraction modes in the same wavelength range. 3D projections of the AID_T graphs that were presented in figures 4.11 and 4.12 can be found in appendix A.

Although equation 4.5 is correct for the measurement results that were presented, extra care should be taken when applying periodic gratings in solar cells. The refractive index of absorber materials is not equal to 1, but can differ significantly. For instance, the refractive index of nc-Si:H reaches values between 3.56 to 5.04 in a wavelength range from 300 to 1200 nm [24]. When equation 4.4 is used to take the refractive indices of the incident and diffractive media into account, diffraction modes will shift. Figure 4.13 shows the effect of substituting air with nc-Si:H (refractive index n_2 [24]) as diffractive medium. This figure is based on a grating with a period $L = 2000$ nm. To clearly indicate the difference, this graph only shows the 0^{th}, 1^{st} and 2^{nd} order diffraction modes. The increase in refractive index causes diffraction modes to shift towards a scattering angle of 180°. Due to this behaviour, extra diffraction modes can be excited in the same wavelength range. To summarise, both grating period and refractive index influence the angular intensity distribution of grating structures. Changing the grating period allows tuning of the intensity distribution.

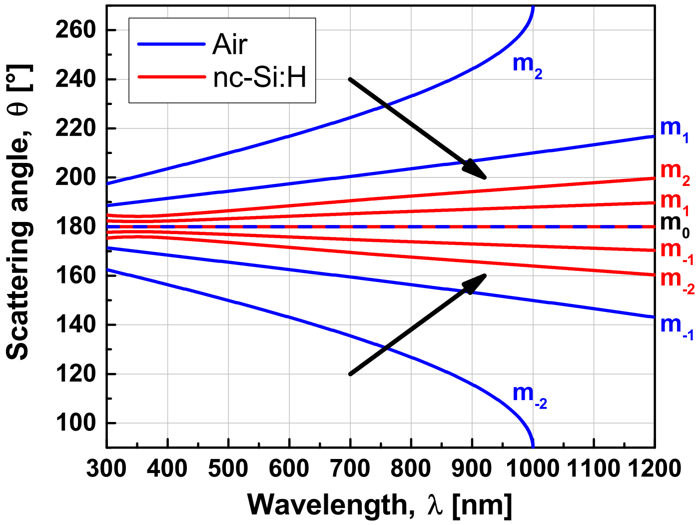

Figure 4.13: Calculated scattering angles in two diffractive media: air and nc-Si:H. Based on a grating with period $L = 2000$ nm and $\theta_{inc} = 0°$.

4.3. Random-Periodic Modulated Surface Textures

Subsection 2.4.2 introduced modulated surface textures as promising alternatives to random textures or periodic gratings. By combining surface morphologies with different dimensions, high intensity light scattering could be achieved over a broad wavelength range. This section presents the results of combining the random textures, obtained in section 4.1, with periodic gratings from section 4.2. Similar to the previous section, results of morphological analysis and optical characterisation will be discussed. This section mainly focuses on MST structures based on 1D gratings.

4.3.1. Morphological Analysis

Uniform, randomly textured samples that were fabricated using the optimised deposition parameters from subsection 4.1.1, were used as basis for modulated surface textures. To ensure that all craters were filled, samples were entirely covered with photoresist and spin coated at low rotational speeds (1000-1500 rpm). It was assumed that photoresist would not be removed from the craters at low spin speeds. After hard baking of the photoresist, samples were covered with 20 nm Ag. The surface morphology of a first successful process is shown in figure 4.14.

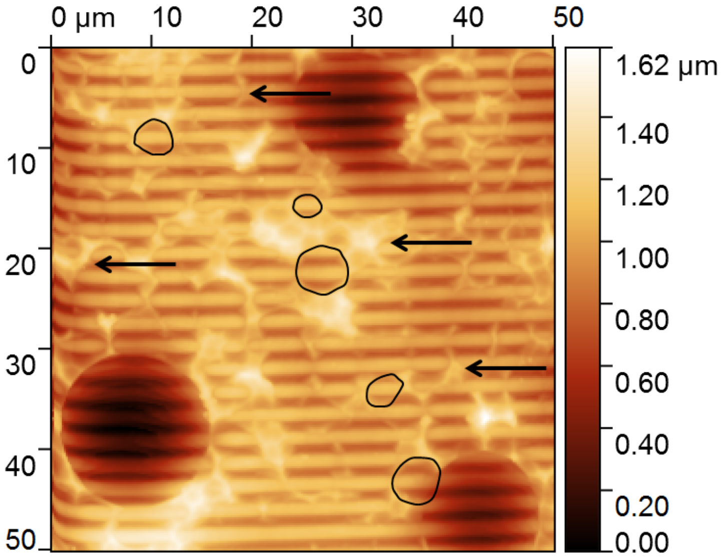

Figure 4.14: 50x50 µm^2 AFM image of the first result for a 1D periodic/random modulated surface texture. Black arrows indicate several shapes, different from craters and grating features. Black lines indicate possible locations of craters that were flattened out by a thick photoresist layer.

This sample was considered as a successful first try, because 1D gratings are clearly visible in three large craters present on the surface. At these locations, both surface morphologies are combined to form a 1D periodic/random modulated surface texture. However, when this 50x50 µm^2 surface is compared to a 50x50 µm^2 area of the randomly textured surface in figure 4.2b, it is clear that many craters of the random texture disappeared. The surface roughness of $\sigma_{RMS} = 221.8 \pm 80.6$ nm indicates that the surface is relatively flat compared to a randomly textured surface ($\sigma_{RMS} = 352.6 \pm 39.1$ nm). Most probably, the low rotational speed during the spin coating process resulted in a thick photoresist layer that flattened small craters. As explained in subsection 2.4.2, the morphological surface characteristics of different layers are only preserved if subsequent layers are thin enough. Besides the three craters and 1D periodic grating that are clearly visible in figure 4.14, the surface contains different features, of which a few are indicated by black arrows in the figure. Most probably, these features arise at the crater edges, caused by an accumulation of photoresist on the surface. Black circles in figure 4.14 indicate several possible locations of craters that have been flattened out by the photoresist. Many more of these possible crater locations can be found on the surface.

To investigate whether a thinner photoresist layer could preserve more of the craters, the rotational speed of the spin coating step was increased to 2250 rpm. This rotational speed was used for the fabrication of 1D periodic gratings on flat glass, which resulted in a 1200 nm photoresist layer. Besides the rotational speed for spin coating, the exact same process steps that were used for the fabrication of the first sample in figure 4.14 were used to obtain a second MST structure. Figures 4.15a and 4.15b present the 100x100 µm^2 AFM scans that were obtained.

These AFM scans show that this sample incorporates many of the craters of the random texture. The surface roughness of $\sigma_{RMS} = 304.9 \pm 31.3$ nm indicates that the surface contains more of the

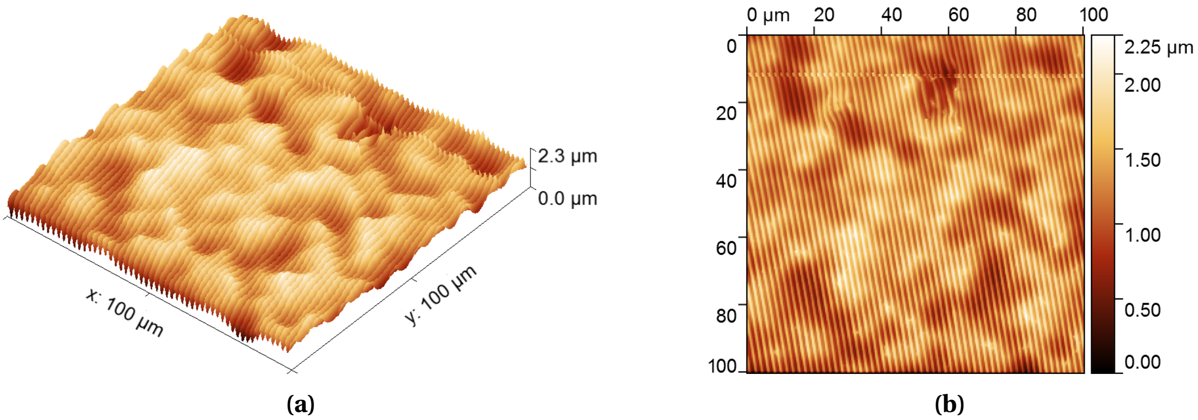

(a) (b)

Figure 4.15: (a) Orthogonal projection corresponding to (b) a 100x100 µm 2D AFM image of a 1D periodic ($L = 1800$ nm)/random modulated surface texture.

original surface morphology than the sample in figure 4.14. Considering that this sample preserves both the surface morphology of random texture and periodic grating, it can be concluded that a modulated surface texture based on large random features, superimposed by smaller periodic gratings can be manufactured.

Using the same process, 2D gratings with both square and hexagonal lattice structures have been fabricated. These substrates will be further discussed in section 4.4 and chapter 5.

4.3.2. Optical Characterisation

To evaluate the optical behaviour of samples with an MST structure, spectrophotometry was used. Similar to the samples based on 1D periodic gratings, the MST samples were placed vertically inside the ARTA accessory. The morphological analysis showed that the surface of an MST is a combination of two different morphologies. Therefore, it was expected that the resulting optical behaviour would combine the individual light scattering properties of both samples. Bringing the results from subsections 4.1.3 and 4.2.3 together should give broadband light scattering, combined with distinct diffraction modes as an outcome.

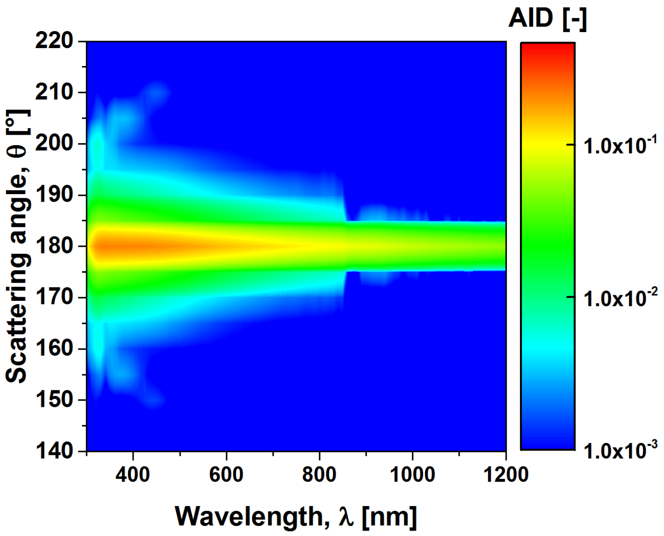

Figure 4.16: $\mathrm{AID_T}$ plot of the first MST sample corresponding to figure 4.14.

Initially, the sample that was discussed in subsection 4.3.1 was optically characterised. A measurement in the wavelength range of 300-1200 nm was obtained for every 10 nm for angles ranging from 140°-220°, every 5°. Figure 4.16 shows the angular intensity distribution plot that resulted from these measurements. This figure clearly contains the specular component and narrow angle light scattering around 180°. Additionally, two very weak diffraction modes seem to arise for $\lambda = 300$ nm around scattering angles of 160° and 200°. These diffraction modes are in accordance with the grating equation for a grating with period $L = 1800$ nm. However, more distinct and more intense diffraction modes were expected. Possibly, the accumulated features at the crater edges on this sample have suppressed the diffraction effect of the periodic grating. Therefore, another sample obtained after application of a thinner photoresist layer was optically characterised.

Figure 4.17a presents the AID$_\text{T}$ measurement of a modulated surface texture that was obtained by superimposing a 1D grating ($L = 2000$ nm) on a randomly textured substrate. Measurements were taken every 2° along a semicircle ranging from 90° to 270°, every 10 nm in the range of 300-1200 nm. Contrary to figure 4.16, this angle intensity distribution plot follows the expectations. Distinct diffraction modes and broadband scattering around these modes indicate that both scattering mechanisms contribute to the optical behaviour of this substrate. The difference between the AID$_\text{T}$ plot of the MST and the AID$_\text{T}$ for a grating on flat glass is clear. The intensity of the diffraction modes is lower in figure 4.17a compared to figure 4.17b. On the other hand, in figure 4.17b almost no light intensity was measured between the diffraction modes. The MST structure clearly scatters light to angles that were not described by the grating equation. This shows that periodic-random modulated surface textures can achieve light scattering into greater, less distinct angles, when compared to either one of the individual structures. The 3D projection of figure 4.17a can be found in appendix A.

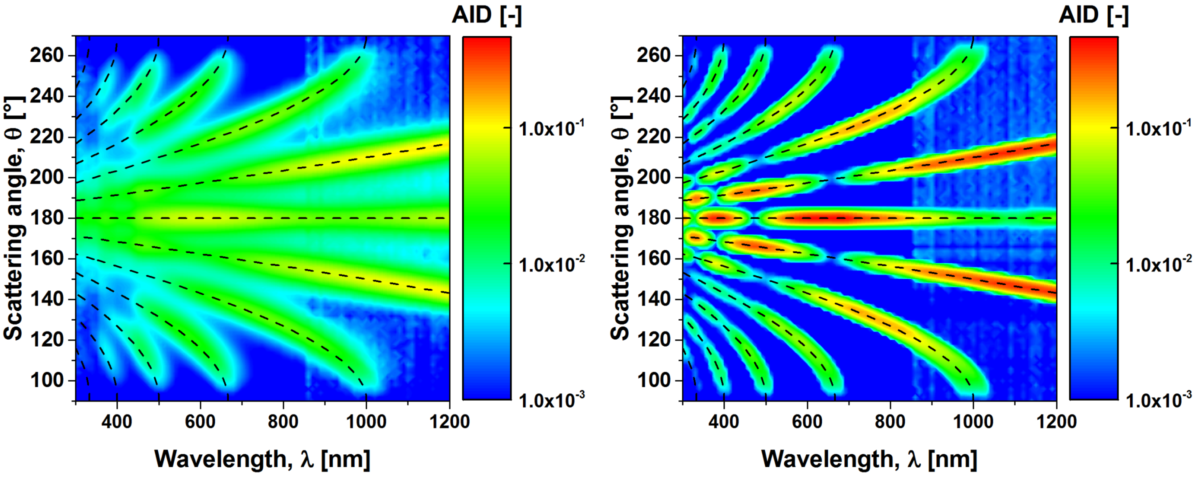

(a) (b)

Figure 4.17: (a) AID$_\text{T}$ plot of a periodic ($L = 2000$ nm)-random modulated surface texture. (b) AID$_\text{T}$ of a periodic grating on flat glass ($L = 2000$ nm). Black dotted lines indicate the diffraction modes, calculated by the grating equation.

4.4. Influence of Back Reflector Structure on Absorption

In the previous three sections, various substrates were evaluated in terms of surface morphology and light scattering behaviour. To evaluate their effect on light absorption, these substrates were used as back reflectors in an additional analysis. During this experiment, three different back reflectors were used: flat glass, textured glass, and modulated surface textures based on 2D periodic gratings and textured glass. Periodic gratings on flat glass were manufactured, but not evaluated because nc-Si:H layers were peeling off from the substrate. The following deposition sequence was applied on top of the substrates: 300 nm Ag / 100 nm a-SiO_x:H / 1500 nm nc-Si:H. Figure 4.18 shows a schematic overview of the structures that were evaluated.

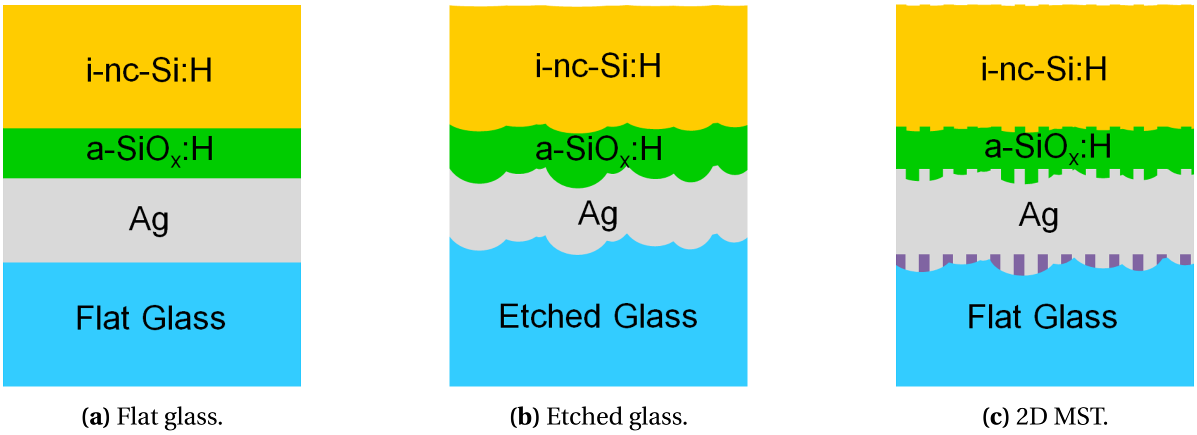

(a) Flat glass. **(b)** Etched glass. **(c)** 2D MST.

Figure 4.18: Structures that were used to evaluate the effect of the back reflector on absorption in a stack of Ag / a-SiO_x:H / i-nc-Si:H.

The main objective of this experiment was to make a qualitative comparison between light absorption in structures with different back reflector surface morphologies, rather than obtaining quantitative data regarding the absorption enhancement factor. The reflectance of different samples was obtained using spectrophotometry. The assumption was made that a 300 nm Ag layer would act as a perfect back reflector (i.e. $R = 100\ \%$, $T = 0\ \%$). With this assumption, light absorption in the stack could be easily calculated ($A = 1 - R$).

It is known that textured interfaces can excite so-called *surface plasmon polaritons* (SPPs). SPPs are electromagnetic waves that travel along the interface of a metal with a dielectric material [83]. These SPPs cause parasitic absorption in the metal and therefore contribute to reflection losses of metal back reflectors. However, parasitic absorption can be reduced by introducing a dielectric, low refractive index buffer layer between the metal and absorber layer [84]. To reduce the effect of parasitic absorption in the metal as much as possible, a 100 nm *n*-type SiO_x:H layer was deposited on the back reflector. Finally, a 1500 nm i-nc-Si:H layer was used as absorber material.

Calculated absorption results for different structures were averaged over at least three samples for each structure. These samples were manufactured by various depositions, to suppress possible process parameter deviations during single depositions. Figure 4.19 presents the results for three different structures. For MST stacks, the highest overall absorption was obtained for a 3 µm square lattice periodic grating. Therefore, this result was used in figure 4.19. All results of MST structures, based on hexagonal lattice gratings and square gratings with 3 and 4 µm periods, are presented in appendix B.

The graph in figure 4.19 can be divided into three main areas. The first area ranges from 300 to 600 nm. All light that is coupled into the absorber stack is absorbed in this range. Interference effects, appearing for wavelengths larger than 600 nm in the graph of the flat glass sample, indicate that a part of the in-coupled light reaches the front interface again after two passes through the stack, and escapes. The second area ranges from 600 to 1117 nm. This is the spectral range in which in-coupled light is partially absorbed, and partially escaping after (at least) two passes through the stack. The wavelength that corresponds to the bandgap of nc-Si:H is $\lambda = 1117$ nm [24]. Therefore, the last range of this graph is $1117\,\text{nm} \leq \lambda \leq 1500\,\text{nm}$. Absorption for $\lambda > 1117$ nm can only be explained by parasitic absorption in silver, or free-carrier absorption (FCA) in the doped a-SiO_x:H

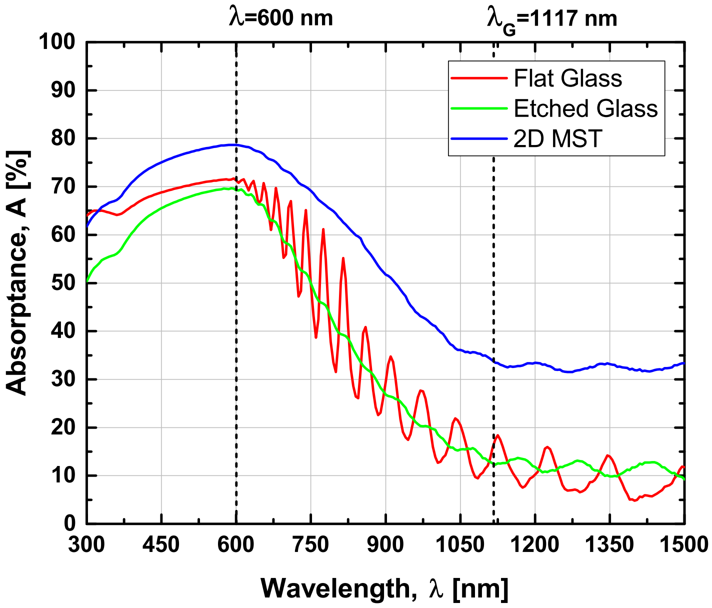

Figure 4.19: Absorptance in Ag / a-SiO_x:H / nc-Si:H structures, based on different back reflector surface morphologies.

layer [10]. However, the magnitude of free-carrier absorption is small compared to the parasitic absorption in silver. Furthermore, the FCA in all a-SiO_x:H layers should be similar, due to equal process parameters.

Interesting to see is that the absorption for long wavelengths in 2D MST structures is significantly higher compared to flat and etched glass samples. Despite a 100 nm a-SiO_x:H layer, the surface texture consisting of small grating features increases the parasitic absorption in silver. On the other hand, MST structures seem to increase absorption for wavelengths shorter than 600 nm. However, parasitic absorption in silver could also contribute to this increase for light that has not been absorbed after a single pass.

In the short wavelength range, the etched glass samples seem to perform worse than flat samples. This behaviour was unexpected, because often random textures are used to reduce front reflection. Furthermore, the etched glass sample clearly reduces the interference effects that were observed for the flat structure. In the textured structure, incident light gets scattered at both the front and back interface. Therefore, the phase shift with which light will arrive back at the front surface does not result in the interference pattern that was observed for flat samples.

4.5. Conclusions

This chapter studied the influence of random textures, periodic gratings and modulated surface texture on the propagation of light. Furthermore, this chapter aimed to fabricate an MST structure that consists of a large, random texture, superimposed by a smaller, periodic grating.

After an optimisation study of ITO deposition parameters, randomly textured glass substrates were obtained by wet etching. Samples that were obtained by 200 nm ITO sputtering and 30 min etching showed the best results in terms of uniformity and reproducibility. An optical characterisation study pointed out that broadband light scattering in a narrow cone around the specular component was induced by these samples.

One-dimensional periodic gratings were fabricated using a photolithography process. Optimisation of process parameters resulted in a development time of 70 s to maintain the intended morphology of grating features. Angular intensity distribution plots showed that high intensity light scattering can be obtained for distinct angles close to 90 °. Fabricated samples resulted in diffraction modes that were predicted by the grating equation. Increasing the period of the grating caused an increase in the number of excited diffraction modes. By carefully choosing the periodicity of gratings for solar cell structures, high intensity light scattering to large angles can lead to a significant increase in optical path length.

By combining both previously mentioned surface morphologies, this chapter aimed to manufacture a periodic/random modulated surface texture. Morphological analysis showed that these MST structures can be fabricated using a photolithography process with a randomly textured sample as substrate. By optical analysis of MST samples, it was found that the resulting angular intensity distribution is a compromise between the $\mathrm{AID_T}$ of the individual surface morphologies. Diffraction modes were still clearly visible, but broadband scattering around the modes allows light to propagate into angles that were not predicted by the grating equation. Therefore, MST structures show promising behaviour to obtain high intensity light scattering into less distinct, wide angles.

However, when two-dimensional MST structures were evaluated using a stack of 300 nm Ag, 100 nm a-$\mathrm{SiO_x}$:H and 1500 nm i-nc-Si:H, high parasitic absorption in the silver back reflector was obtained. Small features of the 2D periodic grating, causing higher surface roughness, might have severely contributed to this parasitic absorption. Furthermore, interference effects, present in flat samples, was significantly reduced when using 2D MST or etched glass substrates.

5

Nanocrystalline Silicon Solar Cells

The previous chapter discussed the morphological and optical characteristics of various substrates. This chapter presents the results of hydrogenated nanocrystalline silicon (nc-Si:H) solar cells that were manufactured on various substrates. The performance of devices on these substrates will be compared. The first section explains the structure of solar cells that were fabricated. The second section will discuss the first solar cell results on modulated surface texture (MST) substrates. The third section presents the results that were obtained by applying indium tin oxide layers with different thicknesses at the front side of solar cells. Finally, the fourth section will compare the performance of solar cells, based on different substrates. This chapter answers the third scientific question that was introduced in section 1.6.

5.1. Solar Cell Structure

As explained in subsection 1.4.1, nc-Si:H absorber layers are often used as bottom cells in multi-junction structures. Compared to a-Si:H, nc-Si:H has higher absorption coefficients for $\lambda > 700$ nm (figure 2.1). The relatively low bandgap of nc-Si:H, allowing near-infrared light absorption, and the absence of light-induced degradation (LID) effects [21], make nc-Si:H layers very suitable for applications in multi-junction structures. The first tandem cell based on a-Si:H and nc-Si:H, with an initial efficiency of 9.1 %, was demonstrated by Meier *et al.* [85] in 1994. Solar cells consisting of an a-Si:H top cell and a nc-Si:H bottom cell are also referred to as *micromorph* solar cells.

Even though the absorption coefficient of nc-Si:H absorber layers is relatively high compared to a-Si:H at long wavelengths, it could be a factor 10^4 to 10^7 lower at short wavelengths. Therefore, light management techniques applied in the long wavelength region are required to enhance absorption of low energetic light. Modulated surface textures, presented in chapter 4, were aiming at absorption enhancement for wavelengths around 1000 nm. Applying these MST structures to nc-Si:H solar cells could therefore yield more light absorption in the long wavelength range.

Section 1.6 explained that nc-Si:H solar cells with an *n-i-p* configuration are the object of study in this work. Because the substrate material for this type of solar cells is not restricted by any optical properties, grating structures do not require a transparent material and can therefore be fabricated in photoresist. The structure of *n-i-p* nc-Si:H solar cells, evaluated in this work, is schematically represented in figure 5.1a. Although this figure shows flat interfaces between layers, this solar cell structure was deposited on textured glass and MST substrates.

In section 4.4, 300 nm silver layers were only used as back reflectors. In *n-i-p* solar cells, back reflectors simultaneously act as metal back contacts. To reduce ohmic resistance in these back contacts, additional aluminium layers were used. Metal back contacts were deposited in the following order: aluminium (Al, 500 nm) / chromium (Cr, 30 nm) / silver (Ag, 300 nm). Similar to the structure that was used in section 4.4, silver is in contact with the solar cell and acts as back reflector. The addition of chromium and aluminium should ideally not affect the reflection of the silver layer.

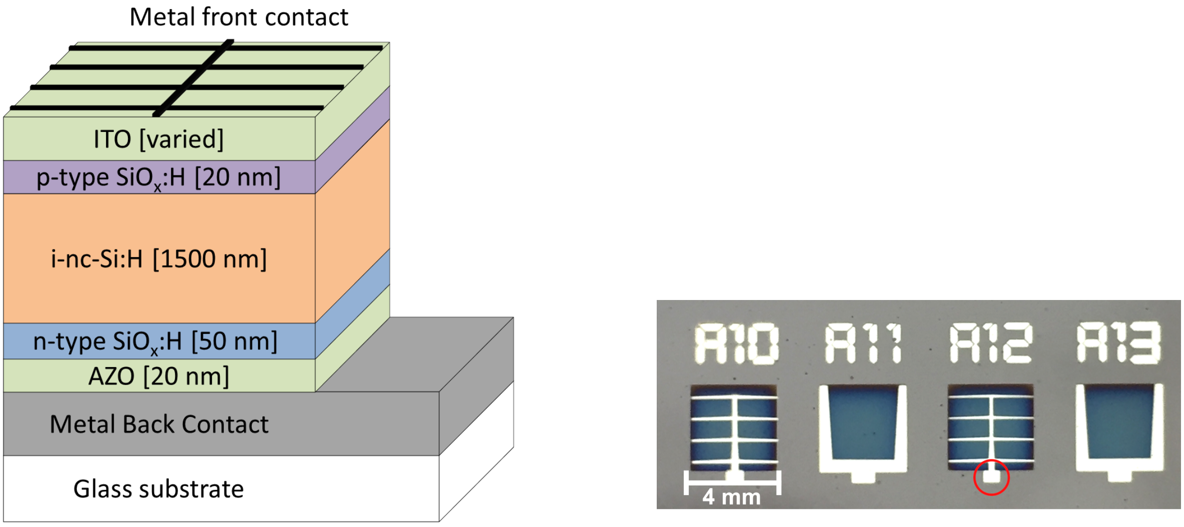

(a) **(b)**

Figure 5.1: (a) The structure of *n*-*i*-*p* solar cells that were deposited on textured glass and MST substrates. (b) Photograph of 4x4 mm^2 solar cells. The red circle indicates the front contact of the solar cell. The back contact is not displayed in this figure.

Aluminium-doped zinc oxide (AZO) layers (20 nm) were deposited on top of each back reflector, to reduce parasitic absorption in silver and shunting effects. Hydrogenated nanocrystalline silicon oxide layers (nc-SiO$_x$:H) were used as doped *n*- and *p*-layers to induce an electric field across the intrinsic nc-Si:H layer. Doped nc-Si:H layers have a low bandgap and absorb a significant fraction of incident light. Doped silicon oxide layers have a lower refractive index, a higher bandgap and therefore lower absorption, especially for wavelengths longer than 700 nm [21]. The *p*-nc-SiO$_x$ layer acts as a transparent window layer, while the *n*-nc-SiO$_x$ is part of the back reflector [21]. The AZO layer and all silicon layers were deposited in the *Amigo* plasma enhanced chemical vapour deposition (PECVD) cluster tool. The precursor gases SiH_4, H_2, CO_2 and PH_3 or B_2H_6 were used for doped layers. Intrinsic nc-Si:H layers were deposited by using only SiH_4 and H_2 as precursor gases.

An indium tin oxide (In_2O_3:Sn, ITO) layer was used as transparent conductive oxide (TCO) layer. The thickness of this layer was varied, to investigate the effect on the performance of devices (section 5.3). Finally, a metal front grid was evaporated to collect the holes at the front side of the device. To protect the surface of the ITO layer, first, a 100 nm Ag layer was evaporated using thermal evaporation (subsection 3.1.3). Subsequently, 30 nm Cr and 300 nm Al were evaporated using e-beam evaporation. Devices were connected to the measurement equipment using two probes: one connected to the front contact of the cell, and one connected to the back contact at the edge of the sample. Figure 5.1b shows a photograph of solar cells that were fabricated. Solar cells with a metal front grid (A10 & A12) were used for evaluating current density-voltage (J-V) curves, while solar cells with an edge front contact (A11 & A13) were subjected to external quantum efficiency (EQE) measurements.

5.2. Modulated Surface Texture Solar Cells

The third scientific research question that was introduced in section 1.6 was: *Is it possible to fabricate a functioning nc-Si:H solar cell, based on periodic-random MST structures, and what is the effect of introducing an MST structured back reflector on the performance of an n-i-p nc-Si:H solar cell?*. To give an answer to this question, back reflectors on MST substrates were subjected to the deposition process of thin film silicon solar cells. For the fabrication of solar cells, only MST structures based on two-dimensional (2D) periodic gratings were considered. According to the temporal coupled mode theory, 2D gratings allow for greater values of the absorption enhancement factor compared to one-dimensional (1D) gratings. Therefore, devices on 2D structures were expected to perform better than devices on 1D structures. First, the J-V characteristics of solar cells were measured, to evaluate whether functioning devices could be manufactured. Figure 5.2 presents the current density-voltage characteristics of two 4x4 mm^2 devices that were fabricated in the first batch of solar cells. Very similar curves were measured for most other solar cells in this batch.

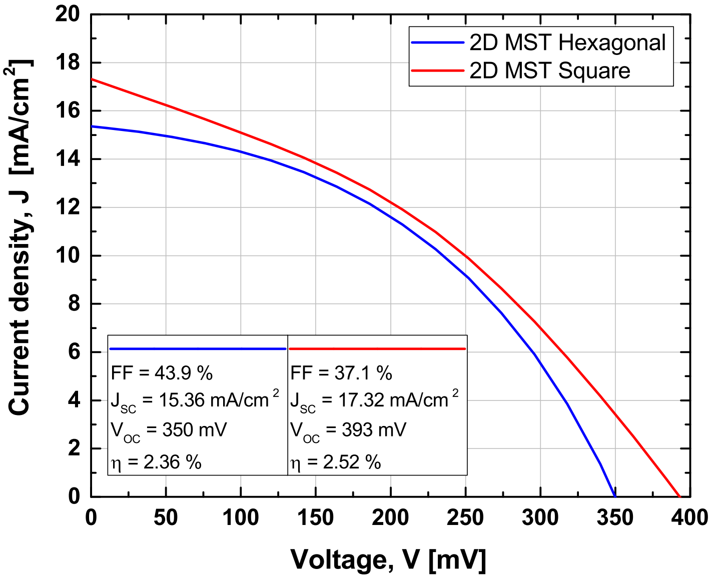

Figure 5.2: J-V curves of two 4x4 mm^2 nc-Si:H solar cells, based on modulated surface textures with hexagonal and square lattice structures. The period of both gratings was equal to $L = 2000$ nm.

The question whether functioning nc-Si:H solar cells could be manufactured on periodic-random MST structures, was answered with these results. Figure 5.2 presents J-V curves that show (non-ideal) diode behaviour. Therefore, these graphs correspond to functioning solar cells. However, the external parameters of both devices are relatively poor. In section 1.5, external parameters of solar cells were discussed in detail. This section introduced the two-diode equivalent circuit of solar cells, including series and shunt resistance. Using this knowledge, it is clear that both devices in figure 5.2 suffer from high series resistance (R_s) and low shunt resistance (R_p). Both have a detrimental effect on the fill factor of these solar cells, which is significantly below 50 %.

High series resistance in these devices might have been caused by non-ohmic semiconductor-metal contacts at the front and/or back side of the solar cells. To reduce series resistance, a thermal annealing step was deployed. This thermal annealing step, 30 minutes at 130 °C, was used after the deposition of silicon layers, ITO and metal front grid. A Thermo Scientific oven [86] was used for the thermal annealing processes. Devices that were obtained after applying 30 minutes thermal annealing showed less series resistance and higher fill factors (figure 5.5a).

The cause of severe shunting behaviour that the solar cells in figure 5.2 showed was less obvious. Scanning electron microscope (SEM) images were obtained, to investigate the front surface of the solar cells. Figure 5.3 presents two SEM images, taken with 1200x and 8000x magnification, respectively. Figure 5.3a shows a surface that consists of expected large craters, in which 2D periodic grating features are clearly present. However, when the magnification is increased, the presence of small holes in the 2D hexagonal lattice structure was discovered. It seems that the silicon layer depositions did not fully cover the substrate in some locations, indicated by red circles in figure 5.3b. If there is direct contact between the metal back contact and the front TCO, these spots could act as shunts in the solar cell, resulting in a very low shunt resistance.

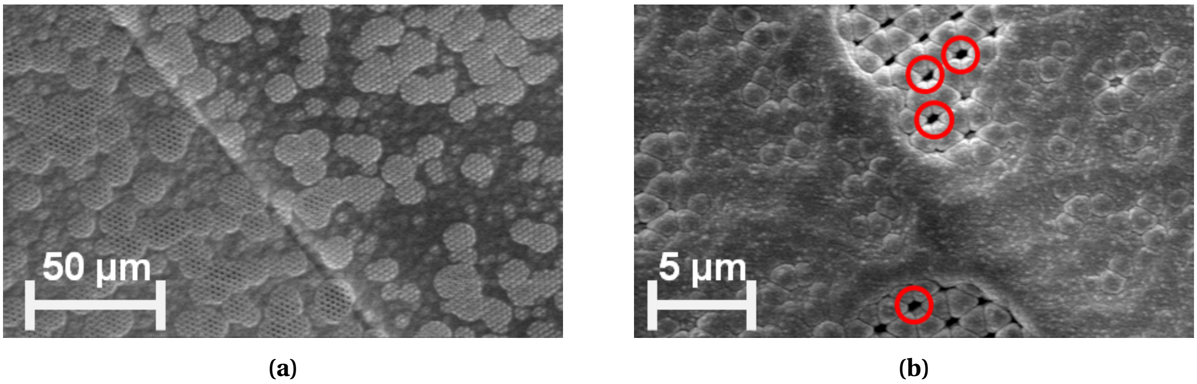

(a) (b)

Figure 5.3: SEM images of the front surface of a 2D MST nc-Si:H solar cell, taken with a magnification of (a) 1200x and (b) 8000x. Red circles indicate small holes in the hexagonal lattice structure.

The SEM images in figure 5.3 correspond to a solar cell on an early 2D MST substrate, obtained by spin coating photoresist at 1750 rpm. As explained in subsection 4.3.1, the rotational speed of the spin coating process was increased to 2250 rpm to obtain a thinner photoresist layer. Besides preserving more craters, a thinner photoresist layer could also reduce the height of the grating features. Reducing this height might reduce the number of small holes in the surface. Besides that, the period of the gratings was increased from 2000 nm to 3000 and 4000 nm, to increase the distance between the grating features.

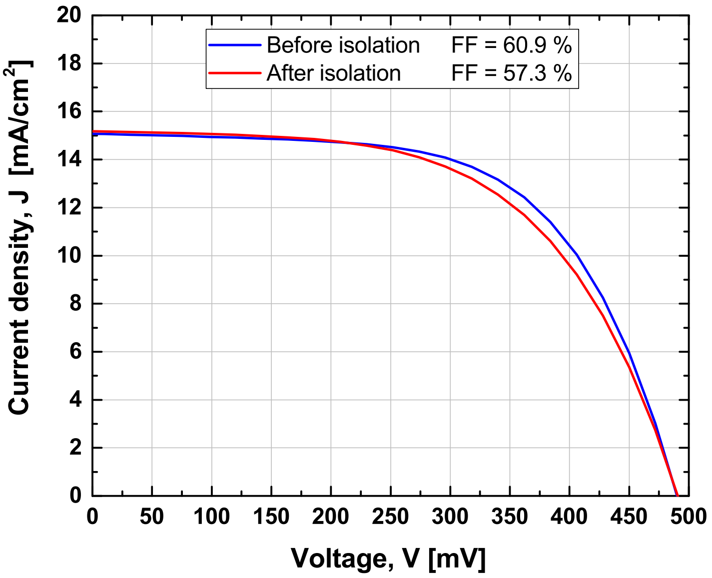

Figure 5.4: J-V characteristics of nc-Si:H solar cells, before and after isolation by laser scribing.

Furthermore, current leakage along the edges of the samples was suspected. Therefore, cells from a new batch, spin coated at 2250 rpm, were isolated using a MOPA 30 W fiberlaser [87]. Power and speed of the laser were adjusted such that a cut in the silicon and TCO layers was made, without affecting the metal back contact. Measured J-V curves before and after isolating are presented in figure 5.4. It is clear that the shunting behaviour of these devices is already significantly reduced compared to figure 5.2. Unfortunately, no significant change in shunt resistance was found after isolating the solar cell. The fill factor of the isolated device slightly decreased. Therefore, isolation of individual cells using laser scribing was not considered as an effective method to increase the shunt resistance.

A new batch of nc-Si:H solar cells was fabricated, taking the proposed adjustments into account. From these devices, a solar cell manufactured on a 2D modulated surface texture, based on a hexagonal grating with a period $L = 4000$ nm, performed best. An efficiency (η) of 5.26 %, open-circuit voltage (V_{OC}) of 497 mV and short-circuit current density (J_{SC}) of 16.68 mA/cm^2 were reached. The J-V curve corresponding to this 4x4 mm^2 solar cell is presented in figure 5.5a. An ITO layer of 75 nm was used for this particular device. With this result, the first nc-Si:H solar cell, with a fill factor exceeding 65 %, based on a periodic-random modulated surface texture is reported.

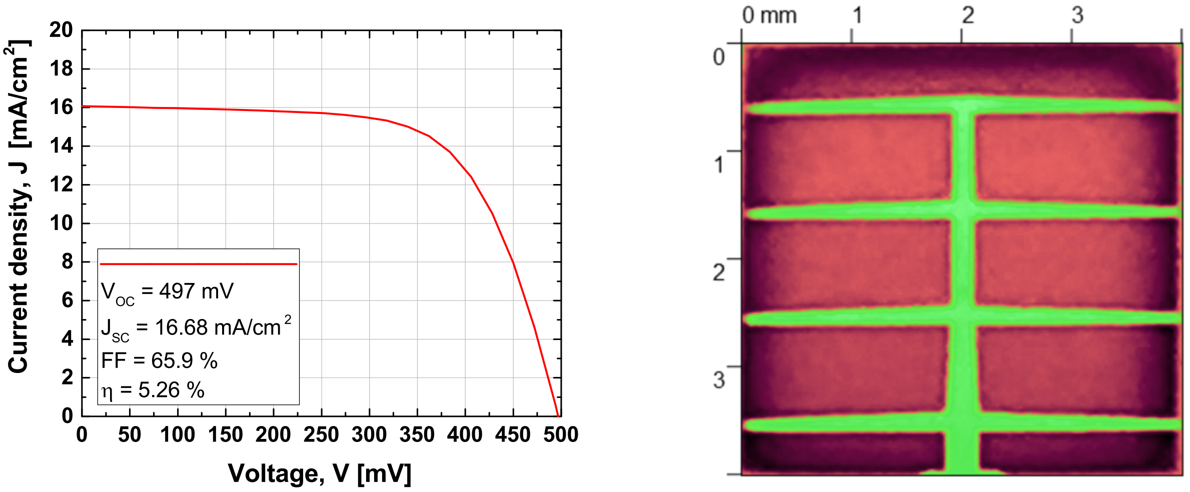

(a) **(b)**

Figure 5.5: (a) J-V characteristic of the best performing cell, obtained on an MST substrate, based on a hexagonal lattice structure periodic grating with a period of $L = 4000$ nm. (b) Photograph of a solar cell with a metal front grid covering 18.6 % of the surface (indicated in green).

In Figure 5.5b, the area covered by the metal front contact is marked in green. This figure was obtained by importing a photograph of the solar cell into Gwyddion 2.49 software [66] and using automatic detection of the metal front grid area. The mas for metal evaporation was designed to cover approximately 10 % of the surface. However, analysis of the image showed that 18.6 % of the 4x4 mm^2 surface was covered. Therefore, the active area of fabricated solar cells was not equal to 16 mm^2, but approximately 13 mm^2. The active area current density-voltage curve of the solar cell was obtained by dividing the current measurements by an area of 13.024 mm^2.

The definition of active solar cell area is crucial for the result of external solar cell parameters, such as J_{SC} and efficiency. A small error in quantifying the active area of a solar cell could lead to large deviations in the magnitude of external parameters. To validate whether the magnitude of the active area, that resulted from image analysis, was approximated correctly, the J_{SC} value was compared to the photo-generated current that resulted from EQE measurements. As explained in subsection 3.2.5, the measurement beam for EQE measurements was focused in a point with a diameter of a few millimetres on the device under test. On the other hand, the distance between two fingers of the metal front contact was less than 1 mm (figure 5.5b). Therefore, the size of the EQE measurement spot was too large to fit between two fingers of the metal front contact. To avoid incorrect EQE measurements, cells with front edge contacts, shown in figure 5.1b, were used. On a sample with solar cells, *edge-contacted* cells and *grid-contacted* cells were alternated. Hence, EQE results presented in this work always correspond to one of the edge-contacted cells, closest to the grid-contacted cell used for J-V measurements.

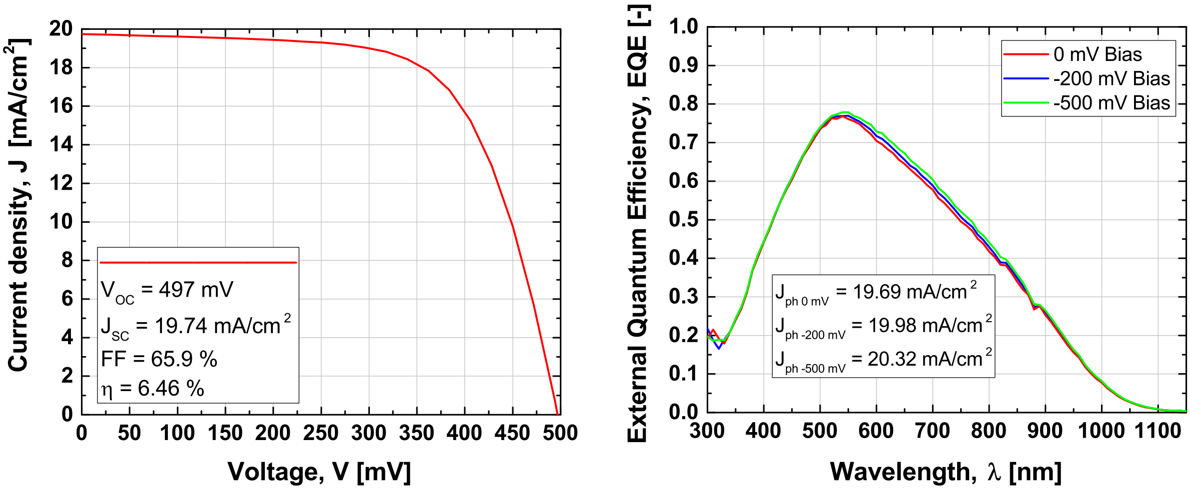

(a) (b)

Figure 5.6: (a) Active area J-V characteristic of the best performing solar cell, obtained on a periodic-random MST ($L = 4000$ nm, hexagonal lattice). (b) EQE measurements of the nearest edge-contacted solar cell.

Figure 5.6a shows the active area J-V curve of the solar cell, corresponding to figure 5.5a. As can be seen, a J_{SC} of 19.74 mA/cm^2 with an active area efficiency of 6.46 % was achieved on a 2D hexagonal modulated surface texture. Figure 5.6b presents EQE measurements for the nearest edge-contacted device, next to the solar cell that was characterised by its J-V behaviour. Measurements were obtained without bias voltage and reverse bias voltages of -200 and -500 mV. A reverse bias voltage was applied to ensure efficient collection of generated charge carriers. The external quantum efficiency measurement of figure 5.6b was used to calculate the photo-generated current, using equation 3.4. EQE measurements were taken under short-circuit conditions. Hence, photo-generated current can be compared to J_{SC} values of J-V measurements to validate the active area definition. A photo-generated current of 19.69 mA/cm^2 was obtained by EQE measurements without bias voltage. This value is very close to the active area corrected J_{SC} of 19.74 mA/cm^2, which resulted from J-V measurements. Therefore, it was concluded that external parameters of individual solar cells could be corrected, using image analysis to obtain the active area.

Furthermore, EQE measurements under different reverse bias voltages did not show a remarkable difference. If measurements under reverse bias voltage would have lead to significantly different EQE graphs, that would be an indication for low quality junctions, containing many recombination centres. For this device, the amount of collected charge carriers does not seem to change significantly under different bias voltages.

To summarise, this work reports functioning nc-Si:H solar cells on modulated surface textures, based on 2D hexagonal periodic gratings and randomly textured glass substrates. These devices were obtained after decreasing the thickness of the applied photoresist layer and increasing the period of the hexagonal lattice grating. An active area efficiency of 6.46 % was reached for devices of 4x4 mm^2, with a J_{SC} of 19.74 mA/cm^2 and V_{OC} of 497 mV. EQE measurements validated the method that was used to correct the external parameters for inactive area.

5.3. Influence of Front Transparent Conductive Oxide Layer Thickness

Thickness of TCO layers at the front side of solar cells has a strong influence on the performance of devices. In this work, ITO layers were used as a front TCO. Thick ITO layers have the advantage of introducing low series resistance, but simultaneously lead to an increase in parasitic absorption of incident light. Especially in the short wavelength range, ITO layers absorb a significant part of the incident light. Solar cells, with a structure that was described in section 5.1 and front ITO layers of 65, 70, 75, 80 and 85 nm, were manufactured on 2D MST substrates. The reflectance of all devices was measured using spectrophotometry. The size of the measurement beam was adjusted to fit on a 4x4 mm^2 edge-contacted solar cell. Reducing the amount of light that was incident on the sample caused more noise in the measurements, especially for longer wavelengths (λ > 860 nm). Hence, the wavelength range of 300-850 nm was examined.

Figure 5.7a presents graphs of the value $1-R$ for a range of ITO layer thicknesses. The graphs seem to reach lower average values for thicker ITO layers. This indicates that either the front reflection or the absorption in the ITO layer increased. Simultaneously, maxima of all graphs seem to shift to longer wavelengths for thicker ITO layers. For solar cell applications, the value for $1-R$ is preferred as high as possible, to have the maximum amount of light available for absorption in active layers. Based on figure 5.7a, a 65 nm ITO layer would be most favourable, due to significantly higher values of $1-R$ for wavelengths between 400 and 600 nm.

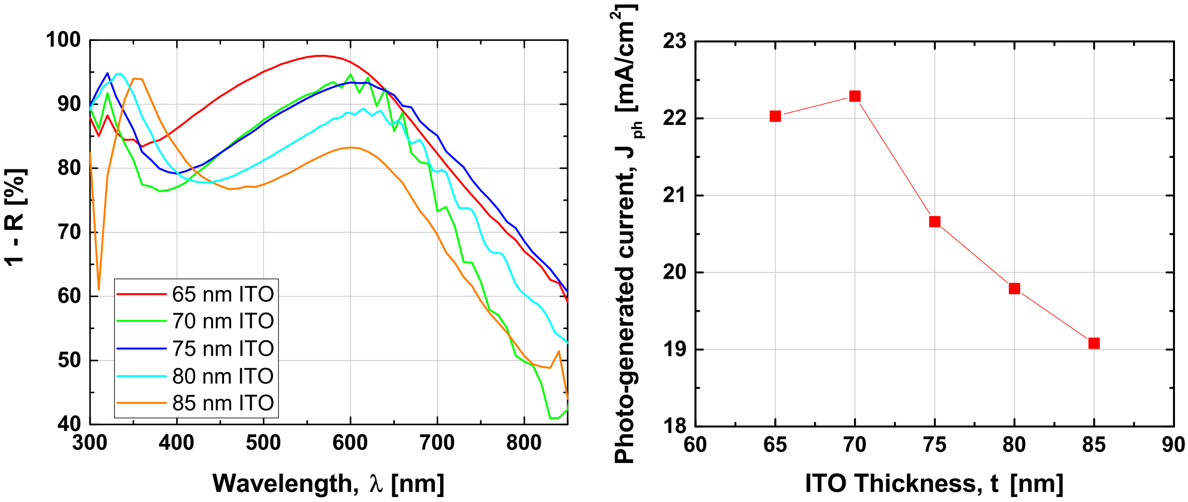

(a)

(b)

Figure 5.7: (a) $1-R$ graphs and (b) photo-generated current ($V_{bias}=-1$ V) for various front ITO layer thicknesses.

The photo-generated current of solar cells that were subjected to reflectance measurements, was evaluated using EQE measurements. A reverse bias voltage of -1 V was applied to all devices to avoid the effect of *n-i-p* junction quality on the photo-generated current. Both EQE measurements and reflectance measurements corresponded to devices based on a 2D MST substrate with a hexagonal lattice structure and $L = 4000$ nm period. Figure 5.7b presents the photo-generated current that was obtained by biased (-1 V) EQE measurements.

Measured values show a clear trend: the photo-generated current decreases significantly for ITO layers thicker than 70 nm. This is in accordance with the results that were obtained in figure 5.7a. Therefore, thick ITO layers do not seem to be beneficial for the solar cell performance. Figure 5.8a shows the external quantum efficiency measurement results for an ITO thickness of 65 and 80 nm, measured under -2 V reversed bias voltage. In this graph, it is very obvious that the thicker ITO layer results in lower EQE values, especially in the short wavelength range. For wavelengths longer than

700 nm, the thickness of the ITO layer does not seem to effect the EQE characteristic.

Despite the fact that a thinner ITO layer yields optically favourable results, the best-performing device on a 2D MST structure, presented in section 5.2, included a front ITO layer of 75 nm. This result indicates the trade-off between optical and electrical properties of the ITO layer. It is well known that resistivity of ITO layers decreases when the thickness of layers increases [88]. To investigate the effect of ITO layer thickness on the J-V characteristics of solar cells, the nearest grid-contacted solar cells were evaluated. Figure 5.8b presents the J-V curves of these solar cells.

The J_{SC} values follow the trend that was predicted by the photo-generated current measurements of figure 5.7b. An ITO layer of 65 nm results in the highest J_{SC} of 19 mA/cm^2, while a layer of 85 nm results in the lowest J_{SC} of 15 mA/cm^2. The solar cell with the highest fill factor (FF) of 66.2 % is based on a 75 nm front ITO layer. This device seems to suffer the least from series resistance. The other devices show lower fill factors, but no clear distinction between high and low series resistance could be made.

Taking into account that a 75 nm front ITO layer resulted in the most efficient solar cell, and that most devices based on a 75 nm ITO layer showed relatively high J_{SC} values, a thickness of 75 nm for the front ITO layer was considered as optimal for 2D MST devices.

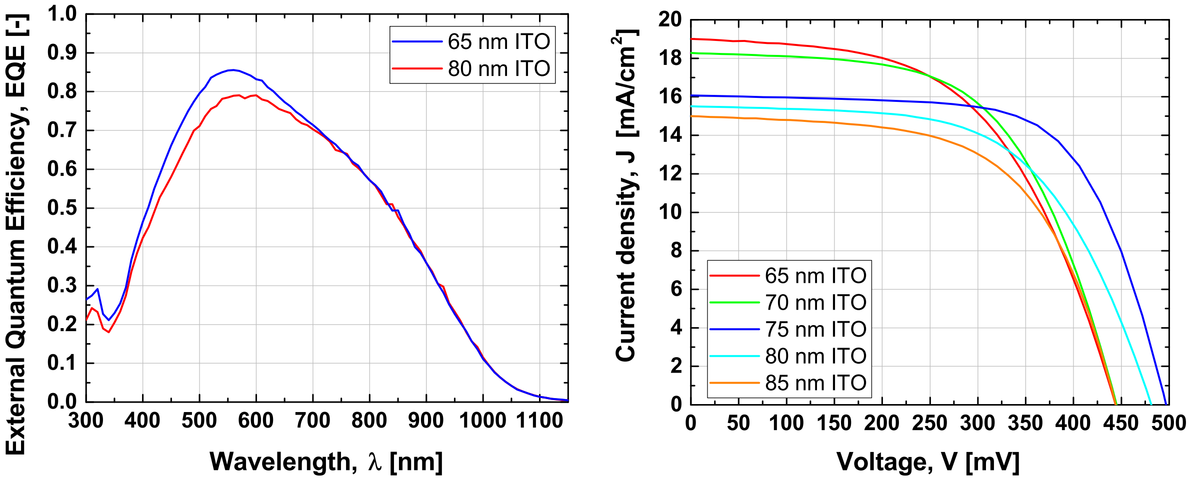

(a) **(b)**

Figure 5.8: (a) EQE of solar cells based on a 65 and 80 nm front ITO layer (V_{bias} = -2 V) and (b) J-V characteristic of solar cells with different front ITO layer thicknesses, based on a 2D MST hexagonal lattice substrate with a period $L = 4000$ nm.

5.4. Solar Cells on Different Substrates

Solar cells on 2D MST substrates, based on hexagonal and square lattice gratings with periods of 3000 and 4000 nm, were fabricated and compared to devices based on randomly textured glass substrates. Because devices based on randomly textured glass were previously fabricated with an 80 nm ITO layer, 2D MST devices with the same ITO thickness were used for the comparison. External parameters were obtained by J-V measurements. To eliminate the influence of non-uniform substrates, external parameters were averaged over at least five functioning devices. The reported values are direct results from J-V measurements, and were not corrected for inactive area. Table 5.1 presents external parameters for devices based on square and hexagonal lattice 2D MST structures, with periods of 3000 and 4000 nm, respectively. J-V curves of individual devices that were used to average the external parameters can be found in appendix C.

Table 5.1: Averaged external parameters ± standard deviation, obtained over at least five different, functioning devices.

Lattice structure	Period [nm]	J_{SC} [mA/cm^2]	V_{OC} [mV]	FF [%]	η [%]
Hexagonal	3000	16.16 ± 1.9	490.4 ± 3.5	57.93 ± 7.7	4.54 ± 0.24
Square	3000	14.70 ± 4.6	453.6 ± 10	56.74 ± 2.7	3.78 ± 1.2
Hexagonal	4000	16.38 ± 1.3	482.3 ± 7.3	54.80 ± 7.1	4.31 ± 0.49
Square	4000	14.51 ± 0.9	444.1 ± 33	55.13 ± 4.2	3.56 ± 0.48

These results show that 2D MST substrates based on hexagonal lattice structures lead to slightly better external parameters, compared to square lattice structured MST substrates (except from the fill factor). Especially the short-circuit current seems to be significantly higher for hexagonal MST structures, compared to square structures. One could argue that a hexagonal periodic grating excites more guided resonances (section 2.4.1) and therefore benefits from higher absorption enhancement factors for wavelengths around 1000 nm. However, when EQE graphs of a 2D MST solar cell based on a square and hexagonal lattice are compared (figure 5.9a), no significant differences were found. If absorption enhancement for wavelengths close to 1000 nm would have caused the difference in performance, this should have been clearly visible in the EQE graphs. Most probably, the electrical performance of solar cells had more influence on the efficiency, J_{SC} and V_{OC}, rather than on the optical performance. The duty cycle of the periodic gratings might have affected the electrical performance of solar cells. As explained in section 2.4, the duty cycle of 2D periodic gratings was defined as the ratio between the area of grating features and the area of the unit cell. The duty cycle was 0.25 for square lattice gratings and 0.21 for hexagonal lattice gratings. These duty cycles indicate that hexagonal grating features cover relatively less of the total area compared to square lattice gratings. This could have resulted in less defective nc-Si:H layers that could have increased the efficiency of the devices.

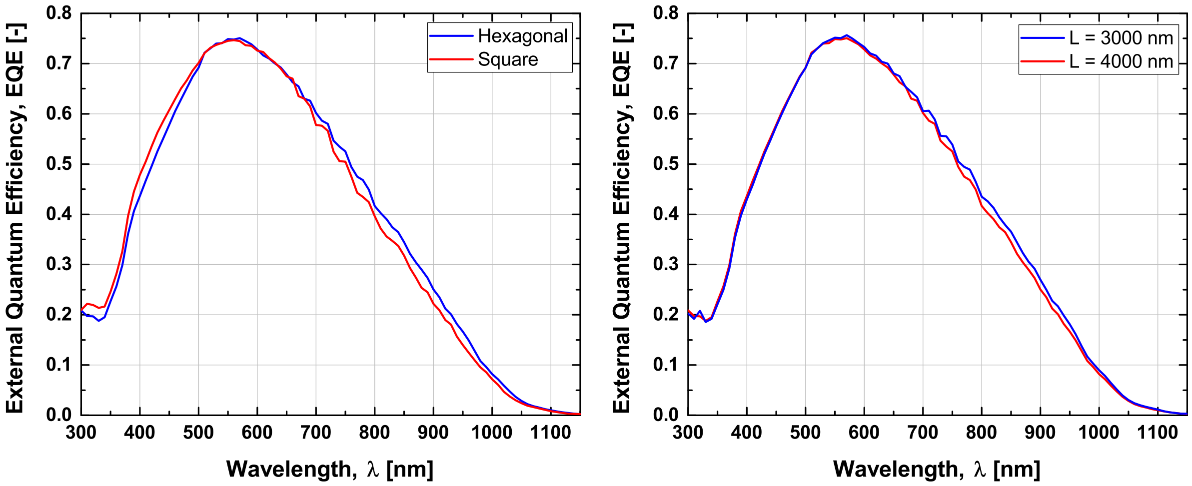

(a) Period $L = 4000$ nm, different lattice structures.

(b) Hexagonal lattice, different periods.

Figure 5.9: EQE curves of 2D MST nc-Si:H solar cells (V_{bias} = -2 V): lattice structure and period compared.

Furthermore, the results in table 5.1 did not show significant performance differences between 3000 and 4000 nm periods, for both hexagonal and square lattice structures. Figure 5.9b presents EQE graphs of solar cells based on a hexagonal lattice 2D MST structure, with periods of 3000 and 4000 nm. Both EQE graphs follow a very similar, almost equal trend.

Although the influence of non-uniformity of samples on the performance of solar cells was avoided as much as possible by averaging external parameters over at least five devices, some of the standard deviation values are relatively high. For instance, the value for J_{SC} corresponding to square lattice gratings ($L = 3000$ nm) has a standard deviation of more than 30 %. Figure C.1b in appendix C shows that two of the five devices suffer from low J_{SC} values, while these cells were fabricated on the same substrate. Therefore, non-uniformity issues still seem to be present and could have had influence on other measurement results.

To evaluate whether the 2D MST structured back reflector has contributed to the performance of solar cells, previously discussed results were compared to results of solar cells based on randomly textured glass. External parameters were averaged over 20 functioning devices and were not corrected for inactive area. Table 5.2 presents the external parameters for these solar cells.

Table 5.2: Averaged external parameters corresponding to nc-Si:H solar cells based on randomly textured substrates.

Parameter	Unit	Average value	± Standard deviation
J_{SC}	[mA/cm^2]	16.66	± 1.6
V_{OC}	[V]	493.7	± 8.5
FF	[%]	61.77	± 4.0
η	[%]	5.07	± 0.51

All external parameters for solar cells on randomly textured substrates are better than the external parameters corresponding to 2D MST based solar cells. Although the light scattering behaviour of MST substrates showed promising results, solar cells based on these substrates did not result in an improvement for any external parameter. Most probably, grating features introduced additional defects in the nc-Si:H structure, resulting in recombination centres. This affected all external parameters. To finalise this comparison, figure 5.10 presents the J-V characteristics of the best performing devices on randomly textured and 2D hexagonal (L = 4000 nm) substrates, respectively. Both J-V curves were corrected for 18.6 % inactive area.

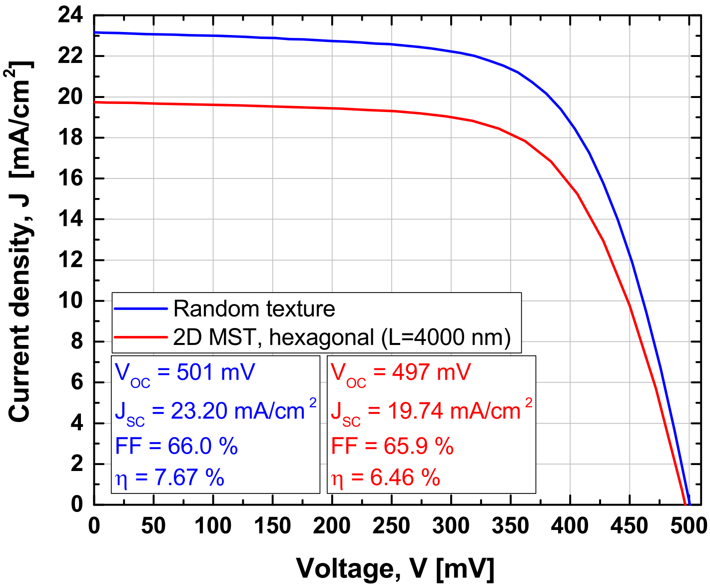

Figure 5.10: Active area J-V characteristics of the best performing solar cells, based on a randomly textured and 2D MST hexagonal (L = 4000 nm) substrates.

5.5. Conclusions

This chapter discussed the results that were obtained for nc-Si:H solar cells, based on different substrates. The aim of this chapter was answering the question whether it is possible to fabricate a functioning nc-Si:H solar cell, based on 2D MST structures. Additionally, the effect of introducing an MST substrate on the performance devices was investigated.

To explore the possibility of manufacturing functioning devices on 2D MST substrates, *n-i-p* solar cells with a structure based on the work of Yang [21] were fabricated. The first J-V curves that were obtained did not show promising results. Low fill factors of 43.9 % and 37.1 % were obtained for hexagonal and square lattice modulated surface textures ($L = 2000$ nm), respectively. SEM images showed small pin holes in the surface. It was suspected that these pin holes acted as shunts in the device, dramatically affecting the external parameters of the fabricated solar cells. Increasing the rotational speed during the spin coating process, and making use of larger grating periods, resulted in a device with a fill factor of 65.9 %.

To correct the external parameters for inactive area, the magnitude of the surface that was covered by the metal front contact was quantified using image analysis software. It was found that 18.6 % of the solar cell area was covered with metal, instead of the 10 % value that was expected. Corrected J_{SC} values were compared to photo-generated current values, resulting from EQE measurements. Correcting the current density values with a factor of 18.6 % was found to be in accordance to EQE results. The best performing solar cell, based on a hexagonal, 4000 nm 2D MST, had an active area efficiency of 6.46 %, a J_{SC} of 19.74 mA/cm^2 and a V_{OC} of 497 mV.

Furthermore, the influence of the front ITO thickness was investigated. Increasing the thickness of this ITO layer, resulted in a lower photo-generated current and $1 - R$ value. On the other hand, it is well known that thin ITO layers suffer from higher series resistance. A trade-off between electrical and optical performance was made and resulted in an optimal ITO layer thickness of 75 nm for solar cells based on a 2D MST substrate.

Additionally, nc-Si:H solar cells based on different 2D MST and randomly textured glass substrates were compared. J_{SC} and efficiency values were higher for solar cells based on hexagonal lattice MST substrates, compared to square lattice MST substrates. Comparison of EQE graphs showed no significant difference in absorption. Therefore, the difference in performance was attributed to electrical properties of the solar cells. Hexagonal grating structures have a lower duty cycle than square grating structures, which could have resulted in less defective nc-Si:H layers, increasing the efficiency of the devices.

Finally, the best performing device on a randomly textured substrate was compared to a 2D hexagonal, 4000 nm MST substrate. The solar cell based on randomly textured glass performed better than the 2D MST device. An active area efficiency of 7.67 % and J_{SC} of 23.2 mA/cm^2 were reached for this device. It can be concluded that periodic-random modulated surface textures can lead to functioning nc-Si:H solar cells. However, a surface morphology optimisation is required to try to improve the electrical properties of these devices.

6

Conclusions and Recommendations

This chapter provides a summary of the most important findings that were presented in this thesis and provides recommendations for further research. The aim of this thesis was introduced in chapter 1 and was summarised by the following statement:

To fabricate and characterise a modulated surface texture substrate based on large, random features, superimposed by smaller, periodic gratings, and to investigate the effect of the substrate on the performance of a nc-Si:H solar cell.

This statement was subdivided in three scientific questions. The following three sections will discuss the results that lead to the answer on each of the questions.

6.1. Fabrication of Random-Periodic Modulated Surface Textures

The first scientific question, based on the aim of this work, was stated as follows:

Is it possible to fabricate an MST structure that consists of a large, random texture, superimposed by a smaller, periodic grating?

Chapter 4 investigated the possibility to fabricate modulated surface texture (MST) structures. Randomly textured substrates were obtained by wet etching glass substrates, coated with a sacrificial indium tin oxide (ITO) layer. The best randomly textured substrates, in terms of uniformity and reproducibility, were obtained by the deposition of 200 nm ITO and a wet etching process of 30 minutes. Fabricated substrates showed surfaces consisting of several craters. Substrates with a root mean square roughness $\sigma_{RMS} = 352.6 \pm 39.1$ nm and an aspect ratio $AR = 0.12 \pm 0.017$ were obtained. These substrates were used as a basis to investigate the fabrication of modulated surface textures.

One- (1D) and two-dimensional (2D) periodic gratings were obtained using a photolithography process. Atomic force microscopy (AFM) images showed that development time had a large influence on the shape and size of periodic gratings. An optimisation study based on 1D gratings resulted in a development time of 70 s to maintain the intended surface morphology of grating features. 2D gratings, based on hexagonal and square lattice structures, were fabricated with the same process parameters and clearly reproduced the structure.

To answer the first sub question that was introduced in section 1.6, samples based on a combination of randomly textured substrates and 1D gratings were developed. Using randomly textured substrates as a basis for the photolithography process, resulted in modulated surface texture substrates. The first results were promising: grating structures were successfully superimposed on random textures. However, many small craters were flattened out, resulting in samples with an average surface roughness of $\sigma_{RMS} = 221.8 \pm 80.6$ nm. By increasing the rotational speed of the spin coating process, thinner layers of photoresist were obtained on the randomly textured substrates. This resulted in a sample, preserving both the random and periodic surface morphologies for MST substrates based on 1D and 2D gratings. Therefore, it was concluded that modulated surface textures, based on large random features superimposed by smaller periodic gratings, could be fabricated using randomly textured glass and a photolithography process.

6.2. Scattering Properties and Absorption

The second scientific question introduced in chapter 1 was:

How do textures, gratings and modulated surface textures influence the propagation of light?

An optical characterisation study was carried out in chapter 4, to investigate light propagation and scattering properties of various substrates. Angular intensity distribution (AID) measurements showed that randomly textured substrates induce broadband scattering in a narrow cone around the specular component.

AID plots for periodic gratings clearly showed scattering to distinct diffraction modes, predicted by the grating equation. Compared to randomly textured substrates, periodic gratings allowed for relatively high intensity light scattering to wide angles, close to 90°. Increasing the grating period lead to an increase in the number of excited diffraction modes. High intensity light scattering to large angles, can lead to a significant increase in optical path length in solar cell structures.

Analysis of MST samples showed that the optical behaviour was a superposition of the individual scattering mechanisms corresponding to random textures and periodic gratings, respectively. The AID plot of MST substrates showed clear, distinct diffraction modes, combined with broadband light scattering around these modes. The properties introduced by the random texture, resulted in light scattering to angles that were not predicted by the grating equation. Therefore, modulated surface textures, based on random and periodic features, showed promising behaviour to obtain high intensity light scattering into a wide range of angles.

The influence of different back reflectors on light absorption in nc-Si:H layers was investigated as well. When 2D MST substrates were used to investigate absorption in a stack of silver, 100 nm amorphous silicon oxide (a-SiO_X:H) and 1500 nm hydrogenated nanocrystalline silicon (nc-Si:H), high parasitic absorption in the silver back reflector was found for long wavelengths. Small 2D grating features might have significantly contributed to this parasitic absorption. Simultaneously, MST substrates seemed to increase the absorption in the short wavelength range. This was probably caused by reduced front reflection.

6.3. Nanocrystalline Solar Cells on Modulated Surface Textures

Chapter 5 aimed to answer the final scientific question that was introduced in chapter 1:

Is it possible to fabricate a functioning nc-Si:H solar cell, based on periodic-random MST substrates, and what is the effect of introducing an MST structured back reflector on the performance of an n-i-p nc-Si:H solar cell?

Two-dimensional modulated surface texture substrates, based on hexagonal and square lattice gratings, were used as a substrate for *n-i-p* solar cells. A metal back contact of 500 nm aluminium (Al), 30 nm chromium (Cr) and 300 nm silver (Ag), was deposited first. Solar cells were deposited in the following sequence: aluminium-doped zinc oxide (AZO, 20 nm), n-type SiO_X:H (50 nm), intrinsic nc-Si:H (1500 nm), p-type SiO_X:H (20 nm). Finally, an ITO layer and front metal contact (100 nm Ag, 30 nm Cr, 300 nm Al) were deposited. The first solar cells did not show promising results. Fill factors below 45 % were achieved, indicating significant shunting and high series resistance issues. Scanning electron microscope (SEM) images showed small pin holes that could act as recombination centres and could cause shunting of the device. A thermal annealing step, larger grating periods and thinner photoresist layers were introduced. This resulted in a 2D hexagonal MST (L = 4000 nm) solar cell, with an active area efficiency of 6.46 %, short-circuit current density (J_{SC}) of 19.74

mA/cm^2, and an open-circuit voltage (V_{OC}) of 497 mV.

The thickness of the front ITO layer had a significant impact on the photo-generated current. Thinner ITO layers were beneficial for the photo-generated current. However, higher series resistance seemed detrimental to the performance of fabricated devices. A 2D MST device based on an ITO layer of 75 nm showed the best performance.

Comparing the performance of nc-Si:H solar cells based on different 2D MST substrates resulted in an interesting finding. Solar cells based on 2D hexagonal lattice substrates seemed to perform better than their square lattice counterparts. However, external quantum efficiency (EQE) measurements did not show remarkable differences between both substrates. The difference in performance was attributed to the electrical properties of the solar cells. A lower duty cycle for hexagonal lattice structures, compared to square lattice structures, could have benefited the growth of less defective nc-Si:H layers.

Finally, the performance of the best device on a 2D MST substrate was compared to the performance of the best device based on randomly textured glass. The device based on randomly textured glass reached an active area efficiency of 7.67 %, a J_{SC} of 23.2 mA/cm^2, and a V_{OC} of 501 mV. It is clear that these external parameters exceed those of the devices based on 2D hexagonal MST substrates. Overall, it can be concluded that functioning nc-Si:H solar cells, based on periodic-random MST substrates, can be fabricated. An optimisation of the surface morphology and solar cell structure might lead to a better performance. If defective nc-Si:H layer growth could be avoided, 2D MST substrates are a promising basis for nc-Si:H solar cells.

6.4. Recommendations and Outlook

The efficiency difference between solar cells based on randomly textured glass and 2D MST substrates is large. However, periodic-random modulated surface textures showed promising behaviour in terms of light scattering. Improving the electrical performance of devices based on 2D MST substrates is the main challenge. If the surface morphology could be adjusted, such that growth of defective growth of nc-Si:H layers can be avoided, higher efficiencies could be achieved. A further decrease of the height of grating features might benefit less defective material growth.

A different process could be considered for the fabrication of periodic gratings on a randomly textured substrate. The photolithography process used in this work resulted in strange interference patterns on the samples multiple times, especially on flat glass samples. Unevenly spread photoresist and very small features in combination with a low vacuum contact exposure mode, could have caused these interference patterns. Ultraviolet nanoimprint lithography (UV-NIL) or reactive ion etching of a thin sacrificial layer, might lead to better results.

Furthermore, it might be interesting to develop an experiment to measure the absorption enhancement factor (F) for samples based on flat substrates with periodic gratings. Several tries to measure the absorption enhancement factor did not result in coherent results. Investigating whether the theoretical enhancement factor results hold for experimental devices could result in new insights into absorption enhancement using grating structures.

Bibliography

[1] NASA. Climate change: How do we know?, 2017. Retrieved from: `https://climate.nasa.gov/evidence/`. Accessed: 29/11/2017.

[2] V. Smil. *Energy Transitions: Global and National Perspectives.* ABC-CLIO, Santa Barbara, USA, 2016. ISBN 9781440853241.

[3] United Nations, Department of Economic and Social Affairs, Population Division. World population prospects: The 2017 revision, 2017. Retrieved from: `https://esa.un.org/unpd/wpp/Download/Standard/Population/`. Accessed: 29/11/2017.

[4] R. Johnston. Historical world population data, 2015. Retrieved from: `http://www.johnstonsarchive.net/other/worldpop.html`. Accessed: 29/11/2017.

[5] U.S. Energy Information Administration. International energy outlook 2017, 2017.

[6] E. Kabir, P. Kumar, S. Kumar, A. A. Adelodun, and K.-H. Kim. Solar energy: Potential and future prospects. *Renewable and Sustainable Energy Reviews*, **82**:894–900, 2018.

[7] O. Isabella. *Light management in thin-film silicon solar cells.* PhD thesis, Delft University of Technology, 2013.

[8] K. Branker, M. J. M. Pathak, and J. M. Pearce. A review of solar photovoltaic levelized cost of electricity. *Renewable and Sustainable Energy Reviews*, **15**(9):4470–4482, 2011.

[9] M. Planck. Ueber das gesetz der energieverteilung im normalspectrum. *Annalen der Physik*, **309**(3):553–563, 1901.

[10] A. H. M. Smets, K. Jäger, O. Isabella, R. A. C. M. M. Van Swaaij, and M. Zeman. *Solar energy: The physics and engineering of photovoltaic conversion, technologies and systems.* UIT, Cambridge, U.K., 2016. ISBN 9781906860325.

[11] R. Vismara. *Optical characterization of photovoltaic materials and structures for thin-film solar cells based on advanced texturization.* Master's thesis, Delft University of Technology, 2014.

[12] International Energy Agency. Snapshot of global photovoltaic markets, 2016.

[13] Centraal Bureau voor de Statistiek. Hernieuwbare electriciteit; productie en vermogen, 2018. Retrieved from: `https://opendata.cbs.nl/statline/#/CBS/nl/dataset/82610ned/table?ts=1527150359160`. Accessed: 24/05/2018.

[14] S. Philipps and W. Warmuth. Photovoltaics report. Technical report, Fraunhofer Institute for Solar Energy Systems (ISE), 2017.

[15] D. M. Bagnall and M. Boreland. Photovoltaic technologies. *Energy Policy*, **36**(12):4390–4396, 2008.

[16] M. Tao. *Terawatt Solar Photovoltaics: Roadblocks and Opportunities.* Springer, London, U.K., 2014. ISBN 9781447156420.

[17] National Renewable Energy Laboratory (NREL). Best research-cell efficiencies (30/10/2017), 2017. Retrieved from: `https://www.nrel.gov/pv/assets/images/efficiency-chart.png`. Accessed: 30/11/2017.

[18] M. A. Green, Y. Hishikawa, W. Warta, E. D. Dunlop, D. H. Levi, J. Hohl-Ebinger, and A. W. H. Ho-Baillie. Solar cell efficiency tables (version 50). *Progress in Photovoltaics: Research and Applications*, **25**(7):668–676, 2017.

[19] D. E. Carlson and C. R. Wronski. Amorphous silicon solar cell. *Applied Physics Letters*, **28**(11): 671–673, 1976.

[20] A. V. Shah. *Thin-film silicon solar cells*. EFPL Press, Lausanne, CHE, 2010. ISBN 9781420066746.

[21] G. Yang. *High-efficient n-i-p thin-film silicon solar cells*. PhD thesis, Delft University of Technology, 2015.

[22] R. W. Collins, A. S. Ferlauto, G. M. Ferreira, C. Chen, R. J. Koh, J.and Koval, Y. Lee, J. M. Pearce, and C. R. Wronski. Evolution of microstructure and phase in amorphous, protocrystalline, and microcrystalline silicon studied by real time spectroscopic ellipsometry. *Solar energy materials and solar cells*, **78**(1-4):143–180, 2003.

[23] International Electrotechnical Commission (IEC). Iec 60904-3:2016 measurement principles for terrestrial photovoltaic (pv) solar devices with reference spectral irradiance data, 2016.

[24] O. Isabella, H. Sai, M. Kondo, and M. Zeman. Full-wave optoelectrical modeling of optimized flattened light-scattering substrate for high efficiency thin-film silicon solar cells. *Progress in Photovoltaics: Research and Applications*, **22**(6):671–689, 2014.

[25] R.E. Treharne, A. Seymour-Pierce, K. Durose, K. Hutchings, S. Roncallo, and D. Lane. Optical design and fabrication of fully sputtered cdte/cds solar cells. *Journal of Physics: Conference Series*, **286**(1):012038, 2011.

[26] G. E. Jellison Jr. Optical functions of gaas, gap, and ge determined by two-channel polarization modulation ellipsometry. *Optical Materials*, **1**(3):151–160, 1992.

[27] S. M. Sze. *Physics of Semiconductor Devices*. John Wiley & Sons, Inc., New York, USA, 1969. ISBN 471842907.

[28] American Society for Testing and Materials (ASTM). Reference solar spectral irradiance: ASTM G-173, 2004. Retrieved from: `http://rredc.nrel.gov/solar/spectra/am1.5/`. Accessed: 26/09/2017.

[29] T. Matsui, H. Sai, T. Suezaki, M. Matsumoto, K. Saito, I. Yoshida, and M. Kondo. Development of highly stable and efficient amorphous silicon based solar cells. In *Proc. 28th European Photovoltaic Solar Energy Conference and Exhibition*, 2213–2217, 2013.

[30] H. Sai, K. Maejima, T. Matsui, T. Koida, M. Kondo, S. Nakao, Y. Takeuchi, H. Katayama, and I. Yoshida. High-efficiency microcrystalline silicon solar cells on honeycomb textured substrates grown with high-rate vhf plasma-enhanced chemical vapor deposition. *Japanese Journal of Applied Physics*, **54**(8S1):08KB05, 2015.

[31] H. Sai, T. Matsui, T. Koida, K. Matsubara, M. Kondo, S. Sugiyama, H. Katayama, Y. Takeuchi, and I. Yoshida. Triple-junction thin-film silicon solar cell fabricated on periodically textured substrate with a stabilized efficiency of 13.6%. *Applied Physics Letters*, **106**(21), 2015.

[32] Fraunhofer Institute for Solar Energy Systems ISE, 2017. Retrieved from: `https://www.ise.fraunhofer.de/content/dam/ise/en/documents/News/2017/0917_News_31_Percent_for-Silicon-based-multi-junction-solar-cell_e.pdf`. Accessed: 26/09/2017.

[33] P. T. Chiu, D. C. Law, R. L. Woo, S. B. Singer, D. Bhusari, W. D. Hong, A. Zakaria, J. Boisvert, S. Mesropian, R. R. King, and N. H. Karam. 35.8% space and 38.8% terrestrial 5j direct bonded cells. In *Proc. 2014 IEEE 40th Photovoltaic Specialist Converence (PVSC)*, 11–13, 2014.

[34] J. Zeitouny, E. A. Katz, A. Dollet, and A. Vossier. Band gap engineering of multi-junction solar cells: Effects of series resistances and solar concentration. *Scientific Reports*, **7**, 2017.

[35] F. U. Hamelmann, J. A. Weicht, and G. Behrens. Light-induced degradation of thin film silicon solar cells. *Journal of Physics: Conference Series*, **682**(1):012002, 2016.

[36] M. A. Green. *Solar cells: operating principles, technology, and system applications.* Prentice-Hall, Inc., Englewood Cliffs (NJ), U.S.A., 1982. ISBN 01382270.

[37] O. S. Heavens. *Optical properties of thin solid films.* Butterworths publications ltd., London, U.K., 1955. ISBN Reprint: 9780486669243.

[38] T. Fujibayashi, T. Matsui, and M. Kondo. Improvement in quantum efficiency of thin film si solar cells due to the suppression of optical reflectance at transparent conducting oxide/si interface by ti o 2/ zn o antireflection coating. *Applied physics letters*, **88**(18):183508, 2006.

[39] M. Zeman, O. Isabella, K. Jäger, R. Santbergen, R. Liang, S. Solntsev, and J. Krc. Advanced light trapping in thin-film silicon solar cells. *MRS Proceedings*, **1245**, 2010.

[40] G. R. Fowles. *Introduction to modern optics.* Courier Corporation, North Chelmsford (MA), U.S.A., 1975. ISBN Reprint: 9780486659572.

[41] A. V. Shah. *Thin-film silicon solar cells.* EPFL Press, Lausanne, CH, 2010. ISBN 9782940222490.

[42] F.-J. Haug and C. Ballif. Light management in thin film silicon solar cells. *Energy & Environmental Science*, **8**(3):824–837, 2015.

[43] C. Battaglia, C. Hsu, K. Söderström, J. Escarré, F.-J. Haug, M. Charrière, M. Boccard, M. Despeisse, D. Alexander, M. Cantoni, Y. Cui, and C. Ballif. Light trapping in solar cells: can periodic beat random? *ACS nano*, **6**(3):2790–2797, 2012.

[44] H. Sai, K. Saito, N. Hozuki, and M. Kondo. Relationship between the cell thickness and the optimum period of textured back reflectors in thin-film microcrystalline silicon solar cells. *Applied Physics Letters*, **102**(5):053509, 2013.

[45] E. Yablonovitch and G. D. Cody. Intensity enhancement in textured optical sheets for solar cells. *IEEE Transactions on Electron Devices*, **29**(2):300–305, 1982.

[46] E. Yablonovitch. Statistical ray optics. *JOSA*, **72**(7):899–907, 1982.

[47] Z. Yu, A. Raman, and S. Fan. Fundamental limit of light trapping in grating structures. *Optics express*, **18**(103):A366–A380, 2010.

[48] P. Sheng, A. N. Bloch, and R. S. Stepleman. Wavelength-selective absorption enhancement in thin-film solar cells. *Applied Physics Letters*, **43**(6):579–581, 1983.

[49] Z. Yu, A. Raman, and S. Fan. Fundamental limit of nanophotonic light trapping in solar cells. *Proceedings of the National Academy of Sciences*, **107**(41):17491–17496, 2010.

[50] O. Isabella, J. Krč, and M. Zeman. Modulated surface textures for enhanced light trapping in thin-film silicon solar cells. *Applied Physics Letters*, **97**(10):101106, 2010.

[51] H. Tan. *Materials and Light Management for High-Efficiency Thin-Film Silicon Solar Cells*. PhD thesis, Delft University of Technology, 2015.

[52] O. Isabella, A. Ingenito, D. Linssen, and M. Zeman. Front/rear decoupled texturing in refractive and diffractive regimes for ultra-thin silicon-based solar cells. In *Optical Nanostructures and Advanced Materials for Photovoltaics*, PM4C–2. Optical Society of America, 2013.

[53] H. Tan, E. Psomadaki, O. Isabella, M. Fischer, P. Babal, R. Vasudevan, M. Zeman, and A. H. M. Smets. Micro-textures for efficient light trapping and improved electrical performance in thin-film nanocrystalline silicon solar cells. *Applied Physics Letters*, **103**(17):173905, 2013.

[54] Polyteknik AS. Polyteknik AS - PVD Systems and Coating Service, 2005. Retrieved from: `http://www.polyteknik.com`. Accessed: 24/05/2018.

[55] D. M. Mattox. *Handbook of physical vapor deposition (PVD) processing*. Elsevier Inc., Oxford, U.K., 2010. ISBN 9780815520375.

[56] Provac vacuum technology. Pro 500/650/800/950/1100 high vacuum pvd coating system, 2008. Retrieved from: `https://www.provac-gmbh.de/en/pro-500-1100-coating-system.html`. Accessed: 24/05/2018.

[57] Elettrorava S.p.A. PECVD Deposition Systems, 2002. Retrieved from: `http://www.elettrorava.com/en/pecvd-deposition-systems.html`. Accessed: 24/05/2018.

[58] Brewer Science. Apogee Spin Coater With DataStream Technology, 2016. Retrieved from: `https://www.brewerscience.com/wp-content/uploads/2016/06/apogee_spin_coater.pdf`. Accessed: 24/05/2018.

[59] Shipley. Megaposit SPR3000 series photo resist, 2018. Retrieved from: `http://www.microchem.com/PDFs_Dow/SPR%203000%20Data%20Sheet.pdf`. Accessed: 24/05/2018.

[60] SÜSS Microtec SE. MA/BA6 Mask and Bond Aligner, 2016. Retrieved from: `https://www.suss.com/en/products-solutions/mask-aligner/ma-ba-6`. Accessed: 24/05/2018.

[61] C. Mack. *Fundamental principles of optical lithography: the science of microfabrication*. John Wiley & Sons, Chichester, U.K., 2008. ISBN 9780470018934.

[62] Shipley. Megaposit MF-300 series developers, 2005. Retrieved from: `http://web.nano.cnr.it/litho/wp-content/datasheets/MF300seriesdevelopers.pdf`. Accessed: 24/05/2018.

[63] M. Hrouzek. *Atomic Force Microscopy, modeling, estimation and control*. PhD thesis, Université Joseph Fourier, Grenoble & Brno University of Technology, 2007.

[64] NT-MDT Spectrum Instruments. NTEGRA - Modular SPM (AFM, STM) system, 2008. Retrieved from: `https://www.ntmdt-si.com/products/modular-afm/ntegra-ii`. Accessed: 24/05/2018.

[65] NT-MDT Spectrum Instruments. Specification of HA_NC probe series, 2012. Retrieved from: `http://www.ntmdt-tips.com/products/view/ha-nc`. Accessed: 11/05/2018.

[66] Gwyddion. Gwyddion - Free SPM data analysis software, 2018. Retrieved from: `http://www.gwyddion.net`. Accessed: 24/05/2018.

[67] PerkinElmer, Inc. *Lambda 650/850/950 Hardware Guide*, 2004.

[68] Perkin Elmer. LAMBDA 950 UV/Vis Spectrophotometer, 2004. Retrieved from: `http://www.perkinelmer.com/nl/product/lambda-950-uv-vis-nir-spectrophotometer-l950`. Accessed: 24/05/2018.

[69] OMT Solutions B.V. Absolute Reflectance/Transmittance Analyzer (ARTA), 2016. Retrieved from: `http://www.omtsolutions.com/products/absolute-reflectance-transmittance-analyzer-arta/`. Accessed: 24/05/2018.

[70] P. A. van Nijnatten, J. M. C. de Wolf, and I. J. E. Schoofs. *Spectrophotometer accessories for thin film characterisation*, 2008. 7th ICCG (International Conference on Coatings on Glass & Plastics), Breda, The Netherlands.

[71] Labsphere. Spectralon® Diffuse Reflectance Standards, 2006. Retrieved from: `https://www.labsphere.com/labsphere-products-solutions/materials-coatings-2/targets-standards/diffuse-reflectance-standards/diffuse-reflectance-standards/`. Accessed: 24/05/2018.

[72] H. Fujiwara. *Spectroscopic ellipsometry: principles and applications.* John Wiley & Sons, Chichester, U.K., 2007. ISBN 9780470016084.

[73] J.A. Woollam Co., Inc. M-20000 Specifications, 2015. Retrieved from: `https://www.moles.washington.edu//wordpress/wp-content/uploads/2015/03/Woollam_Ellipsometer_Specs.pdf`. Accessed: 24/05/2018.

[74] Wacom Electric Co., Ltd. Solar simulator (Continuous type), 2011. Retrieved from: `http://www.wacom-ele.co.jp/en/products/solar/normal/`. Accessed: 24/05/2018.

[75] Oriel Instruments - Newport Corporation. Cornerstone 130 1/8m Holographic Grating Monochromators, 2015. Retrieved from: `https://www.newport.com/f/cs130-holographic-grating-monochromators`. Accessed: 24/05/2018.

[76] Ametek Scientific Instruments. 7225 Dual Phase DSP Lock-in Amplifier, 2001. Retrieved from: `https://www.ameteksi.com/products/lock-in-amplifiers/7225-dual-phase-dsp-lock-in-amplifier`. Accessed: 24/05/2018.

[77] National Instruments. What is LabVIEW?, 2018. Retrieved from: `http://www.ni.com/nl-nl/shop/labview.html`. Accessed: 27/05/2018.

[78] Kepco Power Solutions. Series BOP: Linear Power Supplies, 2005. Retrieved from: `http://www.kepcopower.com/bop.htm`. Accessed: 24/05/2018.

[79] E. Psomadaki. *Micro-textured glass for thin film silicon solar cells.* Master's thesis, Delft University of Technology, 2013.

[80] O. Tuna, Y. Selamet, G. Aygun, and L. Ozyuzer. High quality ito thin films grown by dc and rf sputtering without oxygen. *Journal of Physics D: Applied Physics*, **43**(5):055402, 2010.

[81] G. Mie. Beiträge zur optik trüber medien, speziell kolloidaler metallösungen. *Annalen der physik*, **330**(3):377–445, 1908.

[82] Mentor - Siemens. Tanner L-Edit IC Layout, 2015. Retrieved from: `https://www.mentor.com/tannereda/l-edit`. Accessed: 25/05/2018.

[83] F.-J. Haug, T. Söderström, O. Cubero, V. Terrazzoni-Daudrix, and C. Ballif. Plasmonic absorption in textured silver back reflectors of thin film solar cells. *Journal of Applied Physics*, **104**(6): 064509, 2008.

[84] F.-J. Haug, T. Söderström, O. Cubero, V. Terrazzoni-Daudrix, and C. Ballif. Influence of the zno buffer on the guided mode structure in si/zno/ag multilayers. *Journal of Applied Physics*, **106** (4):044502, 2009.

[85] J. Meier, S. Dubail, R. Fluckiger, D. Fischer, H. Keppner, and A. Shah. Intrinsic microcrystalline silicon (µc-Si:H) - a promising new thin film solar cell material. In *Photovoltaic Energy Conversion, Conference Record of the Twenty Fourth IEEE Photovoltaic Specialists Conference*, volume 1, 409–412. IEEE, 1994.

[86] Thermo Fisher Scientific. Thermo Scientific Heratherm General Protocol Ovens - Operatin Instructions, 2010. Retrieved from: `https://assets.thermofisher.com/TFS-Assets/LED/manuals/D01712~.pdf`. Accessed: 07/06/2018.

[87] Lasergraaf.nl. MOPA fiberlaser 30 Watt kleur graveren “EMMA”, 2017. Retrieved from: `https://lasergraaf.nl/product/mopa-fiber-laser-30w-kleur-graveren/`. Accessed: 04/06/2018.

[88] G. Mei-Zhen, R. Job, X. De-Sheng, and W. R. Fahrner. Thickness dependence of resistivity and optical reflectance of ito films. *Chinese Physics Letters*, **25**(4):1380, 2008.

Glossary

List of Acronyms

AM	Air Mass
AC	Alternating Current
AZO	Aluminium-doped Zinc Oxide (ZnO:Al)
a-Si	Amorphous Silicon
AID	Angular Intensity Distribution
ARC	Anti-Reflective Coating
AR	Aspect Ratio
AFM	Atomic Force Microscopy
ACF	Autocorrelation Function
AGC	Asahi Glass Company
CdTe	Cadmium-Telluride
CI(G)S	Copper-Indium-(Gallium)-diSelenide
c-Si	Crystalline Silicon
DI	Deionised
DNQ	Diazonaphtoquinone
DC	Direct Current
E-beam	Electron Beam
EKL	Else Kooi Laboratory
EQE	External Quantum Efficiency
FF	Fill Factor
FTO	Fluorine-doped Tin Oxide (SnO_2:F)
FCA	Free-carrier Absorption
GaAs	Gallium Arsenide
HMDS	Hexamethyldisilazane
IOH	Hydrogen-doped Indium Oxide
ITO	Indium Tin Oxide (In_2O_3:Sn)
IPA	Isopropanol

LCOE	Levelised Cost of Electricity
LID	Light Induced Degradation
mpp	Maximum Power Point
μc-Si	Micro-crystalline Silicon (also known as nc-Si)
MST	Modulated Surface Texture
nc-Si	Nano-crystalline Silicon (also known as μc-Si)
NIR	Near Infrared
1D	One-dimensional
PAC	Photoactive Compound
PV	Photovoltaic
PZT	Piezoelectric
PECVD	Plasma Enhanced Chemical Vapour Deposition
QCM	Quartz Crystal Deposition Rate Monitor
QTH	Quartz-Tungsten-Halogen
RF	Radio-Frequency
SEM	Scanning Electron Microscope
SQ	Schockley-Queisser
SE	Spectroscopic Ellipsometry
SPPs	Surface Plasmon Polaritons
SET	Sustainable Energy Technology
TCM	Temporal Coupled Mode
SnO_2	Tin Oxide
TCO	Transparent Conductive Oxide
2D	Two-dimensional
UHV	Ultrahigh Vacuum
UV	Ultraviolet
UV-NIL	Ultraviolet Nanoimprint Lithography
VAS	Variable Angle Spectrometry
VHF	Very High Frequency
Vis	Visible Light
ZnO	Zinc Oxide

List of Symbols

A	Absorbance
$\alpha(\lambda)$	Absorption coefficient
δ_p	Penetration depth
$\delta\omega$	Frequency range
$\epsilon(\lambda)$	Complex electric permittivity
η	Conversion efficiency
γ_i	Intrinsic resonance loss rate
$\kappa(\lambda)$	Extinction coefficient
λ	Wavelength
ϕ	Angle of refraction, Azimuth angle
$\Psi_{ph,\lambda}$	Spectral photon flux
σ_{RMS}	Root Mean Square Roughness
θ_c	Critical angle
θ_i	Angle of incidence
$\tilde{n}(\lambda)$	Refractive index
c	Speed of light
E_{ph}	Photon energy
E_{ph}	Photon energy
E_C	Conduction band energy
E_G	Band gap energy
E_V	Valence band energy
F	Enhancement factor
H_R	Haze of reflected light
H_T	Haze of transmitted light
h	Planck's constant
I_{ph}	Photocurrent
$I(z,\lambda)$	Intensity of light
I	Irradiance
J_{mpp}	Maximum power point current density
J_{ph}	Photocurrent density
J_{SC}	Short circuit current density
k	Angular wave number

L_C	Autocorrelation length
L	Period of grating
m	Diffraction order
M	Number of resonances
$n(\lambda)$	Real part of the refractive index
N	Number of leakage channels
P_{max}	Peak power
q	Elemental charge
R_D	Diffuse reflectance
R_p	Shunt resistance
R_s	Series resistance
R_S	Specular reflectance
r_s, r_p	Amplitude ratio's reflected waves
R_T	Total reflectance
R	Reflectivity
T_D	Diffuse transmittance
T_S	Specular transmittance
T_T	Total transmittance
T	Transmittance
V_{mpp}	Maximum power point voltage
V_{OC}	Open circuit voltage
υ	Frequency of electromagnetic radiation

A

3D Angular Intensity Distribution Plots: 1D Grating and Modulated Surface Texture

This appendix presents the 3D projections that correspond to the angular intensity distribution (AID_T) plots that were presented in chapter 4. Figures A.1 to A.4 show the 3D graphs obtained by one-dimensional periodic gratings with periods of 1800, 2000, 2200 and 2400 nm. Figure A.5 presents the 3D projection of the AID_T graph corresponding to a modulated surface texture (MST) based on a randomly textured substrate and a one-dimensional (1D) periodic grating ($L = 2000$ nm).

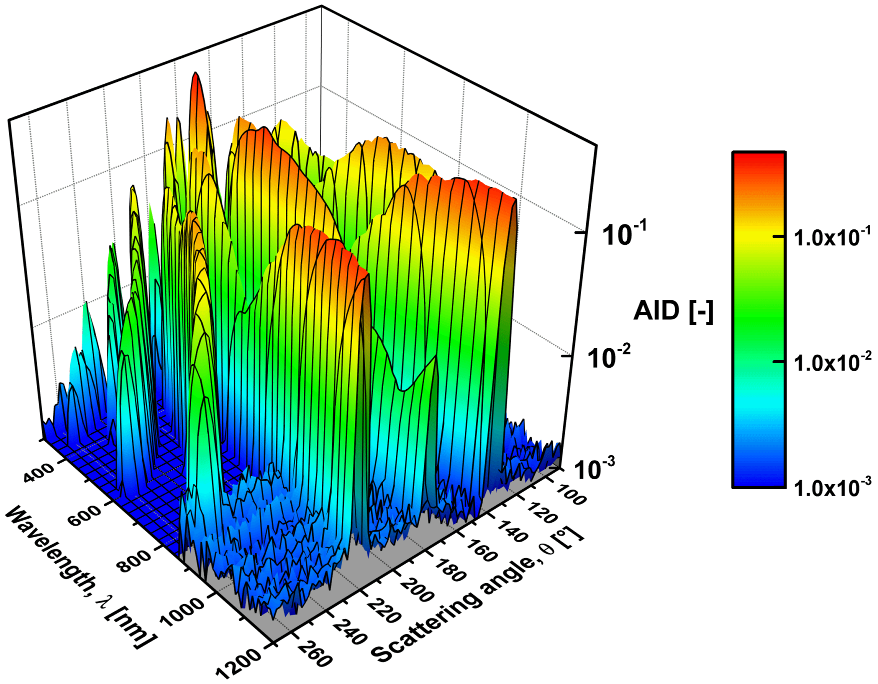

Figure A.1: AID_T of a 1D grating ($L = 1800$ nm).

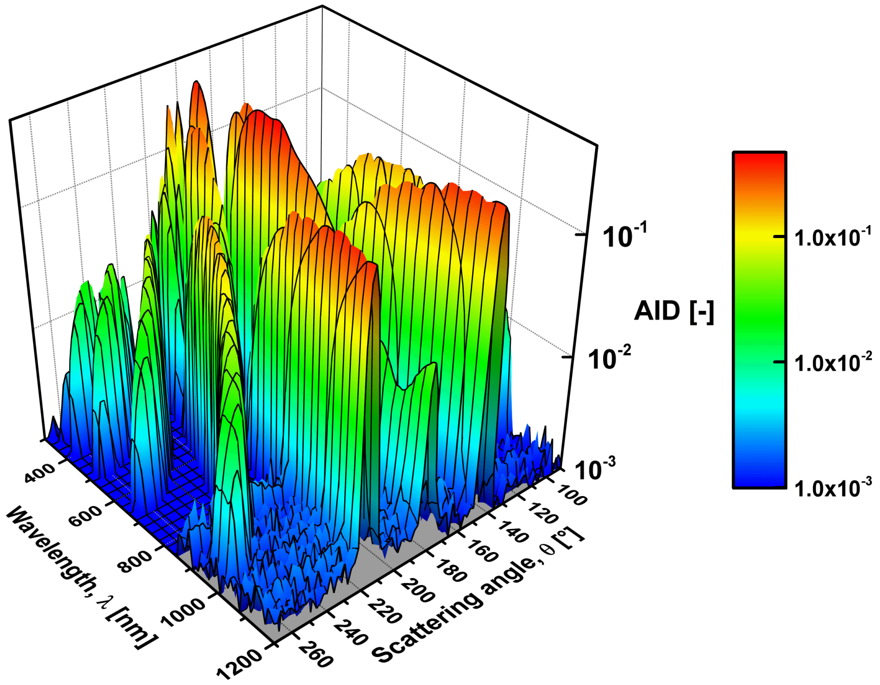

Figure A.2: $\mathrm{AID_T}$ of a 1D grating ($L = 2000$ nm).

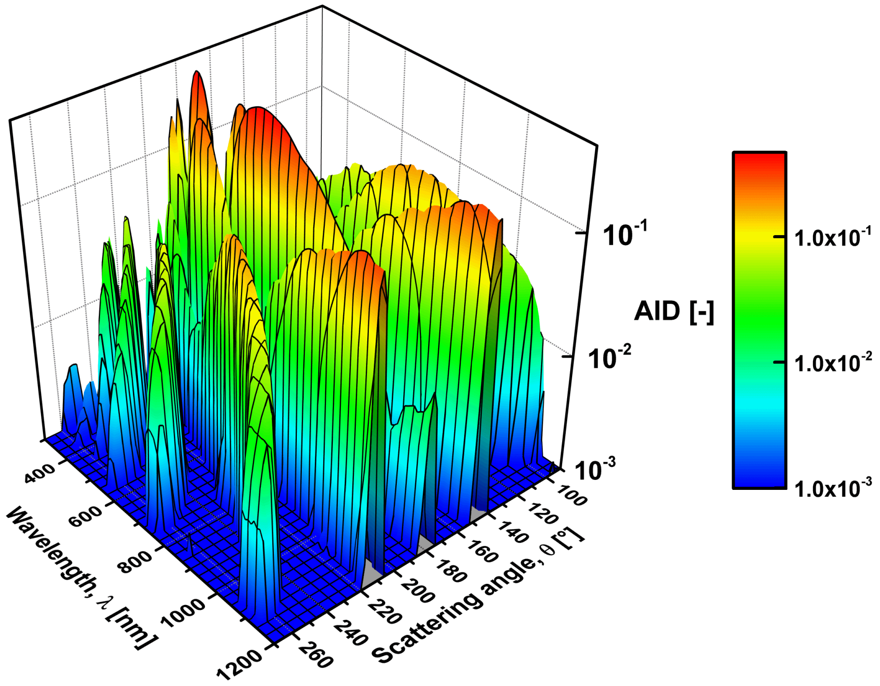

Figure A.3: $\mathrm{AID_T}$ of a 1D grating ($L = 2200$ nm).

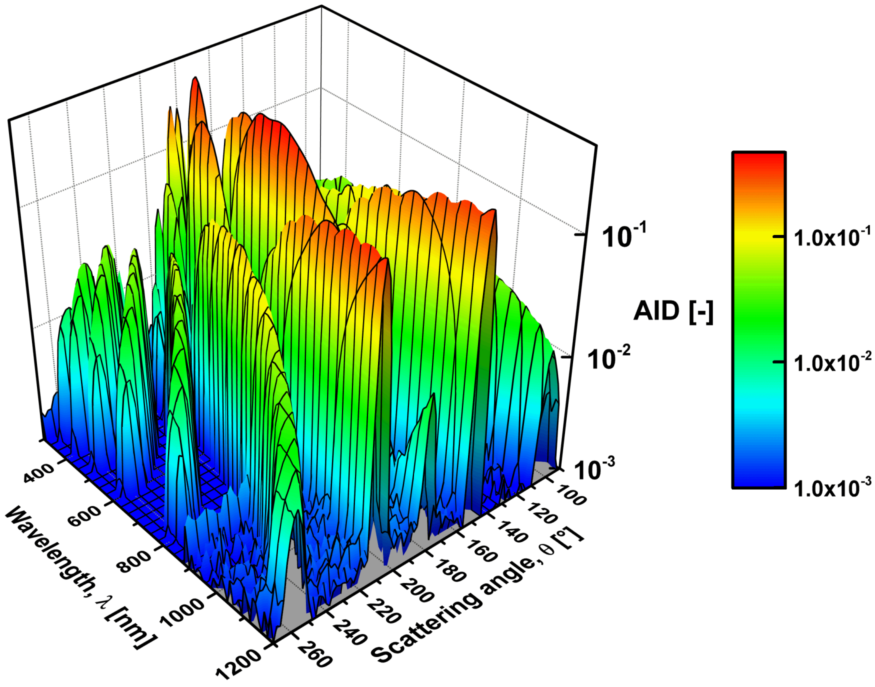

Figure A.4: $\mathrm{AID_T}$ of a 1D grating (L = 2400 nm).

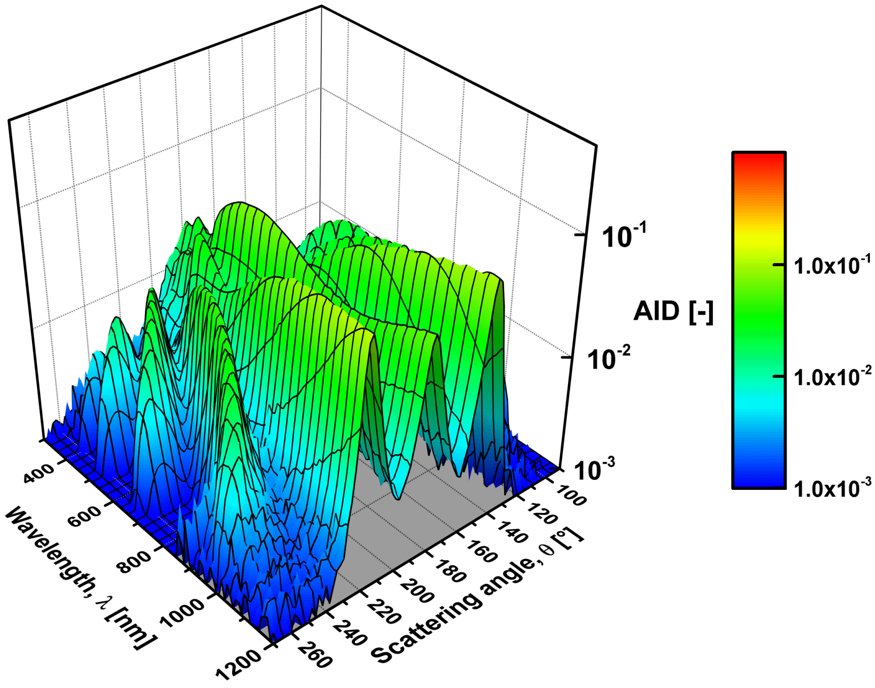

Figure A.5: $\mathrm{AID_T}$ of a MST based on a random texture and 1D grating (L = 2000 nm).

B

Absorption in Different Modulated Surface Texture Structures

Section 4.4 discussed the influence of the surface morphology of the back reflector on the light absorption in three different structures. Back reflectors based on flat glass, textured glass, and two-dimensional (2D) modulated surface textures (MST) were evaluated. A 2D MST structure, based on a square lattice structure with a period L = 3 μm, resulted in the highest absorption in the stack. Figure B.1 presents the results for all 2D MST structures, based on hexagonal and square lattice structures with periods of 3 and 4 μm.

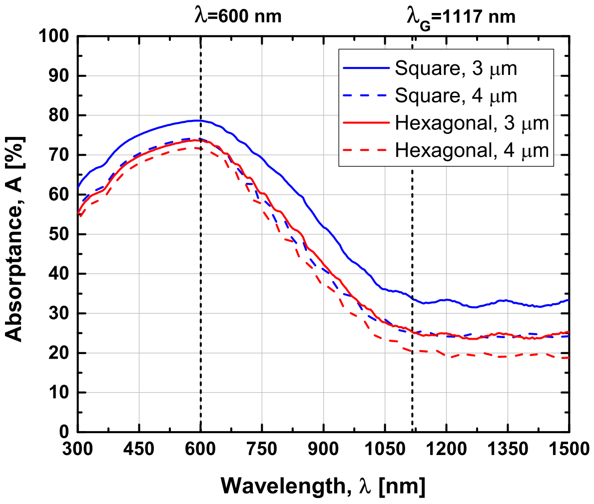

Figure B.1: Absorptance in a-SiO$_x$ / nc-Si:H structures, based on different two-dimensional modulated surface texture back reflectors.

These absorptance graphs all show a similar trend. As explained, the graph for a square lattice structure with a period L = 3 μm has a higher absorptance over the full spectrum. Lower front reflectance could be an explanation for this behaviour.

Another interesting observation it the difference between the periods that were evaluated. For both investigated lattice structures, a period of 3 μm seems to result in higher absorptance in the stack. Because the offset between the graphs corresponding to different periods seems approximately constant, a difference in front reflection is the most obvious explanation.

C

J-V characteristics of individual solar cells

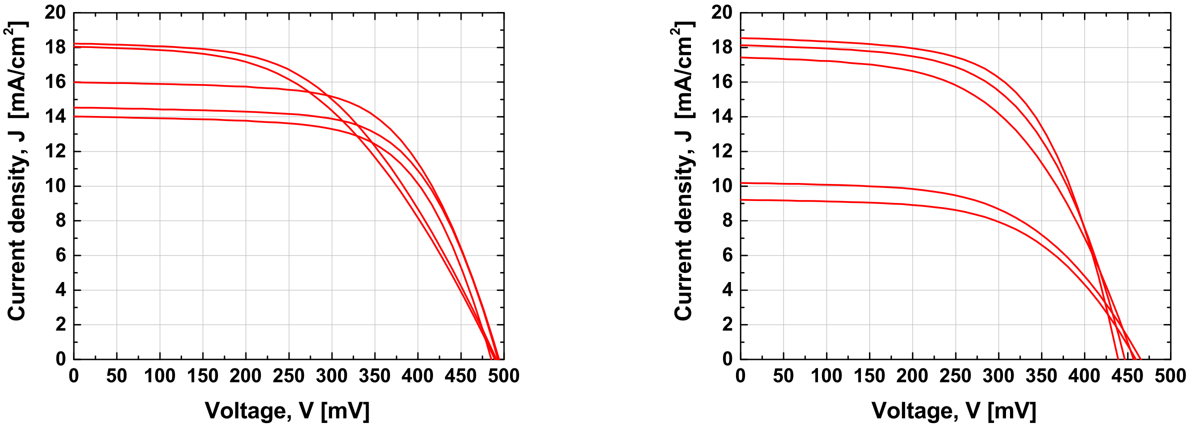

(a) **(b)**

Figure C.1: J-V curves of individual solar cells, used to average the external parameters in table 5.1. (a) Hexagonal and (b) Square lattice ($L = 3000$ nm).

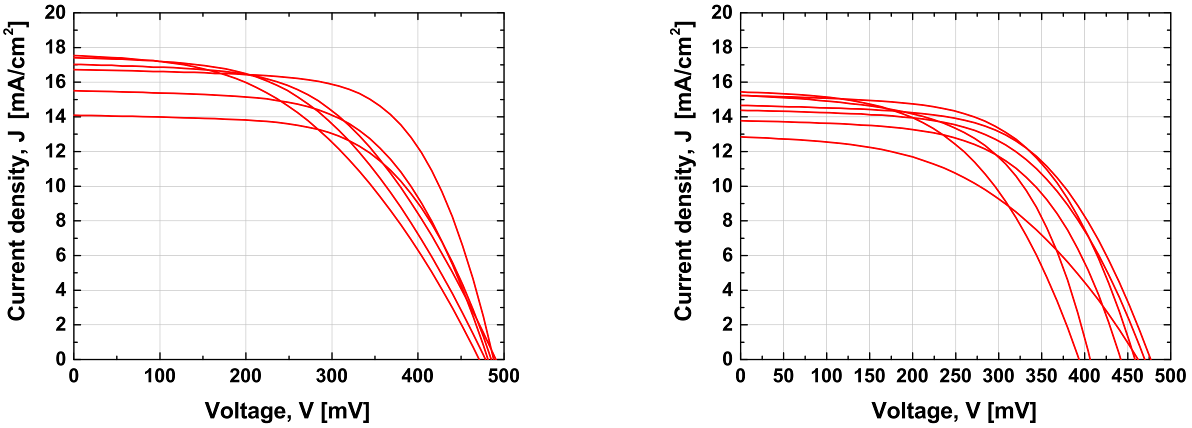

(a) **(b)**

Figure C.2: J-V curves of individual solar cells, used to average the external parameters in table 5.1. (a) Hexagonal and (b) Square lattice ($L = 4000$ nm).